Title
RESONANT RAMAN SCATTERING AS A PROBE OF INTRINSIC DEFECTS IN GaAs

Author
Berg, R.S.

Publication Date
1985-10-01

LBL-20328

RESONANT RAMAN SCATTERING AS A PROBE OF INTRINSIC DEFECTS IN GaAs

R.S. Berg
(Ph.D. Thesis)

October 1985

Lawrence Berkeley Laboratory
University of California
Berkeley, California 94720

Prepared for the U.S. Department of Energy
under Contract DE-AC03-76SF00098

Center for Advanced Materials

DISCLAIMER

LBL - 20328

RESONANT RAMAN SCATTERING

AS A PROBE OF INTRINSIC DEFECTS IN GaAs

Robert Scott Berg
(Ph.D. Thesis)

Department of Physics
University of California, Berkeley

and

Center for Advanced Materials
Lawrence Berkeley Laboratory
Berkeley, California 94720

October 1985

This work was supported by the Director, Office of Energy Research, Office of Basic Energy Sciences, Materials Sciences Division of the U.S. Department of Energy under contract number DE-AC03-76SF00098.

Resonant Raman Scattering as a Probe of Intrinsic Defects in GaAs

Abstract

This thesis presents a series of Raman scattering measurements performed on GaAs samples that have been irradiated with either high energy electrons or neutrons. The irradiation creates fairly high concentrations (10^{17} - 10^{18} cm^{-3}) of intrinsic defects. It is demonstrated that Raman scattering can give useful information about such defects.

One important result of this work is the observation of new and relatively sharp peaks in the Raman spectra of the irradiated samples. These are attributed to vibrational modes of a specific point defect created by the irradiation. On the basis of annealing experiments it is concluded that one of these modes is most likely associated with an As vacancy. The observed polarization dependence suggests that this can be a "breathing" vibration of the atoms surrounding the vacancy.

In addition, experiments were performed that measured the lineshape of the enhancement of the Raman cross section of both the intrinsic and extrinsic modes near the band gap of GaAs using a tunable near infra-red laser. It was observed that the enhancement of the defect induced modes was strong relative to the enhancement of the allowed TO phonon, which itself exhibits a strong enhancement. The observed enhancement lineshape can be explained by assuming that the scattering involving the defect induced modes occurs via a fourth order process. During this process quasi-momentum conservation is relaxed when electrons or holes scatter elastically from defects. On the basis of this model it is concluded that the strong resonant enhancement occurs when the vibrational modes involved have a component that is well localized around a defect. Thus resonant Raman

scattering has greater sensitivity to motion within the first few lattice constants surrounding a point defect and is well suited to provide microscopic information about such defects. Another important conclusion is that the strong enhancement of the Raman cross section of the defect induced modes should be present at critical points other than the fundamental gap.

Table of Contents

	Page
Chapter 1 - Introduction	
1.1 Overview and Motivation	1
1.2 Background Material	5
1.2a Macroscopic Theory of Raman Scattering	5
1.2b Properties of GaAs	9
i. Electronic Properties	9
ii. Vibrational Properties	10
1.2c Defects in GaAs	10
i. Defect Production by Irradiation	10
ii. Vibrational Defect Modes	12
References	15
Figure Captions	17
Figures	18
Chapter 2 - Raman Study of Neutron and Electron Irradiated GaAs	
2.1 Introduction	27
2.2 Microscopic Theory of Raman Scattering Involving Defects	29
2.2a Microscopic Description of Raman Scattering in a Perfect Crystal	29
2.2b Third Order Spatial Correlation Mechanism	31
2.2c Kawamura-Tsu-Esaki Model	35
2.2d Defect Mediated Higher Order Processes	37
2.3 Experimental Aspects	38
2.4 Results	40
2.5 Discussion	43

2.6 Conclusions 54

References 56

Figure Captions 59

Figures 62

Chapter 3 - Resonant Raman Study of Intrinsic Defect Related Modes in GaAs

3.1 Introduction 72

3.2 Theory of Resonant Raman Scattering in a Perfect Crystal 75

3.2a General Description 75

3.2b Allowed TO Phonon Scattering 78

3.2c Forbidden LO Phonon Scattering 82

3.3 Theory of Resonance Behavior of Defect Related Raman Scattering 87

3.3a Fourth Order Process Involving Plane Wave Phonons 87

3.3b Fourth Order Process Involving Non-Plane Wave Phonons 91

3.3c Third Order Process Involving Plane Wave Phonons 93

3.3d Third Order Process Involving Non-Plane Wave Phonons 94

3.4 Experimental Aspects 95

3.5 Results and Discussion 97

3.5a Resonance Behavior of the Allowed TO Phonon Scattering 97

3.5b Resonance Behavior of the Forbidden LO Phonon Scattering 100

3.5c Resonance Behavior of the Defect Related Raman Scattering 101

3.6 Conclusions 108

References 110

Figure Captions 112

Figures 116

Chapter 4 - Future Directions 137

Chapter 1

Introduction

1.1 Overview and Motivation

Defects in semiconductors play a pivotal role in the operation of devices made from these materials. This has spurred an intense effort to understand the underlying physics of these defects.

Due largely to inherently high carrier mobilities and efficient light emitting properties, the semiconductor GaAs is in the process of gaining widespread use in a variety of technological applications such as high speed computer circuits and optical communication systems. Thus the study of defects in GaAs is of especially great practical concern. In particular, there is currently much interest in the nature of intrinsic defects in GaAs such as vacancies and antisite defects due to their impact on device characteristics. Very small concentrations of such defects can exert a very large influence. For example the famous deep level EL2, which is thought to involve an intrinsic defect introduced during the crystal growth process, is responsible for the semi-insulating nature of high quality liquid encapsulated Czochralski (LEC) GaAs.[1] While techniques such as Deep Level Transient Spectroscopy (DLTS) have proved very useful in the study of many macroscopic aspects of these centers (e. g. position in the gap, concentration, whether the center traps electrons or holes),[2] very little is known about their microscopic identity. Electron Spin Resonance (EPR), which has provided a lot of information about

intrinsic defects in Si[3], has so far only been detected for the As_{Ga} antisite defect in GaAs.[4] Even in this case the EPR peaks are quite broad and tell little about the local environment of the defect. Thus it is important to develop additional techniques of high sensivity that can yield microscopic information concerning these defects.

In this thesis I will demonstrate the usefulness of another microscopic probe of intrinsic defects, namely Raman scattering. Raman scattering is an inelastic light scattering process which is depicted schematically in figure 1.1. The difference in energy between the incident and scattered photons is taken up by some elementary excitation of the scattering medium. Here I will consider Raman scattering involving phonons. Conservation of energy then implies

$$\hbar\omega_i = \hbar\omega_s \pm \hbar\omega_p \qquad (1.1.1)$$

where $\hbar\omega_i$, $\hbar\omega_s$ and $\hbar\omega_p$ are the energies of the incident photon, the scattered photon and the (emitted(+); absorbed(-)) phonon respectively.

If the scattering medium is crystalline then there also exists a quasi-momentum conservation law:

$$\hbar\vec{k}_i = \hbar\vec{k}_s \pm \hbar\vec{k}_p \qquad (1.1.2)$$

where $\vec{k}_i$, $\vec{k}_s$ and $\vec{k}_p$ are the wave vectors of the incident photon, the scattered photon and the (emitted(+); absorbed(-)) phonon respectively. Since $\vec{k}_i$ and $\vec{k}_s$ are typically $< 10^6$ cm^{-1} and so are very small in magnitude compared to the size of the Brillouin zone, (typically $\approx 10^8$ cm^{-1}), it follows that for a crystalline scattering

medium only near zone center phonons can participate in one phonon Raman scattering.

There are several aspects of Raman scattering that make it particularly well suited for studying intrinsic defects. For example, part of the difficulty in determining the electronic energy levels of intrinsic defects originates from the fact that intrinsic defects often form electronic states where the electron or hole is well localized in the vicinity of the defect. These are referred to as deep levels. Because of the localization of charge they will often couple strongly to the lattice. Thus the radiative efficiency of transitions involving such levels is often quite low and techniques such as photoluminescence lose some of their usefulness. Raman scattering on the other hand increases in strength as the electron lattice interaction increases.

Raman scattering is a higher order optical process. Therefore it provides symmetry information not available from commonly used optical probes such as absorption or luminescence, which involve first order processes. For example, in cubic materials such as GaAs, absorption and luminescence are not sensitive to the polarization of the light whereas the polarization dependence observed in Raman scattering provides information on the symmetry of the phonons. Furthermore, lattice vibrations are sensitive to local environments so it is possible to use Raman scattering to obtain structural information on the scale of a few lattice constants surrounding a defect. For these reasons Raman scattering has proved to be effective for the study of vibrational excitations in imperfect crystals, being complementary to infra-red techniques in many cases. Both of these methods are much more sensitive than neutron scattering for

investigating crystal defects present in small concentrations ($\leq$ 1 %).

So far, Raman scattering has been successfully used to study intrinsic defects in solids in a large number of investigations.[5-8] Indeed it is interesting to note that while one of the important conclusions of this thesis is the observation of Raman scattering due to vacancies in GaAs, it was twenty years ago that Worlock and Porto[9] reported Raman scattering induced by vacancies (F-centers) in alkali halides. Although many examples of defect related Raman scattering have been observed in alkali halide materials, relatively little work has been done in semiconductors. This is mainly due to the opacity of many semiconductors to visible light which, combined with the low concentration of defects, results in very weak defect related scattering signals.

I show in this thesis that by using incident photons with energy just below the band gap of neutron and electron irradiated GaAs I could take advantage of both the relative transparency of the material and the strong resonant enhancement to observe defect related scattering. The resonant enhancement occurs when the incident photon energy coincides with real electronic transitions in the medium. This phenomenon is known as resonant Raman scattering (RRS). These experiments were conducted using incident photons with energies that coincide with real electronic transitions of the medium (so called resonant conditions). This situation and its relation to non-resonant scattering is depicted in figure 1.2. In addition, by measuring how the Raman cross section changes as the incident photon energy is tuned through electronic resonances in the medium much valuable information

can be obtained about the electronic transition and the electron-phonon interactions of the medium. Chapter 3 presents a RRS study of defect related scattering in GaAs.

1.2 Background Material

1.2a. Macroscopic Theory of Raman scattering; The Raman Tensor and Selection Rules

The starting point in developing a macroscopic treatment of Raman scattering is with a general expression for the polarization $\vec{P}$ induced in a medium by an applied electric field $\vec{E}$. This is expressed in terms of a second rank susceptibility tensor $\overleftrightarrow{X}$:

$$\vec{P} = \overleftrightarrow{X} \cdot \vec{E} \; ; \; \vec{E} = \vec{E}_0 \exp(i\omega_i t) \qquad (1.2.1)$$

where ω_i is the frequency of the electric field. If $\overleftrightarrow{X}$ does not vary with time then it follows that P also oscillates at frequency ω_i. If the scattering medium consists of a single atom then the oscillating polarization will radiate at frequency ω_i in different directions to produce scattered light whose intensity I_s is given by

$$I_s \propto |\vec{E}_s|^2 \propto |\vec{P} \cdot \hat{e}_s|^2 \qquad (1.2.2)$$

where $\vec{E}_s$ is the scattered electric field and $\hat{e}_s$ is a unit vector in the direction of $\vec{E}_s$. If the scattering medium is macroscopic and perfectly homogeneous then there is a coherence between light scattered by different molecules within the medium. The result is that

light is only scattered in the forward direction. If, on the other hand, there are entropy fluctuations within the medium then the scattering again exhibits the $\cos^2$ directional dependence of equation 1.2.2. This is the familiar elastic scattering of light known as Rayleigh scattering.

In the macroscopic picture of Raman scattering the susceptibility $\overleftrightarrow{\chi}$ is assumed to be a function of some generalized parameter Q that describes the amplitude of a fluctuation. For example, in the case of phonons, Q would correspond to the amplitude of vibration. Then

$$\vec{P} = \overleftrightarrow{\chi}(Q)\cdot\vec{E} \tag{1.2.3}$$

By Taylor expanding $\overleftrightarrow{\chi}$ about the equilibrium coordinate Q_0 we have

$$\begin{aligned}\vec{P} &= \overleftrightarrow{\chi}(Q_0)\cdot\vec{E} + \left.\frac{d\overleftrightarrow{\chi}}{dQ}\right|_{Q_0}(\Delta Q)\cdot\vec{E} + \ldots \\ &= \vec{P}_0 + \vec{P}_1 + \ldots\end{aligned} \tag{1.2.4}$$

where

$$\Delta Q = Q - Q_0$$

If the phonon frequency is ω_p then

$$\Delta Q(t) \propto \exp(i\omega_p t) + \exp(-i\omega_p t) \tag{1.2.5}$$

so that $\overleftrightarrow{\chi}$ now is time dependent. It follows that $\vec{P}_1$ has frequency $\omega_i \pm \omega_p$. Thus the $\vec{P}_1$ component of the induced polarization will radiate at

these frequencies. The - (+) sign corresponds to Stokes (anti-Stokes) scattering in which the scattered radiation is down-shifted (up-shifted) in frequency from the incident radiation.

It is convenient to define a second rank tensor known as the Raman tensor $\overleftrightarrow{R}$ in the following manner:

$$\overleftrightarrow{R} = \left(\frac{d\overleftrightarrow{\chi}}{dQ}\right) \frac{\Delta Q}{|\Delta Q|} \tag{1.2.6}$$

so that the scattered intensity I_l can be expressed as

$$I_l \propto |\hat{e}_s \cdot \vec{P}_l|^2 \propto |\hat{e}_s \cdot \overleftrightarrow{R} \cdot \vec{E}|^2 \, |\Delta Q|^2 \propto I_i |\hat{e}_s \cdot \overleftrightarrow{R} \cdot \hat{e}_i|^2 \, |\Delta Q|^2 \tag{1.2.7}$$

where $\hat{e}_i$ and $\hat{e}_s$ are the polarizations of the incident and scattered radiations respectively.

A more complete treatment[10] shows that

$$I_l \propto V\omega_i{}^3\omega_s |\hat{e}_s \cdot \overleftrightarrow{R} \cdot \hat{e}_i|^2 \langle \Delta Q^2 \rangle \tag{1.2.8}$$

where V is the scattering volume and $\langle\ \rangle$ denotes a thermal average. (Taking a thermal average reflects the fact that the phonons responsible for Raman scattering are thermally generated.) It can be shown[10] from a quantum mechanical treatment of lattice vibrations that

$$\langle \Delta Q^2 \rangle = A(n + 1) + B(n) \tag{1.2.9}$$

where the first term describes Stokes scattering, the second term describes anti-Stokes scattering and n is the occupation number of the phonon.

The symmetry properties of the scattering medium impose restrictions on the polarizations and propagation directions of the scattered radiation. This is because the relation

$$\vec{P}_1 = \overleftrightarrow{\chi}_1 \cdot \vec{E} \qquad (1.2.10)$$

must be invariant under any operation that leaves the scattering medium unchanged (e. g. rotation about a symmetry axis, reflection about a symmetry plane, etc.) This requirement has two main consequences.

The first is the existence of selection rules that limit the symmetries of the excitations that can participate in the scattering. That is, the invariance condition mentioned above is satisfied only for excitations whose symmetries are such that both sides of eqn.(1.2.10) have the same transformation properties.[11] It is important to note that in the standard derivation of these selection rules for so-called allowed Raman scattering it is assumed that the phonons involved have $\vec{q}=0$. This greatly simplifies the analysis because a zone center phonon produces a lattice deformation that preserves the translational symmetry of the crystal. Thus it is valid to use a group theoretical treatment based on the point group of the crystal.

The second consequence is the imposition of restrictions on the components P_{ij} of the Raman tensor $\overleftrightarrow{R}$. These restrictions depend on both the point group symmetry of the scattering medium and on the symmetry of the excitation that participates in the Raman process. A complete calculation of these Raman tensors was performed by Nye

(1957)[12]. The result for materials of the zincblende structure like GaAs, which possess the so-called T_d point group symmetry, are shown in Table 1.1 for all of the allowed excitation symmetries. Once these tensors are known it is straightforward to calculate the dependence of the Raman scattering on the scattering geometry for various phonon symmetries. The results are shown in Table 1.2.

1.2b Properties of GaAs

In this section I summarize some of the electronic and vibrational properties of GaAs that are most relevant to this thesis. Table 1.3 lists many of the parameters that characterize GaAs. The recent review article by Blakemore[13] provides a fairly complete survey of the properties of GaAs.

i. Electronic Properties of GaAs

The theoretical band structure for GaAs is shown in figure 1.3[14]. The various critical points are labelled. Of particular note is the transition E_0, which has an energy of 1.52 eV at 4 K. This is the fundamental gap and the fact that it is direct is the main reason that GaAs is an efficient light emitter. The Raman measurements described in this thesis were carried out in the vicinity of E_0. As we shall see, the direct nature of the gap contributes to the large resonant enhancement that I observe. Also noteworthy are: 1) the large spin-orbit splitting in the valence band so that a two band model to be used later is a good approximation and 2) the warping of the valence band so that a spherical approximation to be used later is not that

good.

ii. Vibrational Properties of GaAs

The experimental and theoretical phonon dispersion relations along high symmetry directions in GaAs are shown in figure 1.4a[15,16]. Note that at the zone center, the longitudinal optical (LO) phonon lies higher in frequency than the transverse optical (TO) phonon. This splitting is a consequence of the macroscopic electric field associated with long wavelength LO phonons in a polar material, which provides an additional restoring force for these oscillations.

The phonon density of states for GaAs calculated from the theoretical dispersion curve is shown in figure 1.4b. One characteristic feature of many zincblende materials with two atoms/unit cell is a gap in the density of states between the acoustical and the optical phonons. However, due to the similar masses of Ga and As, the zone edge acoustical and optical phonons are nearly degenerate in GaAs. Thus in this case no prominent gap exists but there is a region of low density (a so-called "pseudo-gap") near 240 cm^{-1}. However, there is a fair amount of uncertainty in the exact density of states in this region.

1.2c Defects in GaAs

i. Defect production by irradiation.

Defects or impurities can be introduced into semiconductors intentionally or unintentionally during the growth process or during subsequent heat treatments such as diffusion or annealing. Quenching

from high temperatures, plastic deformation and irradiation with high energy particles such as ions, electrons, neutrons or gamma rays are other ways in which defects can be created. It is difficult to control the defect concentration and spatial profile by quenching or plastic deformation. Also these techniques often tend to produce defect complexes. These problems are less severe with irradiation. Understanding the effects of irradiation is also important because of interest in the performance of semiconductor devices that have been subjected to high energy irradiation in space, inside nuclear reactors or from nuclear explosions.

A simple picture of the interaction of radiation with solids starts with an atom in a solid that is fixed in position by an energy barrier. If sufficient energy to overcome this barrier is transferred to this atom during a collision with an energetic particle then the atom will be displaced and defects are created. The amount of energy transferred in a collision is calculated by assuming that energy and momentum are conserved in the scattering process. The kinetic energy transferred depends on the scattering angle and on the relative masses of the atom and the impinging particle. The amount of kinetic energy transferred to a silicon atom as a function of incident energy for various types of irradiating particles is shown in figure 1.5. The main conclusion to be drawn from these results is that the more massive the irradiating particle, the less kinetic energy it will require to create a defect.

For GaAs the atomic masses are roughly twice as great as the Si mass so that energy transferred is decreased by a factor of two. Experimentally it has been found that the threshold energy for displacement of Ga or As is found to be roughly 10 eV.[17] When the

energy transferred greatly exceeds the threshold energy then the ejected atoms will possess sufficient kinetic energy to produce secondary defects. Since the mean free path of an ejected atom is very small, the result is a cluster of defects. As an example that is relevant to the work to be discussed in this thesis, an electron with energies on the order of an MeV will typically produce one atomic displacement per collision in GaAs while a 50keV neutron will produce many tens of defects.

ii. Defect related vibrational modes.

The introduction of point defects can influence Raman scattering by creating new types of vibrational modes which may appear in the Raman spectrum.[6] These vibrations can be grouped into the following categories.

1) Localized modes. These types of vibrations occur when atoms in the vicinity of a defect vibrate at frequencies different from those of the phonons found in the perfect crystal. Thus the vibrational energy cannot propagate away from the defect and remains localized around the defect. The linewidth of these modes is quite narrow and therefore they give rise to sharp Raman lines. The amplitude of a localized mode is large near the defect and dies away rapidly with distance from the defect. (Figure 1.6a).

2) Resonance modes. These have frequencies which lie within the phonon bands of the perfect crystal. The amplitudes of the resonance modes are enhanced near the defect but these modes may propagate throughout the lattice and closely resemble the bulk phonon modes at

distances far away from the defect. Hence they are refered to as quasi-localized (figure 1.6b). The frequency spread of such modes is broader than that exhibited by local modes. For some crystals there is no sharp dividing line between what is considered a local mode and what is a resonant mode. In general, the higher the density of bulk phonons at a given energy, the less localized and broader in frequency are the defect vibrational modes.

3) Spatially confined phonons. The presence of defects can limit the spatial extent of a bulk phonon (figure 1.6c). In general, the dimensions of the volume in which the phonon is confined are determined by the separation between defects. Such a phonon no longer has a well defined wave vector. Thus in a Raman process involving such phonons the wave vector conservation law (1.1.2) may no longer hold and it becomes possible for spatially confined phonons from throughout the Brillouin zone to participate in one phonon Raman scattering (see section 2.2b).

Phonons that are localized around point defects are interesting because they have the potential to provide microscopic information concerning the defect. Therefore it is important to calculate the vibrational modes associated with defects. Such calculations are often not easy. One first needs an accurate knowledge of the bulk modes in a defect free crystal. This in turn requires that the effective spring constants connecting the various atoms be known. Then one must calculate the changes in these spring constants and in the local geometry (i. e. lattice relaxtion) introduced by the defect. This is particularly difficult when deep levels are involved. Recent examples of these types of calculations can be found in references 18.

One important benefit of using Raman scattering to study vibrational modes of defects is that the symmetry of the vibration can be deduced from the observed Raman selection rules. To give the reader a physical picture of what these symmetries mean I show in figure 1.7 an example of a Γ_1 and a Γ_{15} symmetry vibration of a point defect (vacancy) that has tetrahedral symmetry.

References

1- See for example: E. R. Weber in Proceedings of the XIII International Conference on Defects in Semiconductors, Coronado, ed. by J. M. Parsey (1984).

2- See for example, G. L. Miller, D. V. Lang and L. C. Kimmerling, Ann. Rev. Mat. Sci. 1977, 377.

3- See for example: J. W. Corbett, in Point Defects in Solids, edited by J. H. Crawford and L. M. Slifkin (Plenum, New York and London, 1975), Vol. 2, p. 1; G. D. Watkins, ibid. p. 333.

4- R. J. Wagner, J. J. Krebs, G. H. Strauss and A. M. White, Sol. St. Comm. 36, 15 (1980).

5- A. A. Maradudin, Sol. St. Phys. 18, 273 (1966), Sol. St. Phys. 19, 1 (1966).

6- A. S. Barker and A. J. Sievers, Rev. Mod. Phys. suppl. 2 (1975).

7- A. A. Maradudin et. al., Sol. St. Phys. suppl. 3 (1971).

8- R. J. Elliot in Phonons in Perfect Lattices and in Lattices with Point Imperfections, ed. by R. W. H. Stevenson, London: Oliver and Boyd, p.377 (1971).

9- J. Worlock and S. P. S. Porto, Phys. Rev. Lett. 15, 697 (1965).

10- W. Hayes and R. Loudon, Scattering of Light by Crystals, John Wiley, New York, (1978).

11- In the language of group theory, if an excitation transforms according the the irreducible representation Γ_x then this excitation can participate in first order Raman scattering only if the direct product $\Gamma_x \times \Gamma_{pv}$ contains the representation Γ_{pv}. Here Γ_{pv} is the irreducible representation that describes how a polar vector transforms under the symmetry operations of the group.

12- J. F. Nye, Physical Properties of Crystals, Clarendon Press,

Oxford (1957).

13- J. S. Blakemore, J. Appl. Phys. 53, R123 (1982).

14- J. R. Cheilkowsky and M. L. Cohen, Phys. Rev. Lett. 32, 674 (1974).

15- H. Bilz and W. Kress, Phonon Dispersion Relations in Insulators, Springer-Verlag, Berlin (1979).

16- G. Dolling and R. A. Crowley, Proc. Phys. Soc. (London) 88, 463 (1966).

17- D. Pons and J. C. Bourgoin, J. Appl. Phys. 51, 2038 (1980).

18- R. M. Feenstra, R. J. Hauenstein and T. C. McGill, Phys. Rev. B 28, 5793 (1983); R. J. Hauenstein, R. M. Feenstra and T. C. McGill, Phys. Rev. B 29, 1858 (1984); R. M. Feenstra, Proceedings of Defect Conference, Coronado, California (1984).

19- J. Bourgoin and M. Lannoo, Point Defects in Semiconductors II, Springer-Verlag, Berlin (1983).

Figure Captions

1.1- Schematic depiction of a Raman process involving phonons.

1.2- Schematic view of resonant Raman scattering.

1.3- Band Structure of GaAs as calculated by Cheilkowsky and Cohen in reference 14.

1.4- a) Phonon dispersion along high symmetry directions in GaAs. Symbols such as triangles, circles and squares are determined experimentally by neutron scattering[15]. Solid lines are the results of a calculation based on a shell model[16]. b) Phonon density of states derived from the shell model calculation.

1.5- Kinetic energy transferred by various irradiating particles to a silicon atom. From reference 19.

1.6- Various types of defect induced vibrational modes. a) Local mode. b) Resonance mode. c) Spatially confined mode.

1.7- Γ_1 and Γ_{15} vibrational modes of a tetrahedrally coordinated vacancy.

Table 1.1 Raman tensors for allowed excitation symmetries for crystals of T_d symmetry. If it is assumed that there is time-reversal invariance then the Raman tensor must be symmetric or c=0.

$$\begin{bmatrix} a & & \\ & a & \\ & & a \end{bmatrix} \quad \underbrace{\begin{bmatrix} b & & \\ & b & \\ & & -2b \end{bmatrix} \begin{bmatrix} & -3^{1/2}b & \\ -3^{1/2}b & & \\ & & \end{bmatrix}}_{E\ \Gamma_3\ \Gamma_{12}} \quad \underbrace{\begin{bmatrix} & & c \\ & & \\ -c & & \end{bmatrix} \begin{bmatrix} & & \\ & & c \\ -c & & \end{bmatrix} \begin{bmatrix} & c & \\ -c & & \\ & & \end{bmatrix}}_{T_1\ \Gamma_4\ \Gamma_{25}} \quad \underbrace{\begin{bmatrix} & & d \\ & & \\ d & & \end{bmatrix} \begin{bmatrix} & d & \\ d & & \\ & & \end{bmatrix} \begin{bmatrix} d & & \\ & d & \\ & & \end{bmatrix}}_{T_2\ \Gamma_4\ \Gamma_{15}}$$

$A_1\ \Gamma_1$

Table 1.2 Selection rules for Raman scattering by Γ_{25} (Γ_{15}) phonons in germanium and zinc-blende-type materials for the three principal surfaces [001], [111], and [110] in backscattering. The efficiencies are given in terms of the irreducible components a, b, c, d of Table 2.1

Surface	Incident polarization $\hat{e}_L$	Scattered polarization $\hat{e}_s$	Raman efficiency
$[1\bar{1}0]$	[110]	[110]	$a^2+b^2+d^2$ (TO)
$[1\bar{1}0]$	[001]	[001]	a^2+4b^2
$[1\bar{1}0]$	[001]	[110]	d^2 (TO)$+c^2$
$[1\bar{1}0]$	[111]	[111]	$a^2+\frac{4}{3}d^2$ (TO)
[100]	$[01\bar{1}]$	$[01\bar{1}]$	$a^2+b^2+d^2$ (LO)
[100]	[011]	$[01\bar{1}]$	$3b^2+c^2$
[100]	[010]	[001]	d^2 (LO)$+c^2$
[100]	[010]	[010]	a^2+4b^2
[111]	$[1\bar{1}0]$	$[1\bar{1}0]$	$a^2+\frac{1}{3}d^2$ (LO)$+\frac{2}{3}d^2$ (TO)
[111]	$[1\bar{1}0]$	$[11\bar{2}]$	$a^2+\frac{2}{3}d^2$ (TO)
[111]	$[11\bar{2}]$	$[11\bar{2}]$	$a^2+\frac{1}{3}d^2$ (LO)$+\frac{2}{3}d^2$ (TO)

Table 1.3-Some properties of GaAs. All values are for room temperature unless otherwise noted.

Crystal structure		zincblende
Space group		F43m
Lattice constant [nm]		0.5653
Linear thermal expansion coefficient [10^{-6}/K]		5.7
Atoms per primitive cell		1+1
Primitive cells per unit volume [10^{22}/cm^3]		2.21
Density [gm/cm^3]		5.31
Cleavage planes		{110}
Thermal conductivity [watt/cm K]	300 K	0.5
	77 K	3.
Melting temperature [°C]		1238
Debye temperature [K]	0 K	340
Bulk modulus [10^{10} Pa]		7.5
Elastic stiffness constants [10^{10} Pa]	c_{11}	11.8
	c_{12}	5.35
	c_{44}	5.94
	c_{13}	-
	c_{33}	-
Electron affinity [eV]		4.1
Dielectric constant	optical	11.0
	static	13.0
Optical phonon energy at q=0 [meV]	TO	33
	LO	36
Electron mobility [cm^2/V sec]	300 K	9000
	77 K	2×10^5
Hole mobility [cm^2/V sec]	300 K	400
	77 K	7000

Energy gap [eV]	300 K	1.424
	77 K	1.510
	0 K	1.519
$E_g(T)-E_g(0)=\alpha T^2/(T+\beta)$	α [10^{-4}eV/K]	-5.4
	β [K]	200
dE_g/dP [10^{-6}eV/bar]		12
Exciton binding energy [meV] at lowest energy gap		4.2
Shallow donors		Si_{Ga} Te_{As}
Binding energy [meV]		6 6
Shallow acceptors		Zn_{Ga} Si_{As}
Binding energy [meV]		31 35
Intrinsic carriers/cm^3		2×10^6
Conduction bands:		
Energy [eV], (symmetry)		1.71(L_6)
m_l/m, m_t/m		0.075, 1.9
Energy [eV], (symmetry)		1.43(Γ_6)
m_e/m, m_t/m		0.067
Valley degeneracy		1
Density of states mass [m]	per valley	0.07
	total	0.07
Valence bands:		
Density of states mass [m]		0.55
Energy [eV], (symmetry)		0(Γ_8)
Interband matrix element P^2 [eV]		29
A,B,C [$\hbar^2/2m$]		-6.8,-4.0,7.1
Energy [eV], (symmetry)		-0.34(Γ_7)
m^*/m		0.15

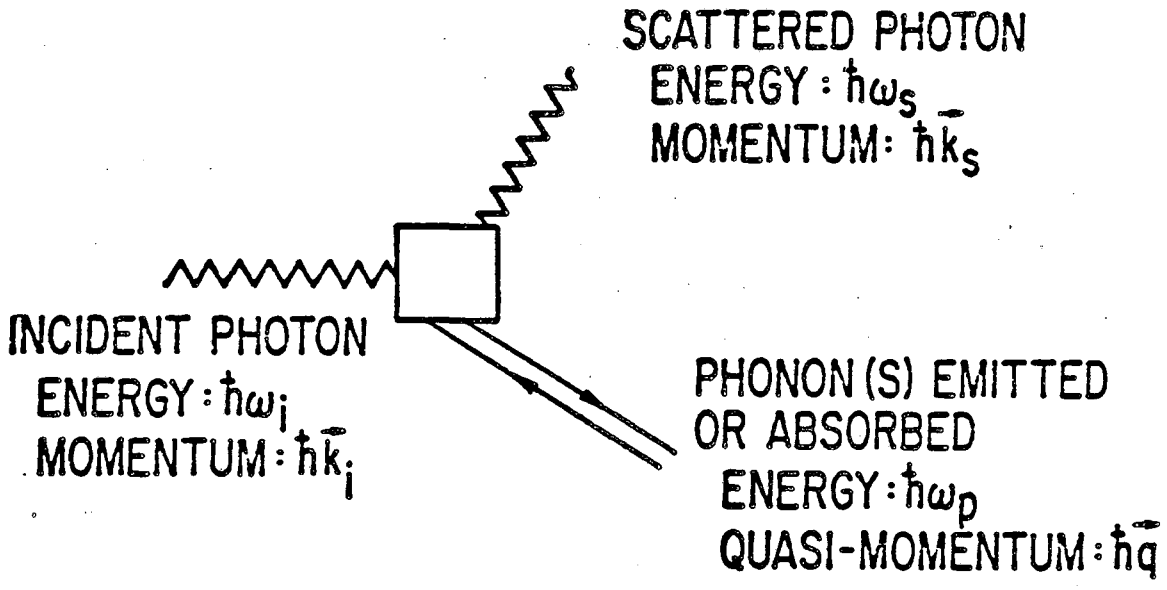

Figure 1.1 Diagrammatic representation of light scattering processes in a medium.

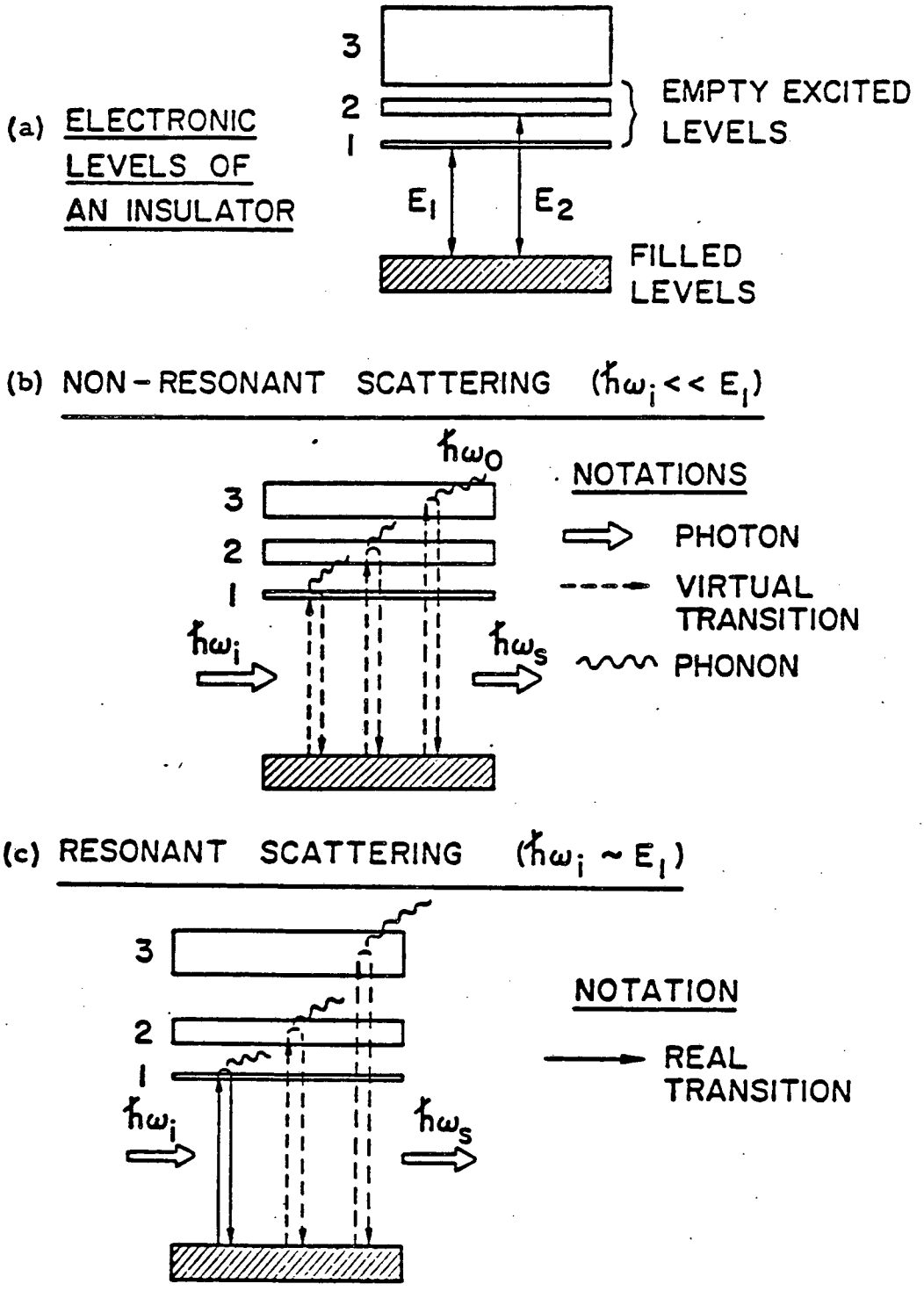

Figure 1.2 (a) Schematic electron energy bands in an insulator. Non-resonant (b) and resonant (c) light scattering processes in insulators.

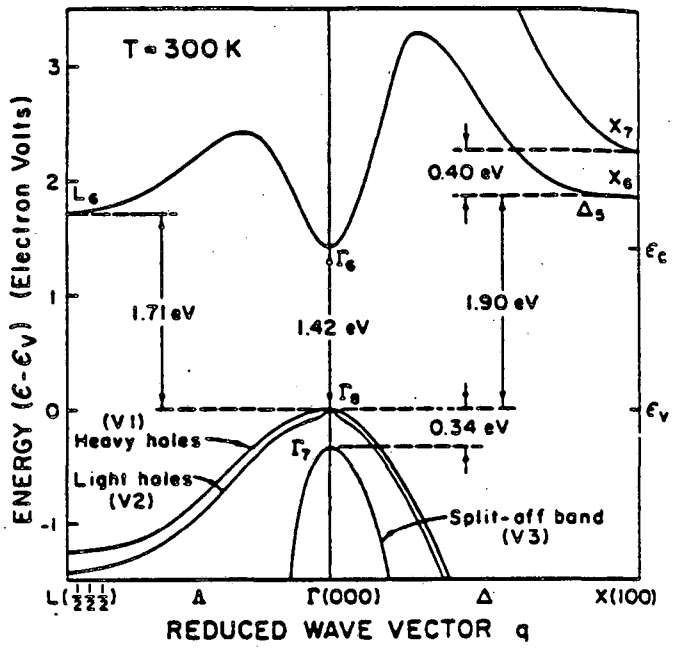

Variation of energy with wave vector for the uppermost part of the valence band system, and for the lowest sets of conduction band minima. Energy gaps are shown as appropriate for room temperature.

Figure 1.3

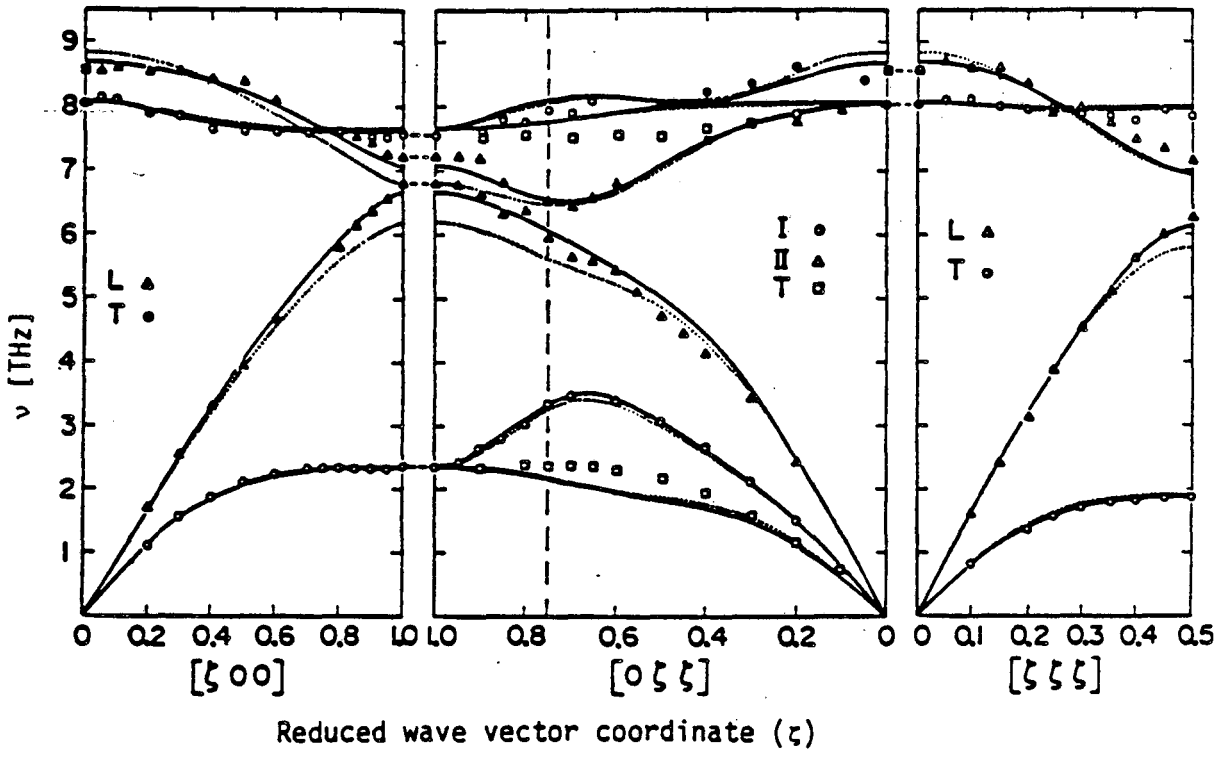

Figure 1.4a

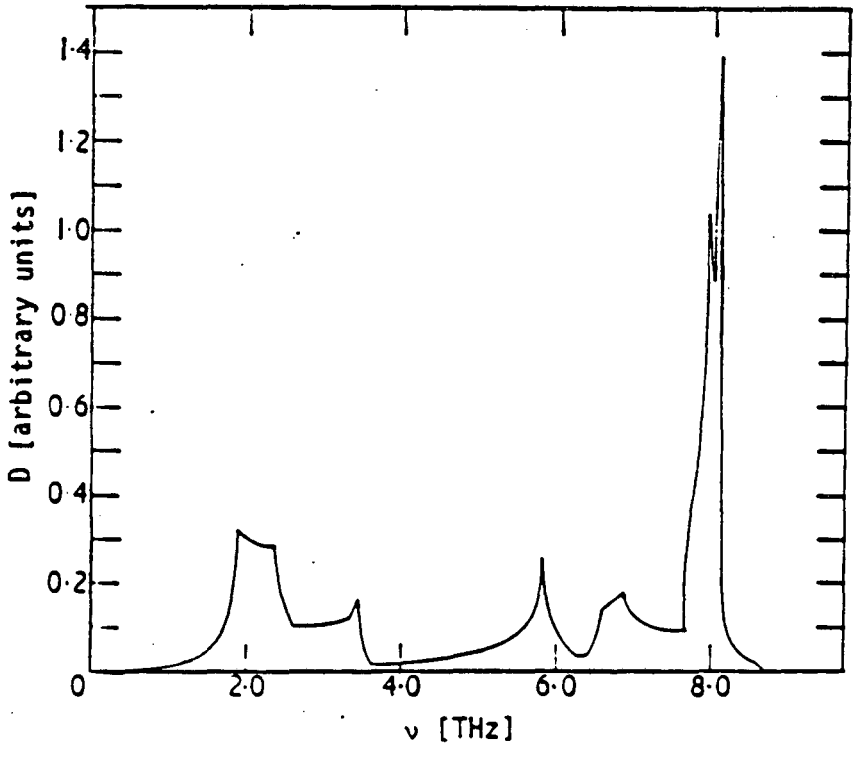

Figure 1.4b

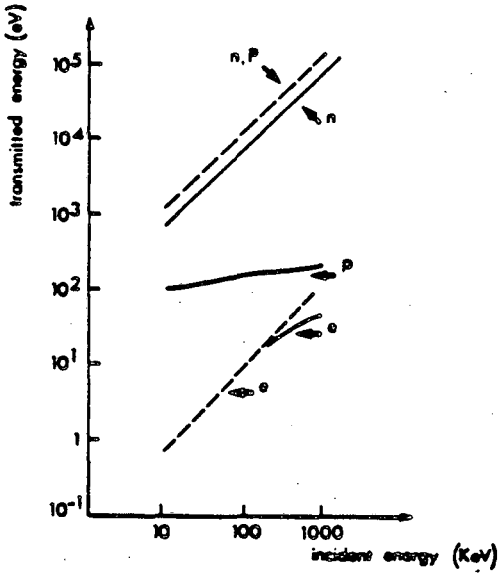

Maximum (dashed line) and average (full line) energy transmitted to a silicon atom as a function of the incident energy for electrons (e), protons (p), and neutrons (n)

Figure 1.5

a) LOCAL MODE

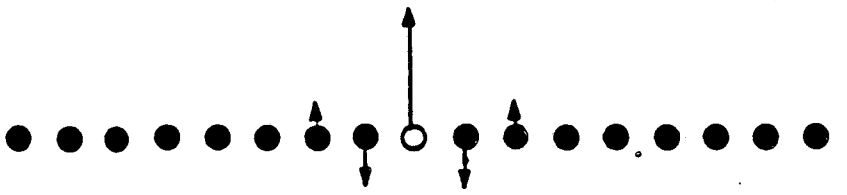

b) RESONANT MODE

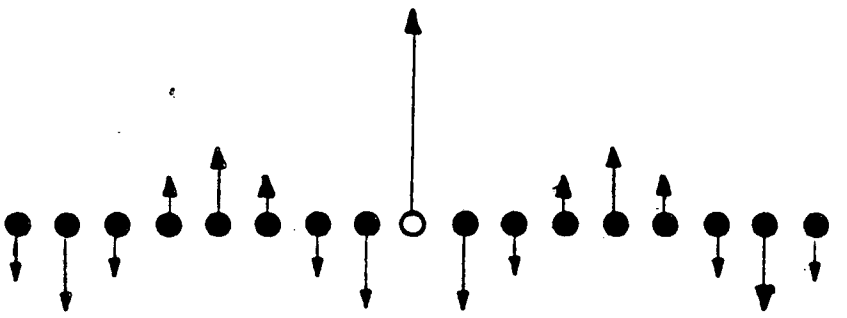

c) CONFINED MODE

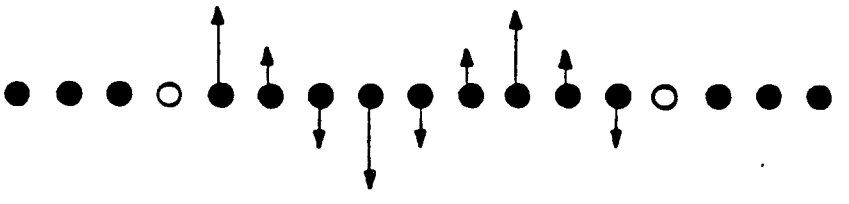

Figure 1.6

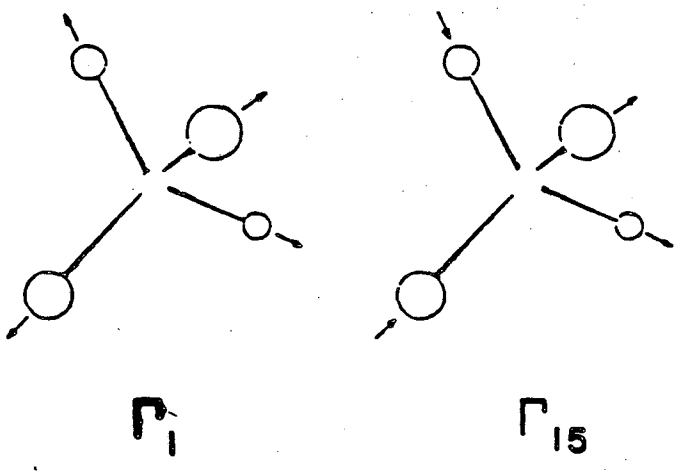

Figure 1.7

Chapter 2

Raman Study of Neutron and Electron Irradiated GaAs

2.1 Introduction

In this chapter I present results of Raman scattering measurements that have been performed on samples that have been damaged by irradiation with either high energy electrons or neutrons.[1]

As mentioned in chapter 1, there are basically two ways in which disorder affects Raman scattering:

1) Localized or resonant vibrational modes caused by the presence of defects appear as new structures in the Raman spectrum.

2) Defect induced Raman forbidden modes such as those which become observable because of a relaxation of the $\vec{k}$-conservation selection rule brought about by a disorder induced loss of translational invariance. There is a large body of previous work in which these two types of disorder related Raman scattering have been used to study defects in semiconductors.

A good example of the first class of defect related Raman scattering is the work of Cerdeira et. al.[2] in which the local modes of boron impurities in silicon were observed. Figure 2.1a shows a Raman spectrum of silicon that has been doped with 4×10^{20} cm^{-3} boron. As a result of the lighter atomic mass the boron vibrational modes occur at frequencies above the optical phonon frequencies of Si and hence they are local modes. There are two local mode peaks due to the two naturally occurring isotopes B^{10} and B^{11}. The positions of

these peaks are in good agreement with a simple model that assumes that only the mass of the defect changes while the spring constant remains unchanged. While such a model often gives accurate predictions when shallow impurities like boron in silicon are involved, it is often found to be inadequate in describing local modes associated with defects that produce deep electronic levels[3,4]. One should note the extremely high doping density required to observe the Raman scattering due to local modes. Many other examples of Raman studies of local modes have been reported in semiconductors.[5]

One example of the second type of disorder related Raman scattering that has been frequently studied is disorder activated first order Raman scattering (DAFORS). In this case a relaxation in $\vec{k}$-conservation allows zone edge phonons to participate in one phonon scattering. The types of disorder responsible for previous observations of DAFORS include effects due to the finite size of microcrystallites (in silicon[6]), ion implantation (in GaAs[7,8]) and disorder introduced by alloying[9-12]. In agreement with a simple theory to be described in section 2.2, the observed lineshape of the DAFORS was found to roughly reproduce the phonon density of states. As an example, figure 2.1b shows Ushioda's[7] results in ion implanted GaAs which can be compared to the calculated phonon density of states.

In this chapter I examine the effects of both neutron and electron irradiation on the Raman scattering observed in GaAs. In addition to scattering which I identify as DAFORS I observe new modes which are associated with intrinsic defects in GaAs. The narrow linewidth of these modes implies that they are due to quasi-localized (resonant) modes. The observed annealing behavior suggests that they

are due to the vibrational modes of an arsenic vacancy.

2.2 Microscopic Theory of Raman Scattering Involving Defects

2.2a) Microscopic Description of Raman Scattering in a Perfect Crystal

Before presenting the microscopic theories of defect induced scattering, it is first necessary to examine the microscopic theory of Raman scattering in a perfect crystal.

First order Raman scattering involves a third order perturbation process with two virtual intermediate states $|a\rangle$ and $|b\rangle$. For semiconductors and insulators, $|a\rangle$ is a state in which an electron is excited from the valence band to the conduction band via the absorption of a photon. $|b\rangle$ is a state in which an excited electron or hole is scattered into another state emitting (Stokes) or absorbing (anti-Stokes) a phonon. The electron and hole then recombine, emitting the scattered photon. Such a process can be represented by a Feynman diagram of the type shown in figure 2.2a. The transitions involved can occur in any time order, leading to six processes which give rise to six terms in the scattering cross section. The total probability for scattering a photon into a solid angle $d\Omega$ while emitting or absorbing a phonon of energy $\hbar\omega_p$ calculated for the diagram in figure 2.2a is:

$$\frac{1}{\tau} = \frac{2\pi}{\hbar^6} D(\omega_p) \sum_{\vec{k}_s} \left| \sum_{a,b} \frac{\langle f|H_{ER}|b\rangle\langle b|H_{EP}|a\rangle\langle a|H_{ER}|i\rangle}{(\hbar\omega_a - \hbar\omega_i)(\hbar\omega_b - \hbar\omega_s)} \right|^2 \quad (2.2.1)$$
$$\times \delta(\omega_i \mp \omega_p - \omega_s)$$

where H_{ER} and H_{EP} are the interaction Hamiltonians for the electron and photon and the electron and phonon respectively; ω_i, ω_s and ω_p are the frequencies of the initial photon, the scattered photon and the emitted (-) or absorbed (+) phonon respectively; $D(\omega_p)$ is the phonon density of states; and $\hbar\omega_a$ and $\hbar\omega_b$ are the energies of the intermediate states. For the diagram shown in figure 2.2a

$$\hbar\omega_a = \hbar\omega_0 + \hbar\omega_1 + \hbar\omega_3; \quad \hbar\omega_b = \hbar\omega_0 + \hbar\omega_2 + \hbar\omega_3;$$
$$\hbar\omega_0 \equiv \text{gap energy};$$

where $\hbar\omega_j$ (j = 1, 2 or 3) denotes the energy of the electron or hole relative to the band extrema. In a perfect crystal since quasi-momentum is conserved at each vertex of the diagram in figure 2.2a the overall quasi-momentum is conserved. Therefore $\vec{k}_i - \vec{k}_s = \vec{q}$ where $\vec{k}_i$, $\vec{k}_s$ and $\vec{q}$ are the wave vectors of the initial photon, the scattered photon and the emitted (+) or absorbed (-) phonon respectively. The summation over $\vec{k}_s$ in equation 2.2.1 includes only those photons scattered into the solid angle $d\Omega$.

Let us now consider how the presence of defects might modify the above description. In the remainder of this section I will examine three different microscopic mechanisms for Raman scattering involving defects.

2.2b) Third Order Spatial Correlation Model

This type of mechanism was first proposed by Shuker and Gammon[13] to explain the Raman lineshapes observed in amorphous silicon. They assumed that the electronic system is undisturbed by disorder; only the phonon system is affected. The relevant Feynman diagram for one phonon Raman scattering is shown in figure 2.2b. It is assumed that the only difference between the defect related Raman scattering shown there and the allowed Raman scattering of figure 2.2a is that the phonon in 2.2b is confined spatially so that it is no longer a plane wave of infinite extent and therefore does not have a well defined quasi-momentum. Note that even though momentum conservation is not required at the H_{EP} vertex the possible values of the intermediate electronic state momenta $\vec{k}_1$ and $\vec{k}_2$ are still subject to the constraint $\vec{k}_1 \simeq \vec{k}_2$. This is because of momentum conservation at the H_{ER} vertices, i.e.

$$\vec{k}_i = \vec{k}_1 - \vec{k}_3 \simeq 0$$

and

$$\vec{k}_s = \vec{k}_2 - \vec{k}_3 \simeq 0$$

implies that

$$\vec{k}_1 \simeq \vec{k}_2$$

In a perfect crystal the wave function for a phonon with wave vector $\vec{q}_o$ can be written

$$\phi(\vec{q}_o, \vec{r}) = u(\vec{q}_o) \exp(-i\vec{q}_o \cdot \vec{r}) \qquad (2.2.2)$$

where $u(\vec{q}_o)$ has the periodicity of the lattice and describes the atomic displacements within a unit cell for the phonon mode labelled by $\vec{q}_o$.

The present discussion is very general and our conclusions do not

depend on the precise manner in which the effect of disorder is added to the phonon wave function. Therefore I have arbitrarily localized the spatial extent of the phonon by multiplying it by a Gaussian envelope. (Such an envelope function has also been used by Richter et. al.[6], Tiong et. al[8] and Parayanthal et. al.[14] to explain the LO phonon lineshapes in various types of disordered semiconductors.) The localized phonon wave function is denoted by $\psi_L(q_o,r)$ with:

$$\psi_L(\vec{q}_o, \vec{r}) = \exp(-2r^2/L^2)\ \phi(\vec{q}_o, \vec{r}) \qquad (2.2.3)$$

With this definition L characterizes the spatial extent of the confined phonon. This type of model is often referred to as a spatial correlation (SC) model. Equation 2.2.3 can be rewritten as:

$$\psi_L(\vec{q}_o, \vec{r}) = \psi'_L(\vec{q}_o, \vec{r})u(\vec{q}_o)$$

with (2.2.4)

$$\psi'_L = \exp\left[\frac{-2r^2}{L^2} - i\vec{q}_o\cdot\vec{r}\right]$$

ψ'_L can be written in terms of its Fourier components:

$$\psi'_L(\vec{q}_o, \vec{r}) = \int d^3\vec{q}'\, C(\vec{q}_o, \vec{q}')\exp(i\vec{q}'\cdot\vec{r}) \qquad (2.2.5)$$

with

$$C(\vec{q}_o, \vec{q}') = (2\pi)^{-3} \int d^3r \psi_L'(\vec{q}_o, \vec{r}) \exp(-i\vec{q}' \cdot \vec{r}) \qquad (2.2.6)$$
$$= L(2\pi)^{-3/2} \exp\left[\frac{-L^2 |\vec{q}_o - \vec{q}'|^2}{4}\right]$$

If I assume that the total wave function of the system can be written as the product of an electron part and a phonon part

$$\Psi_{TOT} = \Phi_{\vec{k}}(\vec{R}) \psi_L(\vec{q}_o, \vec{r}) \qquad (2.2.7)$$

where $\vec{R}$ denotes the electron coordinates and $\vec{k}$ denotes the electron wave vector, then the electron-phonon matrix element in (2.2.1) can be written as:

$$\begin{aligned}
&\langle \Phi_{\vec{k}_2}, \psi_L(\vec{q}_o, \vec{r}) | H_{EP} | \Phi_{\vec{k}_1}, \Lambda \rangle \\
&= \iint d^3\vec{r} d^3\vec{R} \Phi^*_{\vec{k}_2}(\vec{R}) \psi^*_L(\vec{q}_o, \vec{r}) H_{EP} \Phi_{\vec{k}_1}(\vec{R}) \Lambda \\
&= \iint d^3\vec{r} d^3\vec{R} \Phi^*_{\vec{k}_2}(\vec{R}) \left[\int d^3\vec{q}' C(\vec{q}_o, \vec{q}') \exp(-i\vec{q}' \cdot \vec{r}) u^*(\vec{q}_o)\right] H_{EP} \Phi_{\vec{k}_1}(\vec{R}) \Lambda \qquad (2.2.8) \\
&= \int d^3\vec{q}' C(\vec{q}_o, \vec{q}') \left[\iint d^3\vec{r} d^3\vec{R} \Phi^*_{\vec{k}_2}(R) u^*(\vec{q}_o) \exp(-i\vec{q}' \cdot \vec{r}) H_{EP} \Phi_{\vec{k}_1}(\vec{R}) \Lambda\right]
\end{aligned}$$

where $|\psi_L(\vec{q}_o, \vec{r})\rangle$ represents the state with one spatially confined phonon present and $|\Lambda\rangle$ represents the phonon ground state in which no phonons are present.

The expression in square brackets in the last line of (2.2.8), which I shall call M, is the matrix element for an electron-phonon interaction involving plane wave phonons similar to those of (2.2.2). (The only difference is that for the phonons in (2.2.8) the argument of the function u is different from the phonon wavevector $\vec{q}'$.) For

Stokes scattering and the deformation potential type of electron-phonon interaction [15] one can show that:

$$M \propto \omega_p^{-\frac{1}{2}} \delta(\vec{k}_1 - \vec{k}_2 - \vec{q}') \tag{2.2.9}$$

Thus

$$\begin{aligned} &\langle \Phi_{\vec{k}_2} \psi_L(\vec{q}_o, \vec{r}) | H_{EP} | \Phi_{\vec{k}_1} \Lambda \rangle \\ &\propto \omega_p^{-\frac{1}{2}} \int d^3\vec{q}' C(\vec{q}_o, \vec{q}') \delta(\vec{k}_1 - \vec{k}_2 - \vec{q}') \\ &\propto C(\vec{q}_o, \vec{q}) \omega_p^{-\frac{1}{2}} \end{aligned} \tag{2.2.10}$$

where $\vec{q} = \vec{k}_1 - \vec{k}_2 \approx 0$ as in figure 2.2a.

Using (2.2.10) in (2.2.1) yields:

$$\begin{aligned} \tau^{-1}(\omega_p) &\propto D(\omega_p) \left| \omega_p^{-\frac{1}{2}} \int \frac{d^3\vec{k}_a \, C(\vec{q}_o, 0)}{(\hbar\omega_a - \hbar\omega_i)(\hbar\omega_b - \hbar\omega_s)} \right|^2 \\ &\propto \frac{D(\omega_p)}{\omega_p} \left| C(\vec{q}_o, 0) \right|^2 \end{aligned} \tag{2.2.11}$$

Equation (2.2.11) directly gives the lineshape for DAFORS that occurs via this SC mechanism. Note that if C^2 does not change greatly as $\vec{q}_o$ varies within the Brillouin zone, as would be the case if the phonon is well confined ($L \lesssim a_0$), then the lineshape approximately reproduces the phonon density of states $D(\omega_p)$.

The exact form of the factor $(C(\vec{q}_o,0))^2$ depends on the specific

manner in which disorder perturbs the phonons (equation 2.2.3). A more general form of (2.2.11) is

$$\tau^{-1}(\omega_p) \propto \frac{D(\omega_p)}{\omega_p} F(\vec{q}_o) \qquad (2.2.12)$$

where the function $F(\vec{q}_o)$ depends on the extent to which momentum conservation has been relaxed. Equation (2.2.12) is of the same form as the result obtained by Shuker and Gammon[13].

2.2c) Kawamura-Tsu-Esaki Model

The SC model assumed that the disorder which activates the normally forbidden Raman scattering crystal affects only the vibrational modes of the solid. It is also possible that disorder alters the electronic states of the scattering medium and hence causes new Raman processes to become allowed. A theory for DAFORS due to electronic disorder was proposed by Kawamura, Tsu and Esaki (KTE). KTE include the effect of disorder in the electronic system in a manner similar to that for the phonon system described in section 2.2b. The electronic wave functions are no longer described by plane waves characterized by a single wave vector but instead by a Fourier sum over a range of wave vectors.

$$\phi^L_{\vec{k}}(\vec{R}) = \int d^3\vec{k}' \; g_{\vec{k}}(\vec{k} - \vec{k}') \exp(i\vec{k}'\cdot\vec{R}) \qquad (2.2.13)$$

In equation 2.2.13 the subscript $\vec{k}$ denotes the wave vector of the unperturbed wave function. The function $g(\vec{k}')$ is the Fourier transform

of the perturbed electronic wave function $\phi^{L}_{\vec{k}}$ and thus is analogous to the function $C(\vec{q})$ that appears in the SC model of section 2.2b.

As a result of the assumption (2.2.13), all transitions involving electrons or holes do not necessarily have to conserve wave vector. This allows additional electronic states to participate in Raman scattering that would otherwise be forbidden by momentum conservation. An example of one scattering process involving such localized electronic states is shown by the Feynman diagram in figure 2.2c. (Since all three of the vertices in this diagram involve electronic transitions, disordered activated Raman scattering can involve either one, two or three momentum non-conserving steps. However, if the disorder is not too great then those processes with only one momentum non-conserving step will be most significant. In this case, as in the SC model, momentum conservation at the other two vertices constrains the electronic states to be the same as those that participate in allowed Raman scattering.)

KTE show that the rate for Raman scattering involving a phonon of wave vector $\vec{q}$ satisfies the proportionality

$$\tau^{-1} \propto \sum_{\vec{q}} \left| \omega_p^{-\frac{1}{2}} \int \frac{d^3\vec{k}_a \left[\int d^3\vec{k}' \; g^{\vec{q}}_{\vec{k}_a}(\vec{k}' + \vec{q}) \; g^{\vec{q}}_{\vec{k}_a}(\vec{k}') \right]}{(\hbar\omega_a - \hbar\omega_i)(\hbar\omega_b - \hbar\omega_s)} \right|^2 \qquad (2.2.14)$$

where $\vec{k}_a$ is the wave vector of the electron/hole in the first intermediate state $|a\rangle$. If the function $g^{\vec{q}}_{\vec{k}}$ does not depend on the subscript $\vec{k}$, (i.e. all of the electronic wave functions within the band are perturbed in the same way) then

$$\tau^{-1} \propto \frac{D(\omega_p)}{\omega_p} \left| C'(\vec{q}) \right|^2 \qquad (2.2.15)$$

where

$$C'(\vec{q}) \equiv \int d^3\vec{k}' \; g^*_{\vec{k}'}(\vec{k}' + \vec{q}) \; g_{\vec{k}'}(\vec{k}')$$

The result (2.2.15) is thus of the same form as the result obtained for the SC model (c.f. equation 2.2.11).

2.2d) Defect Mediated Higher Order Processes

A third possible mechanism for defect activated Raman scattering is represented by the Feynmann diagram in figure 2.2d. In these types of processes an electron or a hole undergoes elastic scatterings with a defect in addition to scattering with a phonon. Since momentum is transferred to the defect during the elastic scattering, phonons from throughout the Brillouin zone are allowed to participate in one phonon Raman scattering. Thus, like the SC and KTE mechanisms, this mechanism predicts Raman lineshapes that resemble the phonon density of states. However the resonance enhancement of the Raman intensity predicted by such a model can be quite different from that predicted by the SC and KTE mechanisms. This difference gives us an important means to distinguish this mechanism from the other two mechanisms. A detailed discussion of the resonance enhancement predicted by the above three mechanisms is deferred until chapter 3.

2.3 Experimental Aspects

The starting material for these experiments was semi-insulating LEC grown GaAs. One sample was uniformly irradiated with a flux of 3 x 10^{17} /cm^2 fast (50 keV) neutrons produced by the FRJ-1 reactor of the Kernforschungsanlage Juelich under conditions similar to those described by Worner et. al.[16]. The (110) surface of a second sample was irradiated with a flux of 1.0 x 10^{16} /cm^{-2} 1.6 Mev electrons produced by a Van De Graaf generator. The beam was focused to a diameter of approximately 3mm as estimated from viewing a piece of fluorescent material that was placed in the beam at the sample position. Thus I estimate that the peak intensity of the beam is approximately 1.1 x 10^{17} cm^{-2} . Since the beam size is smaller than the sample dimensions the sample is inhomogeneously damaged. The Raman spectra were recorded with the laser beam focused to a 75 micron spot on the sample where the damage is at a maximum. From the estimated electron flux at this point and the fact that the defect introduction rate within the first few millimeters of the sample for 1.6 MeV electron irradiation is[17]

$$1 \text{ incident electron } cm^{-2} \longleftrightarrow 5 \text{ total defects } cm^{-3}$$

I estimate that the <u>total</u> defect density in the region under investigation is approximately 5 x 10^{17} cm^{-3}. The procedure for locating this point is described below. Thus within the volume probed by the laser beam the damage is effectively homogeneous.

During both the electron and the neutron irradiations the sample temperature did not rise above 100 C. This implies that only defects with characteristic annealing temperatures > 100 C will be present in the samples after the irradiations.

For both the electron and the neutron irradiated samples the band edge luminescence is completely quenched, thus making it possible to observe weak Raman scattering near the E_0 gap. I note parenthetically that for a given concentration of defects, electron irradiation appears to be more effective in quenching the luminescence than neutron irradiation. This is presumably due to the fact that the defects produced by neutron irradiation occur in clusters. For comparison I have also studied GaAs grown by the horizontal Bridgeman technique and doped with $10^{17}cm^{-3}$ of Cr. In this case Cr is responsible for quenching the luminescence.

A standard experimental setup for recording Raman spectra was employed (figure 2.3). The sample was placed in an optical dewar and cooled to temperatures betwen 10 K and 100 K. The Raman spectra were recorded in a near-backscattering geometry from either (110) or (111) surfaces. Approximately 200 mW of excitation light was provided by a Styryl 9 dye laser pumped by an Ar^+ laser[18]. The dye laser was tuned to an energy of 1.47 eV, which is just below the fundamental band gap of GaAs. Thus I was able to take advantage of the relatively large scattering volume resulting from the large penetration depth of the light. In addition there was a very large resonant enhancement in the defect related scattering which greatly increased the strength of the scattered light. The scattered light was dispersed by a 3/4 m double spectrometer and detected as single photons by a cooled photomultiplier tube with a GaAs photocathode. Since the sensitivity of the tube falls off sharply below 11500 cm^{-1}, the spectra were corrected for the spectral response of the detection system which was determined by using a quartz halogen lamp as a light source. The Raman spectra were also corrected for the frequency dependence of the

absorption and relectivity of the samples measured in a separate experiment.

2.4 Results

In figure 2.4 I show the Stokes Raman spectra recorded from (110) surfaces for an unirradiated GaAs sample (a), a neutron irradiated sample (b) and an electron irradiated sample (c and d). In the frequency region below the transverse optical (TO) phonon the spectra of the irradiated samples are qualitatively similar to one another but differ significantly from that of the unirradiated sample. In this frequency region the Raman spectra of the irradiated samples show three additional peaks that I have labelled A, B and C.

As mentioned above, the electron irradiated sample was inhomogeneously damaged because the cross section of the electron beam was smaller than that of the sample. When the exciting laser beam is focused on an arbitrary point on the sample that has been electron irradiated, the resulting Raman spectra below the TO phonon frequency can typically be interpreted as a superposition of two types of scattering: 1) disorder related scattering similar to that shown in figure 2.1b and 2) allowed two-phonon overtone scattering similar to that shown in figure 2.4a. By monitoring the relative contribution of these two components as a function of the laser beam position on the sample it is possible to map out a "damage profile". The diameter of the damaged region determined in this manner is 3mm, in good agreement with the electron beam profile. This result confirms the supposition that what I have identified as defect related scattering is in fact

due to damage introduced by the electron irradiation. In the central 0.5 mm of the irradiated region the damage is large enough for the disorder induced scattering to overwhelm the two-phonon scattering so this region was chosen for more detailed studies.

The spectrum of the Cr-doped GaAs shown in figure 2.5b can also be described qualitatively as due to a superposition of the spectra of an unirradiated sample (figure 2.5a) and an irradiated sample (figure 2.5c), except for the fact that there is no clear evidence of the sharp peak A at 227 cm^{-1} found in the irradiated samples. This point is somewhat obscured by the presence of the broad shoulder around 227 cm^{-1} due to two-phonon overtone scattering. It would be interesting to look at GaAs with higher Cr concentrations, where the defect related scattering will overwhelm the two-phonon scattering. Unfortunately the 10^{17} cm^{-3} Cr concentration present in my sample is already close to the "solubility limit" of Cr in GaAs.

The spectra shown in figure 2.4a-c were recorded with the polarizations of both the incident and the scattered light parallel to the same (100) direction. According to the selection rules listed in table 1.2 phonon modes of Γ_1 and Γ_{12} symmetries are allowed in this scattering geometry. In figure 2.4d I show the Raman spectra recorded for the electron irradiated sample with the scattered light polarized perpendicular to the incident light. For a [110] surface only phonons with a Γ_{15} symmetry are allowed (see Tables 1.1,2). A new peak, labelled A' is apparent. The intensities of peaks A, B, C and the longitudinal optical (LO) phonon observed in this Γ_{15} geometry are all roughly 1/10 of the corresponding intensities in the Γ_1 and Γ_{12} configuration. Although the selection rules listed in Table 1.2 state that LO phonon scattering is forbidden from a [110] surface, it is

well known that forbidden LO phonon scattering can be observed under resonance conditions and exhibits predominantly Γ_1 symmetry. This will be discussed in more detail in chapter 3. On the other hand, the TO phonon is 60 times stronger in the allowed Γ_{15} configuration than in the forbidden geometries in accordance with the selection rules. I was unable to observe any defect induced scattering in the Γ_{15} symmetry configuration in the neutron irradiated sample.

To help identify the defects responsible for our observed spectra I subjected several pieces of the neutron irradiated sample to isochronal (one hour) annealing treatments at temperatures ranging from 220 C to 600 C. The results are shown in figure 2.6. The relative intensities of these spectra have been normalized by the TO phonon intensity. Peaks A, B and C remain unchanged in the sample annealed to 220 C but decrease sharply in the sample annealed to 320 C. By 440 C only a weak "density-of-states-like" structure is evident. The sharp peak A is no longer present. For the sample annealed to 600 C (not shown) a strong band edge luminescence was observed and it masked whatever Raman signal might be present.

In contrast with the acoustic phonon energy region which shows a great deal of disorder related scattering, the optical phonons appear relatively unchanged by the irradiation. No change at all is observable in the neutron irradiated sample even when examined with 1 cm^{-1} resolution at 10 K. In the electron irradiated samples only the LO phonon lineshape appears to be slightly asymmetrical, having a greater intensity in the low energy tail than in the high energy tail.

2.5 Discussion

As pointed out in section 1.2c, previous studies[19-21] on the nature of the damage produced by neutron and electron irradiation of GaAs have produced the following picture. In neutron irradiated samples, the materials surrounding a "primary knock on" contains clusters of defects but are otherwise basically crystalline (i.e. they are not amorphous). For samples irradiated with a flux of 3×10^{17} neutrons/cm^2 these damaged regions occupy roughly 5% of the total sample volume. It has been proposed that the primary defects in these damaged regions are interstitial-vacancy pairs that are accompanied by local strains. Larger defect complexes are not thought to be produced in large numbers. For the case of electron irradiated GaAs, the damage is thought to be more homogeneous, consisting of intrinsic point defects distributed uniformly throughout the irradiated region. This is because a collision of the lighter electron with an atom transfers only enough energy to eject a single atom. Thus the point defects that are created are spatially uncorrelated with one another.

As mentioned in section 2.2, the simple theories of DAFORS predict that the Raman lineshape should resemble the phonon density of states. This is in accordance with what has been observed experimentally by a number of workers[6-11] who examined either ion-implanted GaAs or various III-V alloys. Similarly, I have identified the peaks B and C in the irradiated samples as due to DAFORS. Comparison of the spectra in figure 2.4b,c with a calculation of the phonon density of states (figure 2.4e) shows that the lineshape of peak B is similar to the density of states of the longitudinal acoustic (LA) phonons while peak C reproduces the transverse acoustic

(TA) branches. While this correspondence suggests that peaks B and C are related to the bulk LA and TA phonons respectively, it does not unambiguously identify the exact nature of the phonons involved in the peaks B and C. For example, if the mechanism of KTE is responsible for the observed DAFORS then peaks B and C are due to processes involving plane wave phonons. On the other hand, if the SC mechanism is responsible for these peaks then the involved phonons are not plane waves. In this case the phonons might for example be spatially confined phonons or even resonant modes which happen to have a density of states that is quite similar to the bulk density of states.[3,4]

In contrast, peaks A and A' have not been observed in previous Raman studies of disordered GaAs. These peaks are much different from peaks B and C in that they are much narrower (full widths at half maximum of 7 cm^{-1}) and are not reproduced in the phonon density of states. One may argue that peak A can be explained by the broad structure near 227 cm^{-1} in the theoretical phonon density of states that arises from the LA(X) critical point. However, this explanation is not likely based on the following observations. Firstly, the structure at 227 cm^{-1} in the theoretical spectra is broader than peak A while all of the other peaks in the theoretical spectra are sharper than the corresponding peaks in the experimental spectra. Secondly, the structure near 227 cm^{-1} is weaker than the other structures in the phonon density of states while peak A is much stronger than the other DAFORS peaks. Of course one may question the accuracy of the calculated density of states. Fortunately there is experimental support for these results as can be seen by examining the Raman spectrum in figure 2.7, which was recorded with the laser beam

focussed at a point 1.5mm away from the point of maximum damage. In this figure both the disorder induced scattering and the two-phonon overtone scattering are visible. It is well known that the two phonon overtone spectrum roughly mirrors the phonon density of states scaled by a factor of 2[11]. Indeed, two phonon peaks corresponding to overtone scattering of peaks B and C are present (labelled 2B and 2C). However, the two-phonon overtone scattering observed in the range corresponding to twice the energy of peak A (455 cm^{-1})(labelled 2LA(X)) is too broad and weak to be identified as overtone scattering of peak A; instead it is more consistent with an overtone scattering associated with the critical point LA(X) in the phonon density of states.

I also rule out the possibility that peak A is due to a two phonon difference combination process involving emission of an optical phonon and absorption of an acoustical phonon because peak A is as strong at 10K as at 100K. For a difference combination process the Raman cross section should be proportional to

$$(n_{op} + 1)n_{ac}$$

where

$$n_{op} = (\exp(\hbar\omega_{op}/kT) - 1)^{-1} \; ; \; n_{ac} = (\exp(\hbar\omega_{ac}/kT) - 1)^{-1}$$

and $\hbar\omega_{op}$ ($\hbar\omega_{ac}$) is the optical (acoustical) phonon energy. For $\omega_{ac} \sim 50\text{-}80 cm^{-1}$ the factor n_{ac} would make this process much weaker at 10 K than at 100 K, contrary to what is observed experimentally. The difference combination process can also be ruled out because the corresponding two phonon sum combination peak is not observed. The absence of peak A in GaAs that has been disordered by a variety of other means such as ion implantation[7,8], alloying[9] or Cr doping (figure 2.5) implies that it is associated with the presence of a

specific defect introduced in relatively large concentrations by both neutron and electron irradiation.

I have therefore identified both peaks A and A' as due to either electronic or vibrational Raman scattering associated with some intrinsic defects induced by the irradiation. Electronic Raman scattering can be ruled out based on the dispersion of the Raman intensity as the laser frequency is tuned across the band gap. I found that the resonance enhancement of the Raman cross section of the A mode is quite similar in electron and neutron irradiated GaAs and is much too strong to be explained by electronic Raman scattering.[22] On the other hand this strong enhancement can be understood if peak A is a vibrational mode (local or resonant mode) of a defect. These results will be presented and discussed in detail in chapter 3.

The Raman spectrum observed in the sample that has been annealed to 440 C in Fig. 2.6 shows a weak DAFORS structure that is presumably caused by disorder that has not yet been annealed out. Noticeably absent from this spectrum is any evidence of the sharp peak A structure. This observation suggests that peak A is associated with a specific defect that has a characteristic annealing temperature in the range between 220 C and 320 C.

That peak A' was not observed in the neutron irradiated sample is most likely due to the fact that the absolute magnitude of the defect induced scattering is much weaker in this sample. If the ratio of the scattering intensities in the Γ_1 and Γ_{15} geometries were the same as for the electron irradiated samples the signal would be too weak to be detected in the neutron irradiated sample. In addition there is a relatively large featureless background in the spectra of the neutron

irradiated sample which makes it difficult to observe weak features.

The weakness of peak A' precludes any detailed measurement of its properties such as dependence on laser frequency. It should however be possible to examine its annealing characteristics which should shed light on whether peak A' is associated with the same defect as peak A. Its Γ_{15} symmetry suggests it should be infrared-active and thus may be more conveniently studied by far infrared absorption spectroscopy.

I contend that the sharpness of peaks A and A' suggests that they are associated with isolated point defects since Raman peaks associated with large defect clusters are more likely to have considerable inhomogeneous broadening. In principle ion implantation, like neutron and electron irradiation, will introduce large quantities of intrinsic defects, yet peak A has not been observed in ion implanted samples. However, as mentioned above, of the three kinds of high energy particles (ions, neutrons and electrons), ions and, to a lesser extent, neutrons tend to produce defect clusters while electrons produce isolated point defects. This is consistent with my observation that in the electron irradiated sample peak A is considerably stronger relative to the DAFORS and there is also less featureless background scattering than in the neutron irradiated sample.

The very narrow linewidths observed for peaks A and A' suggests that these peaks are due to vibrational modes that are well localized around a defect. One argument against such an identification might be that a localized mode cannot exist at an energy so close to the LA(X) critical point. The conventional wisdom has it that truly localized modes can only exist at energies where there are no bulk modes;

otherwise motion which is initially localized around the defect can very effectively propagate away into the bulk, resulting in a non-localized mode. Firstly, it should be noted that while the exact value of the phonon density of states is not precisely known in the energy range where peak A is located, by all accounts this density is not very high. Secondly a recent calculation of the vibrational modes of the deep level oxygen in GaP[3,4] shows that it is possible to get fairly well localized modes even when the energies of these modes are coincident with a relatively high density of bulk modes provided the localized modes do not couple to bulk modes.

Another point that can be made concerns the rather special nature of the atomic displacements associated with the LA(X) critical point. For this mode in GaAs all of the motion is taken up by the As atoms; the Ga atoms remain stationary.[23] On the other hand let us consider for example a localized breathing mode associated with an As vacancy. Presumably this mode consists largely of motion of the Ga atoms surrounding the vacancy. Thus it is not implausible that such a local mode will not couple to the LA(X) bulk mode.

I have argued that peak A is associated with a vibrational mode of a point defect. The list of candidates for this point defect is then I_{Ga}, I_{As}, V_{Ga}, V_{As}, As_{Ga} and Ga_{As}. The annealing behavior allows some of these to be ruled out. For example, ESR measurements in the neutron irradiated sample show that it contains $7\times10^{17}/cm^3$ As_{Ga} antisite defects.[24] Measurements by Worner et. al.[16] have shown that after one hour isochronal annealing the concentration of As_{Ga} as determined by ESR remains constant to 400 C above which the concentration drops sharply by a factor of 100. From my annealing results I conclude that the As_{Ga} defects are not responsible either

for peak A or for the bulk of the DAFORS that I observe. However it is possible that the weak structure appearing in the sample which has been annealed at 440 C is due to As_{Ga}.

An annealing stage in the vicinity of 225 C has been observed by nearly everyone who has performed an annealing experiment on either electron or neutron irradiated GaAs. A wide variety of experimental techniques, ranging from infra-red absorption to electrical resistivity, has been utilized to monitor the annealing. A summary of much of this work is given by Lang[25]. In particular, Pons and Bourgoin[26] used DLTS to observe this stage in electron irradiated GaAs. They demonstrate that the stage is due to the annealing of the so-called E2 electron trap. The microscopic identity of this level is not definitely known, but they present strong evidence that it is a simple defect formed by displacement of the As sublattice (i.e. V_{As}, As_{Ga} or I_{As}). Their argument is based on an anisotropy in the defect introduction rate when the electron beam is incident in the (111) or (-1 -1 -1) directions. Based on positron lifetime measurements, Cheng et. al.[27] argue that the arsenic vacancy is the more likely possibility. Pons et al.[28] also conclude that the vacancy is the more likely possibility. Recently Loualiche et al.[29] have shown additional evidence that this annealing stage is associated with As vacancies. On this basis I tentatively conclude that peak A is most likely associated with V_{As}.

The observed Γ_1 symmetry suggests a breathing mode (figure 1.7a), but care should be exercised in making such an identification as it is well known that Raman selection rules often breakdown near resonance. (For example, near resonance the forbidden LO phonon scattering is

observed to be primarily of Γ_1 symmetry even though the LO phonon has Γ_{15} symmetry.[30])

This proposed identification should be checked by a theoretical calculation of the vibrational properties of vacancies and interstitials in GaAs. (See section 1.2c.) If this identification of the 227 cm^{-1} Raman mode is confirmed by theoretical calculation, it will be a powerful means to study the properties of As vacancies in GaAs. In fact, recent theoretical calculations by Leite[31] predict that the arsenic vacancy should have two local modes, one of Γ_1 symmetry and the other of Γ_{15} symmetry, whose energy lies in the gap in the phonon density of states between the acoustical and optical branches. It should be noted that Leite's calculation assumes that there is a gap in the phonon density of states between the acoustical and optical branches and that these local modes lie within this gap. However, theoretical calculations of the phonon density of states (figure 2.4e), experimental determination of the phonon density of states based on DAFORS (figures 2.1b and 2.5b) and two-phonon overtone scattering (figure 2.7) all indicate that the phonon density of states is low near 230 cm^{-1}, but not zero.

Evidence that the defects involved in the 225 C annealing stage involve displacement of the As sublattice comes largely from studies in which differences in defect introduction rate as a function of whether the crystal is irradiated in the (111) or (-1 -1 -1) directions are monitored. This suggests that a useful experiment would be to measure the differences in the strength of the defect induced Raman signals as a function of irradiation direction as a means of confirming the identification of peak A as due to V_{As}.

Further examination of the annealing results yields some valuable

clues concerning the nature of the DAFORS involving peaks B and C. Comparison of the lineshapes of the sample annealed to 320 C with the unannealed sample reveals that not only has the intensity of the scattering diminished in the annealed sample but the lineshape now has lost its sharp structures that resemble the phonon density of states and taken on a more "washed out" appearance. This can be qualitatively understood within the framework of the models for DAFORS that were described in sections 2.2b (SC) and 2.2c (KTE). Both these models predicted DAFORS scattering rates that satisfy the proportionality given in (2.2.12).

Let us see what the consequences of these types of models are by investigating a particular idealized case of the SC model (figure 2.8). For the purposes of demonstration I assume a simple idealized one-dimensional dispersion relationship that may be appropriate for an acoustical branch (shown in figure 2.8a). The corresponding phonon density of states is shown in figure 2.8b. As in section 2.2b, the perturbed phonon is assumed to be described by a wave function that has a Gaussian envelope of the form

$$\psi_L(\vec{q}_o, \vec{r}) = \exp\left[\frac{-2r^2}{L^2}\right]\phi(\vec{q}_o, \vec{r}) \qquad (2.2.3)$$

where $\phi(\vec{q}_o,\vec{r})$ is the wave function of a bulk phonon.

The corresponding function $F(\vec{q}_o)$, which describes the extent to which momentum conservation has been relaxed is given by

$$F(\vec{q}_o) = \exp\left[\frac{-q_o{}^2 L^2}{2}\right] \qquad (2.5.1)$$

Plots of $F(\vec{q}_o)$ as a function of phonon frequency for several different values of the parameter L are shown in figure 2.8c. As expected, the more spatially confined the phonon, the greater the relaxation of momentum conservation. For spatially confined phonon modes (fig 1.6c) it is expected that L should increase as the defect concentration decreases. The effect of such an increase in L on the observed Raman lineshape, as predicted by (2.2.12), is shown in fig 2.8d. It can be seen that as L increases the Raman spectra becomes more "washed out", and no longer resembles the density of states. Since in the annealing experiment the defect concentration should decrease as the sample is heated, the disappearance of the phonon density of states structure in the Raman spectrum can be understood.

On the other hand the above explanation cannot account for the reemergence of the sharp density-of-states-like Raman structure in the sample annealed to 440 C. Similarly it cannot explain the Raman spectra of the samples that have been irradiated with lower electron dosages (figure 2.9). I will concentrate on the DAFORS peak C measured at two different locations within the electron irradiated region of the sample. One measurement takes place at the center of the damaged region while the other was recorded at a point 1.5 mm from the center. From the measured intensities of peak C relative to the TO phonon intensity (figure 2.9a) I estimate that the defect concentration differs by about a factor of 6 between these two points. (This estimate is roughly consistent with the measured Gaussian beam size of

3mm). In spite of the significant difference in defect concentration the shape of the DAFORS peaks observed at these two locations is identical (figure 2.9b).

As mentioned above, the phonons involved in the DAFORS peak C may be either spatially confined phonons, resonant phonons or plane wave phonons. Spatially confined phonons have localization lengths that depend on the separation between defects (figure 1.6c). Resonant modes on the other hand are associated with isolated point defects (figure 1.6b) and their spatial extent should be independent of the defect concentration. Obviously, the spatial extent of a plane wave phonon also does not depend on the defect concentration. Thus the insensitivity of the peak C to electron dosage in the electron irradiated samples suggests that peak C is due mostly to scattering involving either resonant phonons or plane wave phonons. On the other hand the same peak C is due to confined phonon modes in the neutron irradiated sample which has been annealed to less than 320C. I will present additional evidence to support this proposition in chapter 3.

A number of previous studies have focused on the observed asymmetry and red-shifting of the LO phonon line[6,8,14]. This effect has been successfully interpreted within the framework of the SC model. In order to make contact with this work, a few words concerning the LO phonon lineshapes in my GaAs sample are in order. I have been unable to detect any distortion in the LO phonon lineshape in the neutron irradiated sample and only a small asymmetry and broadening in the electron irradiated sample. One explanation for this observation is that the "damage threshold" for observing disorder related scattering is much lower in the acoustic phonon energy range, simply because the disorder related scattering is not competing with a

strong allowed first order scattering. This is especially true for the neutron irradiated sample. Since the neutron irradiated sample is inhomogeneously damaged the spectra I observe are dominated by the strong allowed first order scattering (sharp LO and TO peaks) from the 95% of the sample volume which is relatively undamaged while the weak DAFORS from the remaining 5% of the damaged cores is completely negligible.

2.6 Conclusions

In conclusion I have been able to observe new and relatively sharp peaks due to intrinsic defects in the Raman spectra of both neutron and electron irradiated GaAs. The symmetry and annealing dependence of one of the peaks at 227 cm^{-1} is consistent with its identification as a vibrational mode of an As vacancy. The use of incident photons tuned to just below the band gap has allowed me to simultaneously take advantage of both the relatively large scattering volume and a large resonant enhancement. This results in large scattering intensities for the defect related Raman processes. (In the electron irradiated sample rates were as high as several thousand photons/sec when counted by a PMT with 1% quantum efficiency.) This suggests that it should be possible to examine defect related scattering in samples with considerably lower defect concentrations.

While the narrow linewidths of peaks A and A' suggest that they are associated with well localized vibrations it is important to test this hypothesis with additional experiments. Two ideas which come quickly to mind are:

1) Since a Γ_1 local mode associated with an arsenic vacancy would

involve mostly Ga motion one immediately thinks of isotope substitution. Unfortunately there are no naturally occurring isotopes of either Ga or As. The next best thing would be to look at alloys such as GaAlAs or GaPAs. If the peaks A and A' were indeed V_{As} local modes that involved mostly motion of the nearest Ga neighbors then the frequency of these modes should be modified differently in GaAlAs as compared to GaPAs.

2) Observation of changes in the Raman spectrum induced by hydrostatic or uniaxial pressure.

A third possibility is that the observed resonant enhancement lineshape may shed some light on the degree of localization of the vibrational modes that participate in the defect related scattering. In the next chapter I will show that this is indeed the case.

References

1- The contents of this chapter have been partially presented in the following publications: R. S. Berg, P. Y. Yu and E. R. Weber, Proceedings of the XVII International Conference on the Physics of Semiconductors, San Francisco, ed. by J. Chadi and W.A.Harrision(Springer-Verlag, New York, 1985) p. 765; R. S. Berg, P. Y. Yu and E. R. Weber, Appl. Phys. Lett.,(to be published).

2- F. Cerdeira, T. A. Fjeldly and M. Cardona, Phys. Rev. B 9, 4344 (1974).

3- R. M. Feenstra, R. J. Hauenstein and T. C. McGill, Phys. Rev. B 28, 5793 (1983).

4- R. J. Hauenstein, R. M. Feenstra and T. C. McGill, Phys. Rev. B 29, 1858 (1984).

5- A. S. Barker and A. J. Sievers, Rev. Mod. Phys. 47, S1 (1975).

6- H. Richter, Z. P. Wang and L. Ley, Sol. St. Comm. 39, 625 (1981).

7- S. Ushioda, Sol. St. Comm. 15, 149 (1974).

8- K. K. Tiong, P. M. Amirtharaj, F. H. Pollak and D. E. Aspnes, Appl. Phys. Lett. 44, 122 (1984).

9- H. Kawamura, R. Tsu and L. Esaki, Phys. Rev. Lett. 29, 1397 (1972); R. Tsu, H.Kawamura and L. Esaki, Proceedings of the XI International Conference on the Physics of Semiconductors, p. 1135 (1972).

10- B. Jusserand and J. Sapriel, Phys. Rev. B 24, 7194 (1981).

11- N. Saint-Cricq, R. Carles, J. B. Renucci, A. Zwick and M. A. Renucci, Sol. St. Comm. 39, 1137 (1981).

12- R. Carles, A. Zwick, M. A. Renucci and J. B. Renucci, Sol. St. Comm. 41, 557 (1982).

13- R. Shuker and R. W. Gammon, Phys. Rev. Lett. 25, 222 (1970).

14- P. Parayanthal and F. H. Pollak, Phys. Rev. Lett. 52, 1822 (1984).

15- W. Hayes and R. Loudon, Scattering of Light by Crystals, John Wiley, New York, (1978).

16- R. Worner, U. Kaufman and J. Schneider, Appl. Phys. Lett. 40,141 (1982).

17- K. D. Glinchuk et. al., Sov. Phys. Semicond. 17, 471 (1983).

18- J. Hoffnagle, L. Ph. Roesch, N. Schlumpf and A. Weis, Opt. Comm. 42, 267 (1982).

19- K. Laithwaite and R. C. Newman, Phil. Mag. 35, 1689 (1977).

20- R. Coates and E. W. J. Mitchell, Adv. Phys. 24, 593 (1975).

21- J. Bourgoin and M. Lannoo, Point Defects in Semiconductors II, Springer-Verlag, Berlin 1983.

22- P. Y. Yu, Phys Rev B 20, 5286 (1979).

23- R. Carles, N. Saint-Cricq, J. B. Renucci, M. A, Renucci and A. Zwick, Phys. Rev. B 22, 4804 (1980).

24- E. R. Weber, in III-V Semi-insulating Materials, Warm Springs, 1984.

25- D. V. Lang, in Radiation Effects in Semiconductors, ed. by N. B. Urli and J. W. Corbett, Institute of Physics, London, 1976.

26- D. Pons and J. Bourgoin, Phys. Rev. Lett. 47, 1293 (1981).

27- L. J. Cheng, J. P. Karins, J. W. Corbett and L. C. Kimerling, J. Appl. Phys. 50, 2962 (1979).

28- D. Pons, A. Mircea and J. Bourgoin, J. Appl. Phys. 51, 4150 (1980).

29- S. Loualiche, A. Nouailhat, G. Guillot and M. Lannoo, Phys. Rev. B 30, 5822, (1984).

30- M. Cardona in Light Scattering in Solids II, p.19, ed. by M.

Cardona, Springer-Verlag, Berlin, (1982).

31- R. C. Leite, unpublished.

32- G. Dolling and R. A. Crowley, Proc. Phys. Soc. (London) 88, 463 (1966).

Figure Captions

Figure 2.1- Some results of defect related Raman scattering. a) Local modes of boron in silicon. From reference 2. b) DAFORS resulting from ion implantation of GaAs (upper curve) and comparison with calculated phonon density of states (lower curve). From reference 7.

Figure 2.2- Feynman diagrams- for various Raman processes discussed in the text. The various symbols used are defined within the figures. a) Third order Raman process in a crystalline semiconductor. b) Third order spatial correlation mechanism involving phonons of finite spatial extent. c) Mechanism of KTE that involves localized intermediate electronic states. d) Fourth order defect mediated process.

Figure 2.3- Experimental setup for recording Raman spectra.

Figure 2.4- Stokes Raman spectra for GaAs (110) surface recorded at 90 K. a) Unirradiated sample. b) Neutron irradiated sample; $\Gamma_1 + 4\Gamma_{12}$ symmetry scattering geometry. c) Electron irradiated sample; $\Gamma_1 + 4\Gamma_{12}$ symmetry scattering geometry. d) Electron irradiated sample; Γ_{15} symmetry scattering geometry. e) One phonon density of states calculated using a shell model from Reference 32. For spectra (b), (c) and (d) the incident photon had a frequency of 11900 cm^{-1}. For the spectrum a) the 19436 cm^{-1} line of the Ar^+ laser was used instead to avoid the strong band gap luminescence. The amplitudes of the spectra have been rescaled for ease of comparison. For example, the Γ_{15} symmetry spectrum shown in (d)is actually 10 times weaker than the Γ_1

+ $4\Gamma_{12}$ spectrum of spectrum(c). Comparison of spectra (b) and (c) to spectra recorded in a $\Gamma_1 + \Gamma_{12} + \Gamma_{15}$ scattering geometry has shown that the Γ_{12} component in these spectra is negligible compared to the Γ_1 component.

Figure 2.5- Stokes Raman spectra recorded in $\Gamma_1 + 4\Gamma_{12}$ symmetry from (110) surface of GaAs. a) Unirradiated sample. b) GaAs doped with 10^{17} cm^{-3} Cr. c) Neutron irradiated sample.

Figure 2.6- Stokes Raman spectra recorded for the neutron irradiated sample following one hour isochronal annealing treatments. The intensity of the spectrum for the sample annealed to 220 C is unchanged compared to the unannealed sample (figure 2.4b).

Figure 2.7- Raman spectra in electron irradiated GaAs recorded at a point where the electron dosage is lower than the maximum dosage by roughly a factor of 6.

Figure 2.8- Simple example showing the consequences of the spatial correlation model on the DAFORS lineshape. a) Model dispersion relation used for the purposes of this example: $\omega = 1 - \exp(-2qa)$ for $0 < q < q_{BZ} = \pi/a$. b) Phonon density of states corresponding to the dispersion relation of part a). c) Four different momentum relaxation functions F(q) of the form $\exp(-q^2L^2/2)$ with L = 0.5,0.75,1.0,2.0. d) Raman spectrum predicted by eqn. 2.2.11 for the four different correlation lengths of part c).

Figure 2.9- Comparison of the Raman lineshape observed in regions irradiated with different doses of electrons. a) Spectrum recorded 1.5 mm from point of maximum irradiation (labelled "2"). Shown for comparison is a spectrum recorded at point of maximum irradiation (labelled "1"). These spectra are scaled so that the intensities of the TO phonons are equal. The difference in the intensity of the defect related scattering is assumed to be due to a difference in defect concentration. b) Same as in a) except that the spectra are scaled so that the intensities of peak C are equal, so as to facilitate a comparison of the lineshapes.

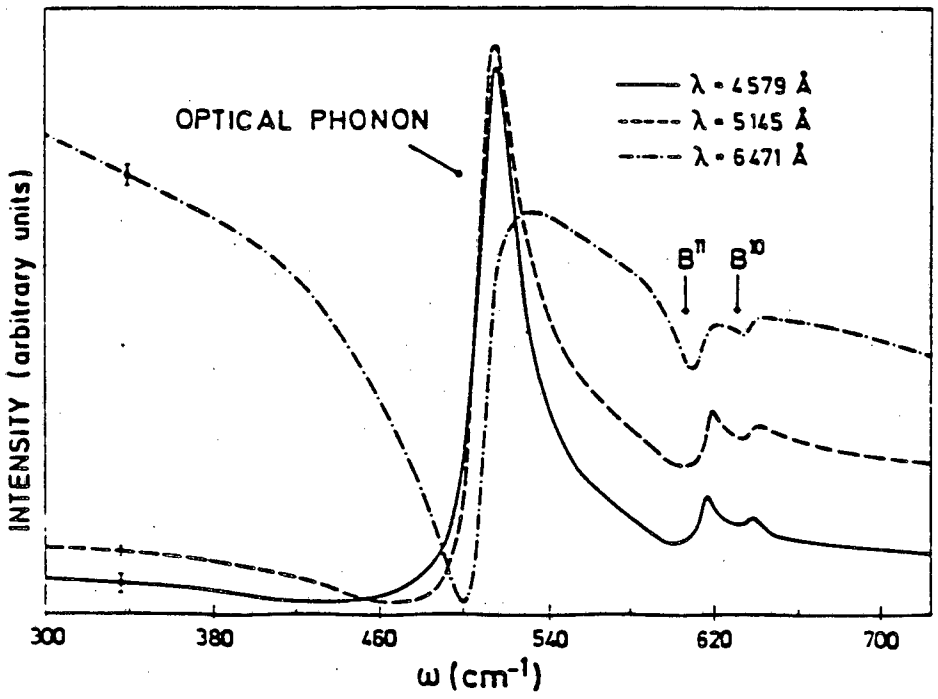

Figure 2.1a

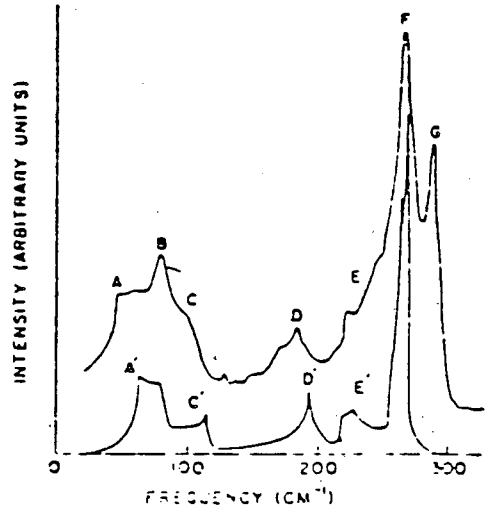

Figure 2.1b

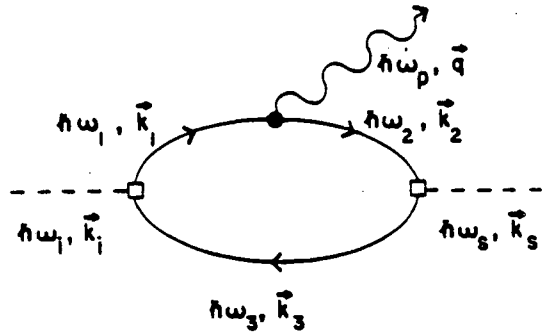

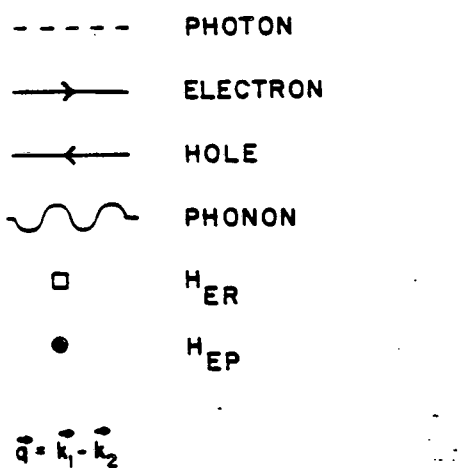

Figure 2.2a

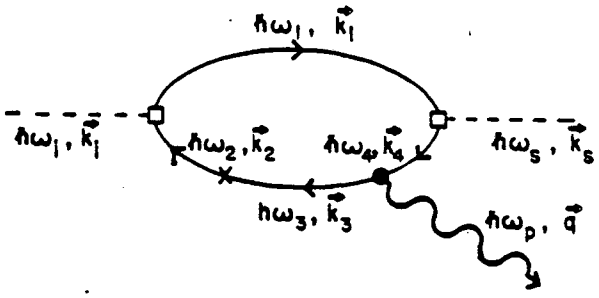

Figure 2.2d

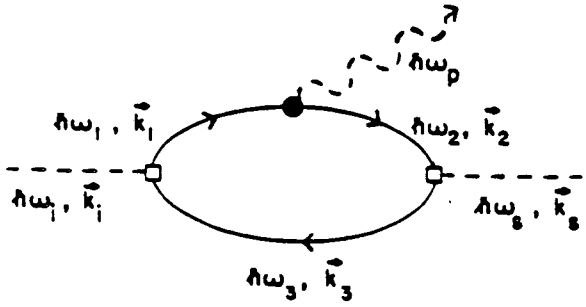

Figure 2.2b

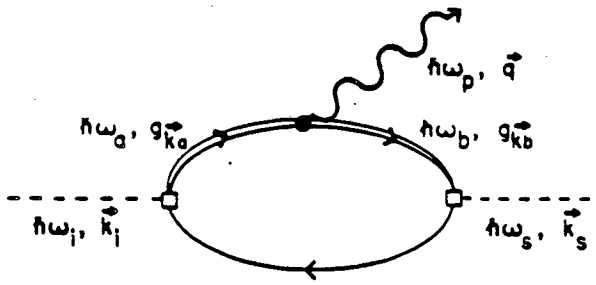

Figure 2.2c

Figure 2.2

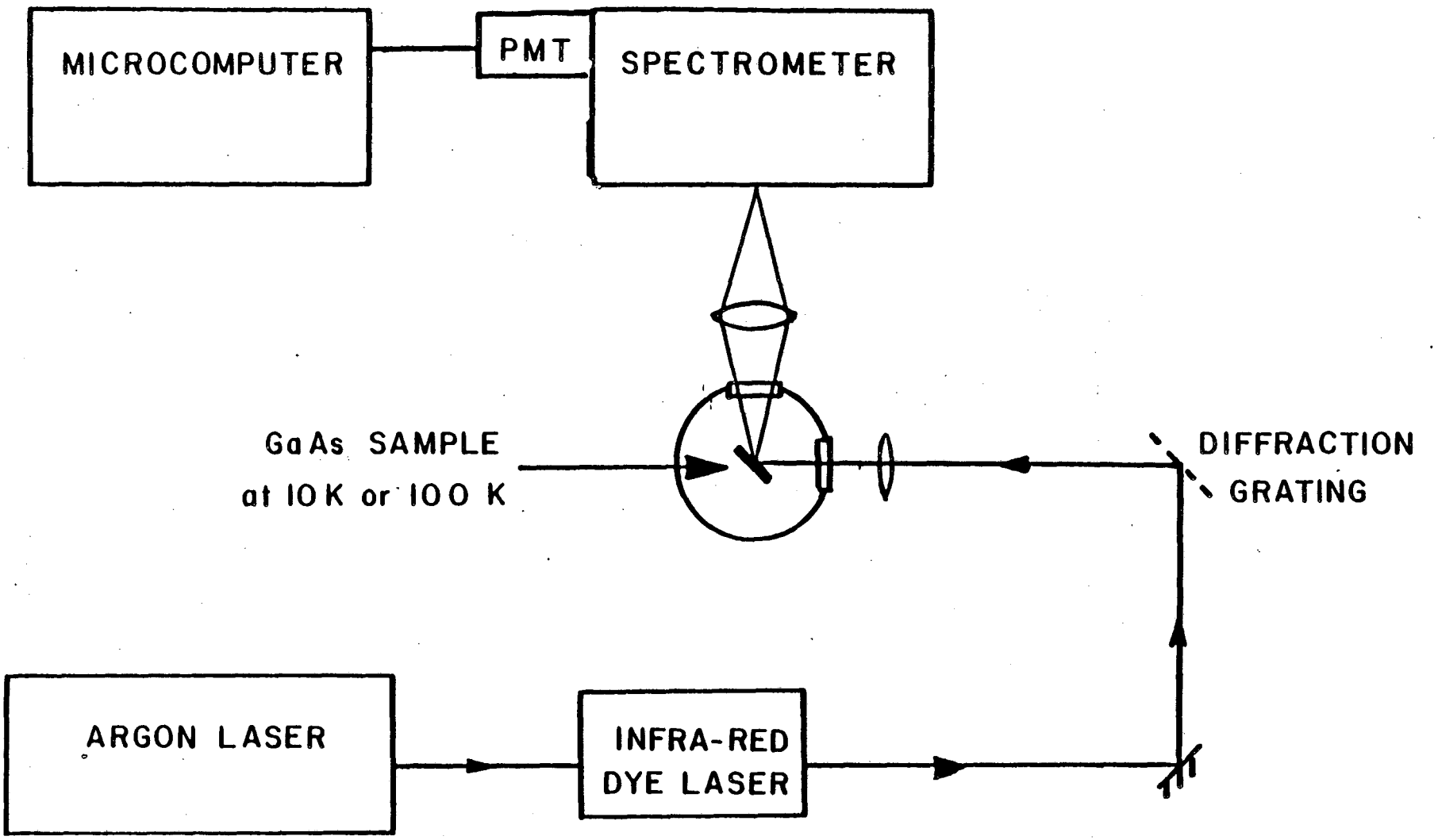
MICROCOMPUTER
PMT
SPECTROMETER
GaAs SAMPLE
at 10K or 100 K
DIFFRACTION
GRATING
ARGON LASER
INFRA-RED
DYE LASER

Figure 2.3

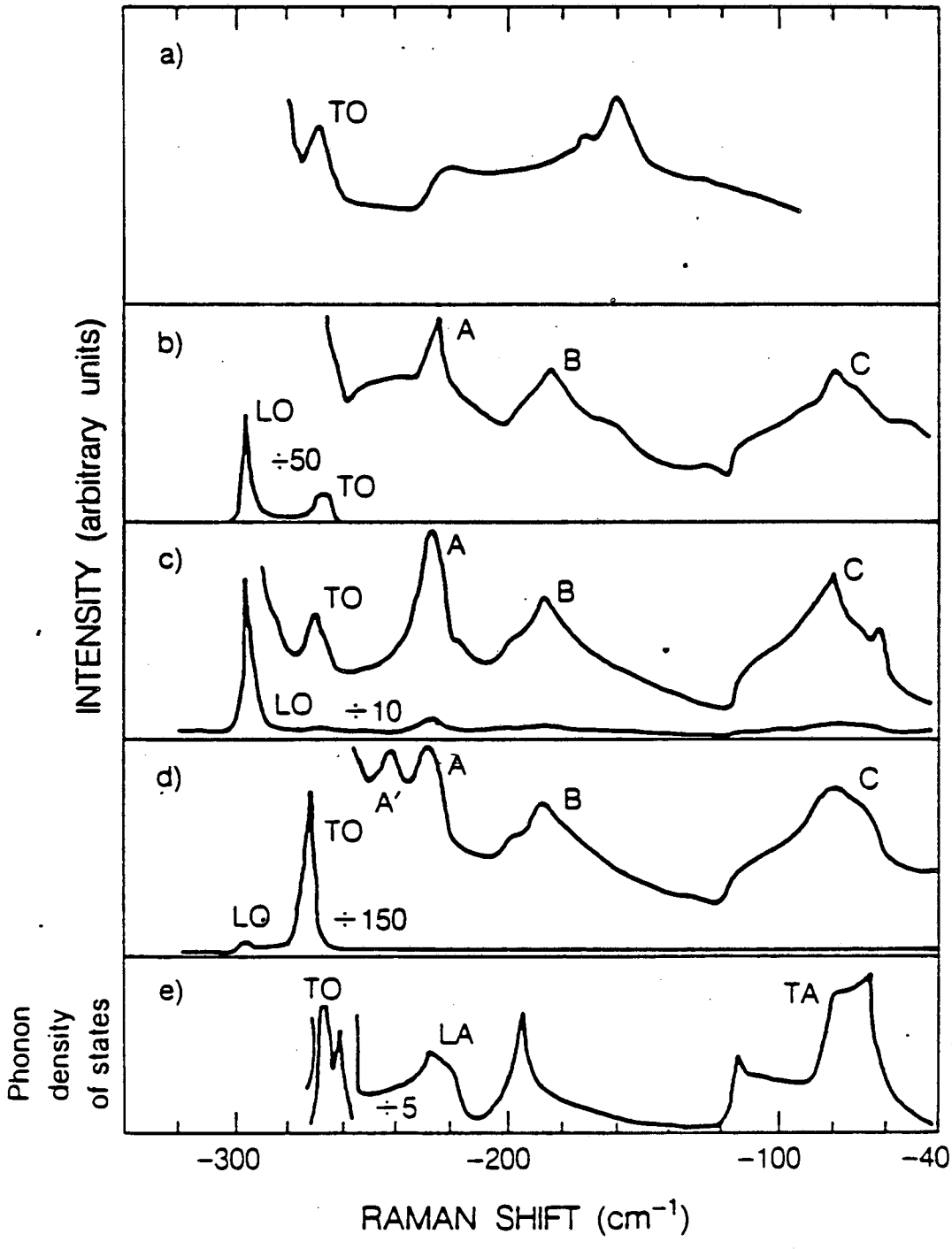

Figure 2.4

XBL 853-10143

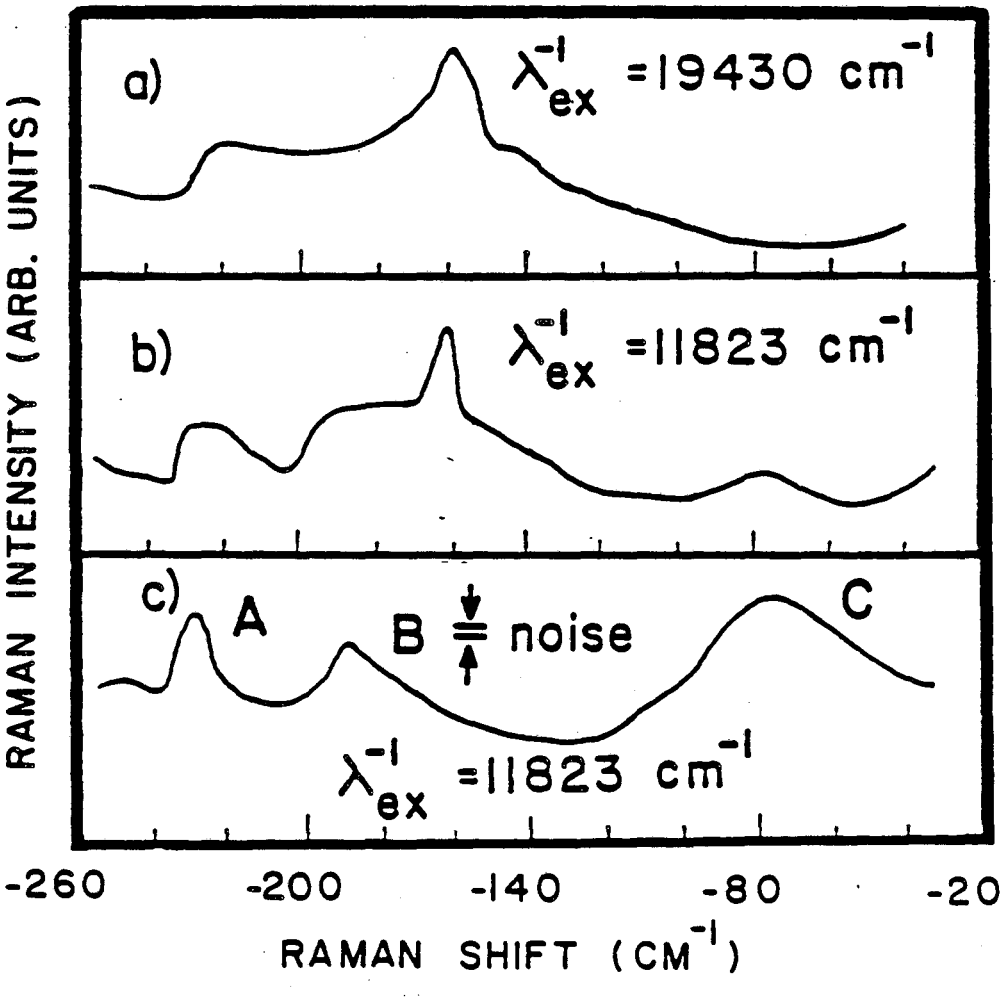
a)
λ_{ex}^{-1} =19430 cm^{-1}
b)
λ_{ex}^{-1} =11823 cm^{-1}
c)
A
B
noise
C
λ_{ex}^{-1} =11823 cm^{-1}
RAMAN INTENSITY (ARB. UNITS)
-260
-200
-140
-80
-20
RAMAN SHIFT (CM^{-1})

Figure 2.5

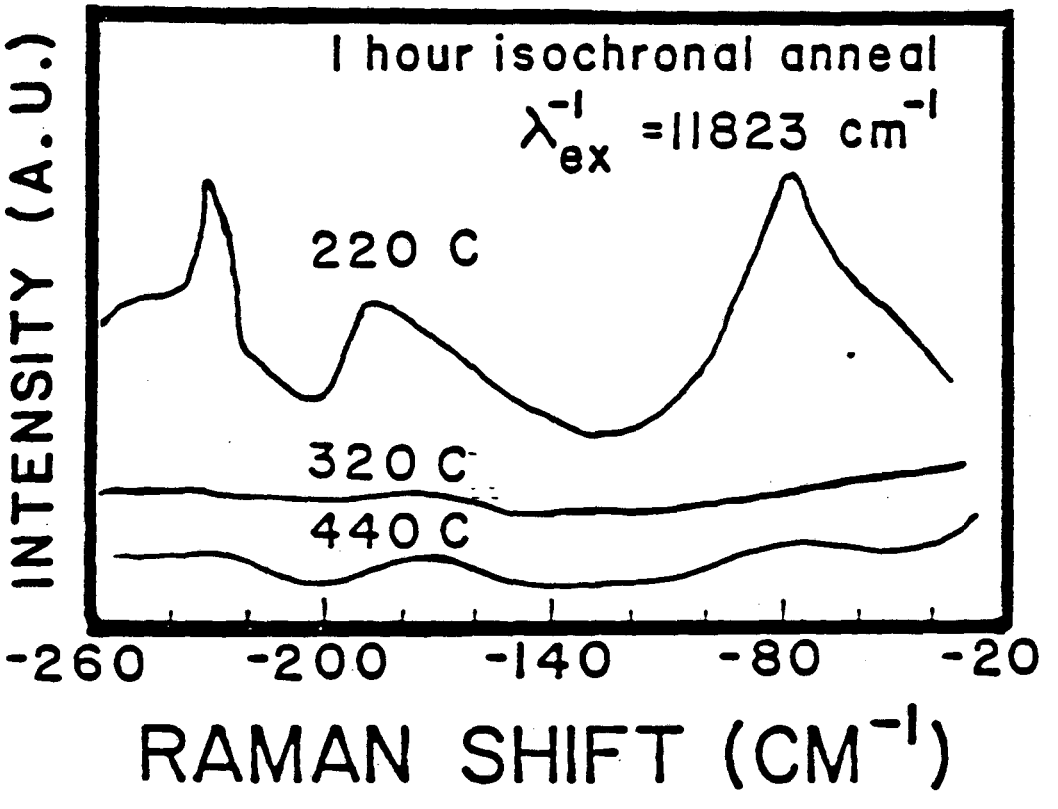

XBL 855-2645

Figure 2.6

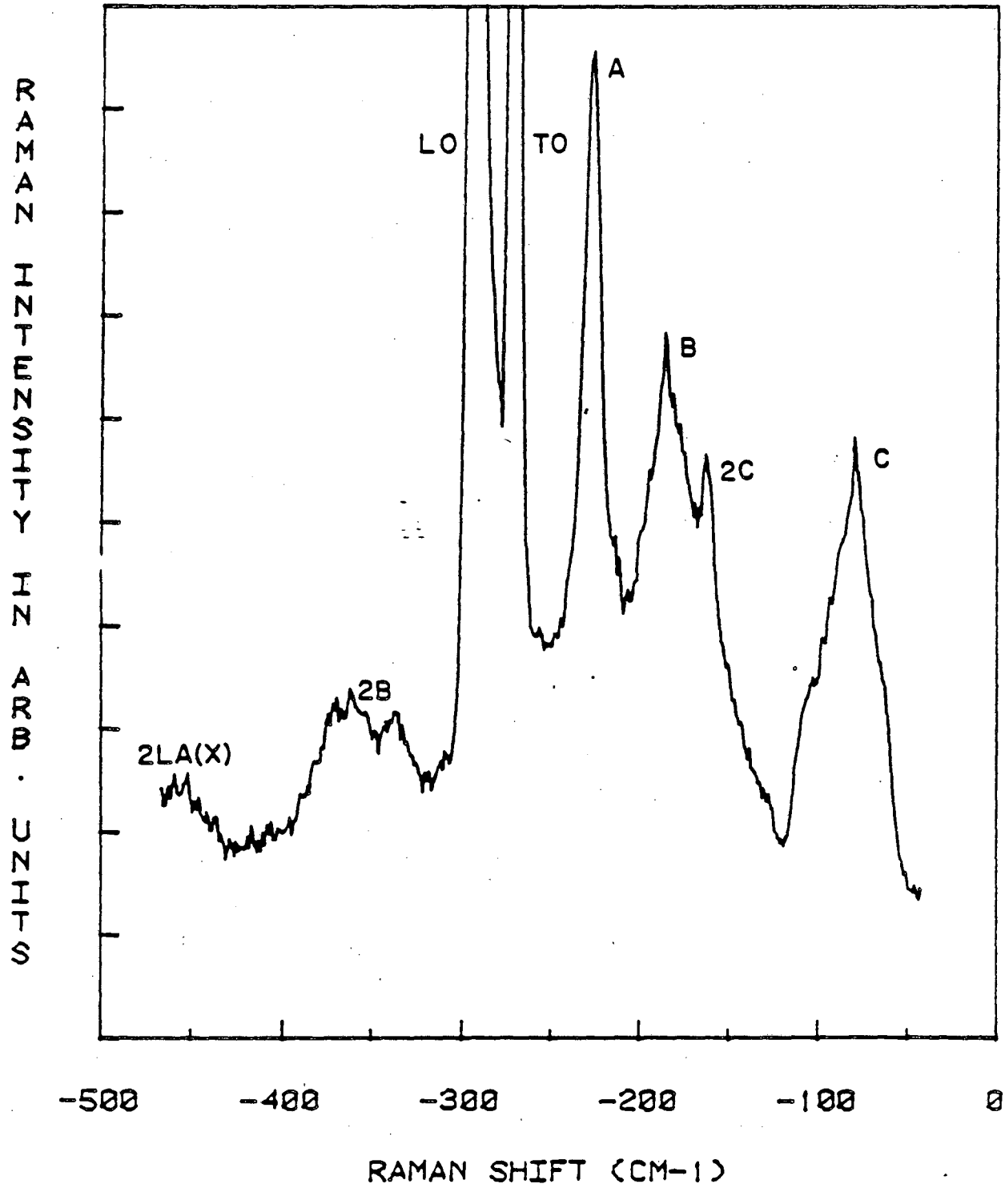
RAMAN INTENSITY IN ARB. UNITS
LO
TO
A
B
2C
C
2B
2LA(X)
-500
-400
-300
-200
-100
0
RAMAN SHIFT (CM-1)

Figure 2.7

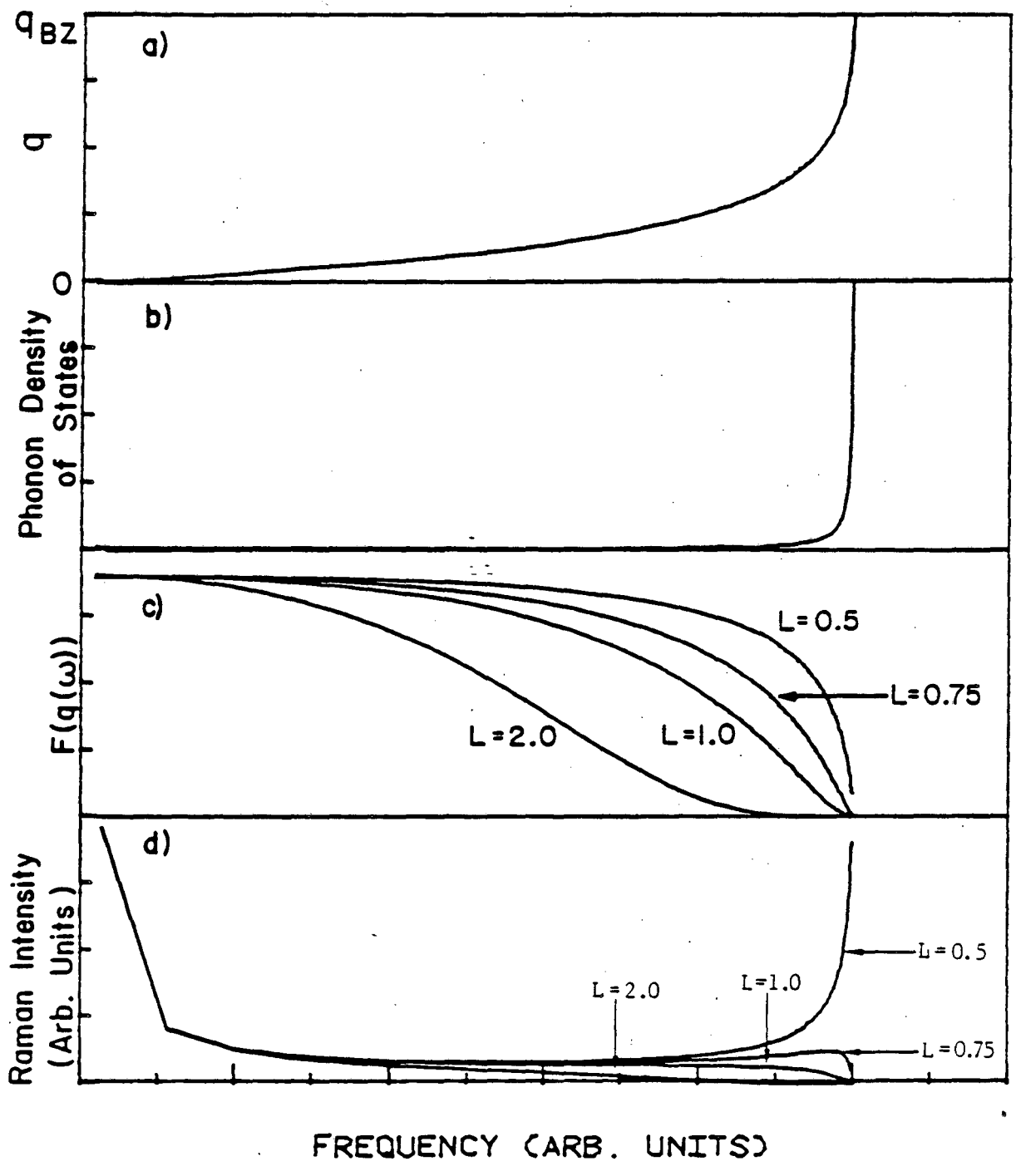
q_{BZ}
q
0
a)
b)
Phonon Density of States
c)
F(q(ω))
L=0.5
L=0.75
L=2.0
L=1.0
d)
Raman Intensity (Arb. Units)
L=0.5
L=2.0
L=1.0
L=0.75
FREQUENCY (ARB. UNITS)

Figure 2.8

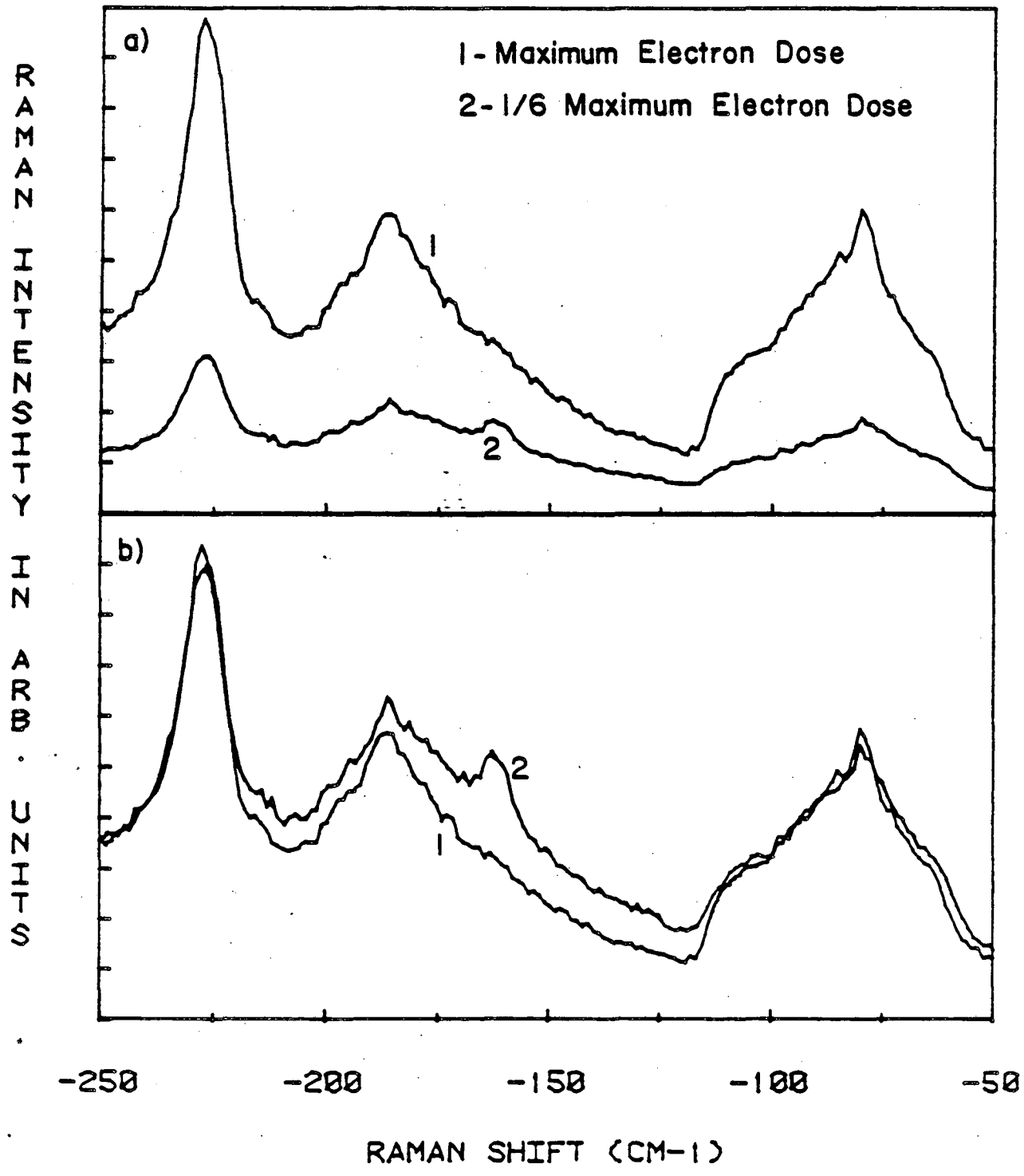
a)
1 - Maximum Electron Dose
2 - 1/6 Maximum Electron Dose
1
2
b)
2
1
RAMAN INTENSITY IN ARB. UNITS
-250
-200
-150
-100
-50
RAMAN SHIFT (CM-1)

Figure 2.9

CHAPTER 3

Chapter 3

Resonant Raman Study of Intrinsic Defect Related Modes in GaAs

3.1 Introduction

In chapter 2 I examined the defect induced Raman scattering found in neutron and electron irradiated GaAs. In this chapter I discuss the use of resonant Raman scattering (RRS) to study intrinsic defects in GaAs. Specifically, I present results on the variation of the Raman cross section for this defect related scattering as a function of incident photon energy in the vicinity of the E_0 gap.

The motivation for studying RRS is several-fold:

1) The large resonant enhancement provides a means of increasing the sensitivity of Raman scattering as a tool to study defects. Thus one goal is to understand the physics underlying the resonant enhancement so as to ~~best~~ better be able to take advantage of it. There are two possible scenarios for how the sensitivity is increased. The first is simply an across the board increase in the intensity of all the phonon modes. Secondly, there exists the possibility of selective enhancement in which the mode of interest is enhanced more than the other modes. Such selective enhancement can be useful for a number of reasons. For example it can result in an increase in the strength of the signal relative to a competing background. (A case in point is depicted in figure 2.9, where the disorder related modes are partially masked by the two -phonon overtone modes.) Also, in this study I have introduced large concentrations of intrinsic defects into GaAs by

irradiating samples with either high energy neutrons or electrons. While this technique generates relatively high concentrations of intrinsic defects it is not a selective technique in that it inevitably creates a number of different types of defects. Thus it can be difficult to sort out which Raman mode is due to which defect. RRS offers the possibility of selectively enhancing a particular type of mode induced by defects. For example, I argue that here as the phonons that participate in the disorder related scattering become more localized, the corresponding resonance enhancement becomes sharper. In some situations one can tune the incident photons to resonate with electronic transitions associated with specific defects, thereby selectively enhancing the corresponding scattering. This would aid in the identification of defects.

2) The enhancement lineshape of a Raman mode provides information concerning the electron-phonon interaction and the nature of the scattering mechanism. In particular, I show in this chapter that the RRS lineshape for the defect related scattering can be explained by a fourth order scattering process that involves a $\vec{q}$-independent electron-phonon interaction.

Since RRS is an excitation spectroscopy it is possible to study excited electronic states that would not be accessible by techniques such as photoluminescence. Thus a connection can be made between information that is obtained from RRS and that obtained from other techniques. As shown in chapter 2, Raman scattering gives information regarding the vibrational modes associated with defects. Such information is valuable because the nature of these vibrational modes can be used to draw conclusions about the microscopic identity of the

associated defect. Ultimately though, such information is most useful when a correspondence can be made with the defect energy levels provided by other techniques, such as DLTS. RRS potentially provides the means to make this connection. While the above was part of the original motivation for undertaking this RRS study, I should state at the outset that I have found no evidence that compels me to invoke such localized electronic intermediate states to explain my results. Such a mechanism may however be applicable to the case where the incident photon energy is tuned through deep levels in the gap.

Several previous studies have focussed on the resonant behavior of defect related Raman scattering. For example, Bedel et. al.[1] studied the resonance behavior of DAFORS modes in the alloy system $InAs_xP_{1-x}$ in the vicinity of the E_1 critical point. They observed a relatively small resonant enhancement for these modes. Yu et. al.[2] used RRS to study CdS:Cl. They tuned the energy of the scattered photons through an electronic level corresponding to an exciton bound to a shallow acceptor. By observing a large enhancement in the Raman scattering of a V_{Cd}-Cl$_S$ complex they were able to deduce that such complexes form a shallow acceptor in CdS. Wolford et. al.[3] used this technique to study the deep level N in $Al_xGa_{1-x}As$. Usually in these III-V alloys inhomogeneous broadening due to differences in the local environment prevents much useful information from being obtained from the defect assisted recombination luminescence. However, by tuning the incident photon energy Wolford et.al. were able to circumvent the inhomogeneous broadening by selectively exciting only a narrow distribution of the N centers. By observing the details of the now observable phonon replicas, they were able to deduce information concerning the electronic wave function of the N level.

3.2 Theory of Resonant Raman Scattering in a Perfect Crystal

3.2a General Description

To understand the kind of information that can be obtained by RRS it is necessary to return to the microscopic expression derived from time dependent perturbation theory with the goal of determining how the scattering cross section varies as a function of the incident photon energy:

$$\sigma(\omega_i) \propto \left| \sum_{\vec{k}_a} \frac{\langle f|H_{ER}|b\rangle \langle b|H_{EP}|a\rangle \langle a|H_{ER}|i\rangle}{(\omega_a - \omega_i)(\omega_b - \omega_s)} \right|^2 \qquad (3.2.1)$$

When the incident photon energy coincides with the energy of an electronic transition then the resonant denominators will become very small (an imaginary damping component added to the electronic energies prevents the denominators from becoming zero) and the cross section will be large. Let us first consider a special case of equation 3.2.1 where there is a single isolated intermediate state whose energy is $\hbar\omega_0$. (see figure 3.1a) In this case 3.2.1 reduces to:

$$\sigma(\omega_i) \propto \left| \frac{1}{(\omega_0 - \omega_i)(\omega_0 - \omega_s)} \right|^2 \qquad (3.2.1a)$$

The behavior of the cross section as a function of incident photon frequency in the vicinity of ω_0, assuming finite damping, is depicted in the right hand side of figure 3.1a. The result is two

peaks that are symmetric about $\omega_0 + \omega_p/2$ and located at ω_0 and $\omega_0 + \omega_p$ (solid line). These two peaks are referred to as the ingoing and outgoing resonances respectively. In this case only one of the two factors in the denominator of (3.2.1) vanishes at a time and they never vanish simultaneously. In practice broadening often causes the two peaks to merge into one peak that is symmetric about $\omega_0 + \omega_p/2$ (dashed line).

In the more general case of RRS in a solid with a band structure, where there are many possible intermediate states, it is often necessary to consider only the most strongly resonant terms in equation 3.2.1. For example, those portions of the band structure that have transition energies near the incident photon energy will make the dominant contribution to the cross section. Also, only one time ordering (the one shown in figure 2.2a) contributes significantly. In weighing the relative contributions from various types of scattering processes it is convenient to separate them into two classes referred to as two-band and three band processes. These processes are depicted schematically in figure 3.2. As implied by the names, in the two-band process only two bands are involved so the electron or hole remains in the same band when emitting a phonon while in the three band process the electron or hole scatters to a new band.

Consider a two band process in a perfect crystal (e.g. figure 3.2a). Quasi-momentum conservation implies that the phonon wave vector $q = 0$. Therefore, for a typical band structure $\omega_a = \omega_b$, since quasi-momentum is conserved at every vertex. The resonant denominator in equation 3.2.1 at, for example, the ingoing resonance ($\omega_i = \omega_0$) is

$$(i\Gamma_a)\ (i\Gamma_a + \omega_i - \omega_s) = (i\Gamma_a)\ (i\Gamma_a + \omega_p) \qquad (3.2.1b)$$

where a damping Γ_a has been added. On the other hand, for the three band process shown in figure 3.2b the resonant denominator in equation 3.2.1 at the ingoing resonance is

$$(i\Gamma_a)\ (i\Gamma_a + \omega_i + \Delta - \omega_s) = (i\Gamma_a)\ (i\Gamma_a + \Delta + \omega_p) \qquad (3.2.1c)$$

where Δ is the separation between the two valence bands. Comparison of equations 3.2.1b,c shows that if $\Delta >> \omega_p$ then the three band terms will not be signigicant compared to the two band terms.

RRS allows us to focus on contribution from a small portion of the band structure and gain information on scattering processes that occur via these electronic states. In contrast, in the off resonance case, information regarding specific electronic transitions and H_{ER} and H_{EP} is lost due to the summation over all of the intermediate states.

The behavior of the ingoing and outgoing resonances for the case of a semiconductor with a simple model band structure is shown in figure 3.1b. In this case it is necessary to perform the sum indicated in (3.2.1). It is found that $\sigma(\omega_i)$ again exhibits peaks at $\omega_i = \omega_0$ and $\omega_i = \omega_0 + \omega_p$. In contrast to the example in figure 3.1a, these two peaks are no longer symmetric about $\omega_i = \omega_0 + \omega_p/2$. This is because now when ω_i is tuned so that $\omega_s = \omega_0$ (the outgoing resonance), there is the possibility that the incident photon will also be resonant with a real transition. Thus both terms in the resonant denominator can

simultaneously be very small (double resonance). On the other hand, a double resonance is clearly not possible at the ingoing resonance. The result is that the outgoing resonance can be much stronger than the ingoing resonance. Therefore $\sigma(\omega_i)$ tends to peak at the outgoing resonance and is "sharper" if double resonance effects are possible.

Double resonance effects will be strongest when it is possible to conserve energy in all of the steps in the Raman process. This is the situation that is depicted in figure 3.1b for the outgoing resonance. Ordinarily though, in a one phonon process the phonon momentum is small so the restrictions imposed by momentum conservation prevent this from occurring. This is the situation shown in figure 3.1c.

The key to deriving a correct expression for $\sigma(\omega_i)$ from equation 3.2.1 is to properly perform the sum over the intermediate states. It is necessary to coherently sum (i.e. maintaining proper phase relationships) over a range of both real and virtual intermediate states. Thus the problem reduces to properly evaluating a contour integral in the complex plane. Let us now see how this is done for a variety of different cases.

3.2b Allowed TO Phonon Scattering

We wish to evaluate $\sigma(\omega_i)$ for the case of allowed one TO phonon scattering in the vicinity of the E_0 critical point in GaAs. Such a calculation has been performed by a number of authors.[4,5] I present here results similar to those of Cardona.[5] (Since I am interested in predicting the RRS lineshape I use as a starting point equation (3.2.1) which includes only the most resonant term. Cardona's treatment includes some less dispersive terms which do not appreciably

affect the lineshape close to resonance.) The following assumptions were made:

1) Only two band terms are included. In GaAs the critical point that lies closest to the E_0 critical point is the $E_0 + \Delta_0$ critical point, which is 2400 cm^{-1} away. This separation is large compared to ω_{TO} = 270 cm^{-1}. In light of the discussion of section 3.2a it is therefore a good approximation to neglect the three-band terms. As discussed above, the assumption that momentum is conserved implies that the phonon $\vec{q} \approx 0$ and for a two-band process this means that $\omega_a \approx \omega_b$.

2) The matrix elements in (3.2.1) are assumed to be constants independent of ω_a and can therefore be taken outside of the summation.

3) The intermediate states are a single set of parabolic bands. The dispersion of the conduction (valence) band is given by

$$\omega_{c(v)} = \vec{k} \cdot \frac{\hbar}{2\overleftrightarrow{m}_{c(v)}} \cdot \vec{k} \qquad (3.2.2)$$

where the $\overleftrightarrow{m}_{c(v)}$ are the effective mass tensors. Thus

$$\omega_a = \omega_c - \omega_v = \omega_0 + \hbar/2\left(\vec{k} \cdot \frac{1}{\overleftrightarrow{m}^*} \cdot \vec{k}\right) \qquad (3.2.3)$$

where

$$\frac{1}{\overleftrightarrow{m}^*} = \frac{1}{\overleftrightarrow{m}_c} + \frac{1}{\overleftrightarrow{m}_v} \qquad (3.2.4)$$

For a M_0 critical point such as the E_0 gap, the effective mass tensors

are positive definite and the joint density of states $N_d(\omega_a)$ exhibits the familiar $E^{1/2}$ dependence:

$$N_d(\omega_a) = \frac{\sqrt{2}}{\pi^2} m_d^{3/2}(\omega_a - \omega_0)^{1/2} \quad ; \ \omega_a > \omega_0 \qquad (3.2.5)$$

$$= 0 \ ; \ \omega_a < \omega_0$$

where

$$m_d \equiv (m^*_1 m^*_2 m^*_3)^{1/3}$$

and m^*_i are the principal components of the effective mass tensor. Note that the assumption that the intermediate states are uncorrelated electron-hole pairs implies that exciton effects are neglected. Qualitatively one expects the inclusion of exciton effects to shift the $\sigma(\omega_i)$ curve downward in energy by an amount on the order of the exciton binding energy (34 cm^{-1} in GaAs) and to cause a sharpening of the resonance.[5]

Making use of these assumptions and transforming the sum in (3.2.1) into an integral yields:

$$\sigma_{TO}(\omega_i) \propto \left| \int \frac{d\omega_a N_d(\omega_a)}{(\omega_a - \omega_i)(\omega_a - \omega_s)} \right|^2 \qquad (3.2.6)$$

Let us define

$$A(\omega) \equiv \int \frac{d\omega_a N_d(\omega_a)}{\omega_a - \omega} \qquad (3.2.7)$$

($A(\omega)$ is proportional to the linear optical susceptibility.) Then $\sigma_{TO}(\omega_i)$ can be expressed as

$$\sigma_{TO}(\omega_i) \propto \left| \frac{A(\omega_i) - A(\omega_s)}{\omega_p} \right|^2 \qquad (3.2.8)$$

Evaluating (3.2.7) by using a contour integral in the complex plane leads to:

$$\sigma_{TO}(\omega_i) \propto \frac{1}{\Delta^2} \left| \frac{F\left(\frac{x}{1+\Delta}\right)}{(1+\Delta)^{3/2}} - \frac{F\left(\frac{x}{1-\Delta}\right)}{(1-\Delta)^{3/2}} \right|^2 \qquad (3.2.9)$$

where

$$\Delta \equiv \omega_p/2\omega_0; \quad x \equiv \frac{\omega_i}{\omega_0 + (\omega_p/2)}; \qquad F(x) \equiv \frac{(1-x)^{1/2}}{x^2}$$

A plot of this result with parameters appropriate to one TO phonon scattering at the E_0' critical point of GaAs is shown in figure 3.3 for the case of zero damping. Note that two peaks occur at $\omega_i = \omega_0$ and $\omega_s = \omega_0$ corresponding to the ingoing and outgoing resonances. The lineshape is approximately symmetrical. As discussed above in reference to figure 3.1c, because of the constraints imposed by quasi-momentum conservation there is no effect of double resonance.

The effect of damping can be incorporated by adding an imaginary part Γ to the frequency ω_0. The resulting effects will be significant only when Γ is appreciable compared to ω_p. Otherwise the width of the resonance is roughly ω_p.

3.2c Forbidden LO Phonon Scattering

According to the selection rules listed in Table 1.2, Raman scattering involving one LO phonon is not allowed in GaAs when the spectrum is recorded in a backscattering configuration from a (110) surface. Nonetheless, the experimental spectra displayed in figure 2.4 show strong LO phonon scattering. This type of forbidden scattering has been observed previously by many workers.[5] The forbidden scattering has been found to exhibit a very strong resonant behavior near critical points such as E_0 and $E_0 + \Delta_0$. Away from these critical points the forbidden scattering becomes so weak that it is unobservable. Also it has been observed experimentally that the forbidden scattering exhibits predominantly Γ_1 symmetry ; i.e. the scattered light is polarized parallel to the incident light. In this section I present a theoretical explanation of this forbidden scattering based on the assumption that the scattering medium is a perfect crystal. The treatment follows that given by Cardona[5].

The underlying reason for the forbidden LO scattering is the macroscopic electric field $\vec{E}$ associated with an LO phonon. The interaction energy of an electron (hole) in the presence of this field was shown by Frohlich to be $-(+)\ ieE/|\vec{q}|$ and the interaction bears his name. It is the $\vec{q}$-dependence of the interaction that ultimately accounts for the forbidden scattering.

As in the case of the TO phonon, a calculation of the scattering cross section involves evaluating the perturbation theory expression (equation 3.2.1) corresponding to the Feynman diagram shown in figure 2.2a with H_{EP} assumed to be the Frohlich interaction. To do this a complicated integration over the intermediate states must be

performed. The details of the calculation tend to obscure the underlying physics. Therefore I first present a simplified treatment that yields the essential features. It is assumed in this treatment that $\omega \dashrightarrow 0$ so that $\omega = \omega$.
p i s

Due to the $|\vec{q}|^{-1}$ dependence of the Frohlich interaction, the cross section calculated for a diagram such as the one shown in figure 2.2a diverges in the limit $q \dashrightarrow 0$. However, it is necessary to consider two such diagrams: one in which the Frohlich interaction couples two electrons and a second in which two hole states are coupled. Because the charges of the electron and hole are equal and opposite these two terms cancel. However, since the expression for the scattering cross section contains an explicit $\vec{q}$-dependence we are led to carry out the calculation to a higher order in $\vec{q}$. (Recall that while quasi-momentum conservation implies that $\vec{q}$ is small, it is still finite.) In terms of the Raman tensor this can be expressed as:

$$\overleftrightarrow{R}(\vec{q}) = \overleftrightarrow{R}(0) + \left.\frac{d\overleftrightarrow{R}}{d\vec{q}}\right|_{\vec{q}=0} \vec{q} + \left.\frac{d^2\overleftrightarrow{R}}{d\vec{q}^2}\right|_{\vec{q}=0} :\vec{q}\vec{q} + \ldots \qquad 3.2.10$$

The term linear in $\vec{q}$ must also vanish as can be seen from the following argument: Since the hamiltonian H_{EP} depends only on $|\vec{q}|^{-1}$, the scattering cross section cannot depend on the direction of $\vec{q}$ so that $d\overleftrightarrow{R}/d\vec{q} = 0$.

In order to choose an appropriate form for the term that is second order in $\vec{q}$ let us first consider the mechanism by which the Raman tensor depends on $\vec{q}$. Figure 3.4a(b) shows the transitions involved in a process in which electrons (holes) are scattered by phonons with wave vector $\vec{q}$. In this simplified treatment it is assumed

that $\omega_p \dashrightarrow 0$ so that $\omega_i = \omega_s$. Because of the constraints imposed by quasi-momentum conservation the threshold energy for the valence to conduction band transitions is raised above ω_0. If parabolic bands are assumed then the $\vec{q}$-dependent effective gap is given by:

$$\omega_0(q) = \omega_0 + (\hbar/2)m_{c(v)}^{-1}(q/2)^2 \qquad (3.2.11)$$

Now, the susceptibility $\overleftrightarrow{\chi}(\omega)$ is a measure of the reponse of the electronic system when driven at frequency ω. Obviously this response will depend on the electronic resonance frequencies $\omega_0(\vec{q})$.) Therefore the magnitude of the modulation of $\overleftrightarrow{\chi}$ caused by a phonon will depend on the phonon $\vec{q}$. Recalling equation 1.2.6, which relates the Raman tensor to the magnitude of the susceptibility modulation, the second order term can be written:

$$\left.\frac{d^2\overleftrightarrow{R}}{d\vec{q}^2}\right|_{\vec{q}=0} : \vec{q}\vec{q} \propto |\vec{q}|^{-1} \frac{\partial^2 R}{\partial\omega_0^2}\left(\left.\frac{\partial^2\omega_0}{\partial q^2}\right|_c - \left.\frac{\partial^2\omega_0}{\partial q^2}\right|_v\right) : \vec{q}\vec{q} \qquad (3.2.12)$$

where the two terms correspond to the two processes indicated in figure 3.4.

Inserting equation 3.2.11 into equation 3.2.12:

$$\left.\frac{d^2R}{d\vec{q}^2}\right|_{\vec{q}=0} : \vec{q}\vec{q} \propto \frac{\vec{q}}{|\vec{q}|}\cdot\left(\overleftrightarrow{m}_c^{-1} - \overleftrightarrow{m}_v^{-1}\right)\cdot\vec{q}\,\frac{\partial^2\overleftrightarrow{R}}{\partial\omega_0^2} \qquad (3.2.13)$$

The main feature to note in this result is that the Raman tensor is linear in $|\vec{q}|$. Also, in the limit that the effective mass tensors are isotropic the Raman tensor is isotropic and the scattering is of Γ_1 symmetry. The breakdown of the standard selection rules for this $\vec{q}$-

dependent mechanism is not surprising. This is because the selection rules were derived using symmetry arguments that assumed that the phonons possesed the full symmetry of the point group of the crystal, i.e. $\vec{q}=0$ (see footnote 11 of chapter 1).

The main ingredient in the above description was the $\vec{q}$-dependence of the effective energy gap. This feature is carried over to the full scale microscopic treatment based on perturbation theory (i.e. equation 3.2.1). The simplifying assumption is made that the bands are isotropic, which as mentioned in section 1.2b is not a very good assumption. For the E_0 critical point the perturbation theory result can be expressed as:

$$\sigma_{LO}(\omega_i) \propto \left| \frac{P^2}{|\vec{q}|} \sum_{\vec{k}} (\omega_i - \omega_0 - \frac{\vec{k}^2}{2m^*})^{-1} \cdot \left[\left(\omega_i - \omega_0 - \omega_{LO} - \frac{(\vec{k} - S_c\vec{q})^2}{2m^*} \right)^{-1} - \left(\omega_i - \omega_0 - \omega_{LO} - \frac{(\vec{k} + S_v\vec{q})^2}{2m^*} \right)^{-1} \right] \right|^2 \qquad (3.2.14)$$

where $S_{c(v)} \equiv \frac{m_{c(v)}}{m_c + m_v}$

and $\vec{k}$ is the electron/hole wave vector and where P denotes the matrix element of H_{ER} which is assumed to be a constant independent of $\vec{k}$. The two terms in parentheses correspond to the two processes shown in figure 3.4. Carrying out the integration over $\vec{k}$ leads eventually to:

$$\sigma_{LO}(\omega_i) \propto \left| \frac{P^2}{|q|} \left(\Xi(\vec{q}S_c) - \Xi(\vec{q}S_v) \right) \right|^2 \qquad (3.2.15)$$

where

$$\Xi(\vec{q}) = (4\pi|\vec{q}|)^{-1} \tan^{-1} \left[i\vec{q}(2m^*)^{-\frac{1}{2}} \omega_{LO}^{-1} \left((\omega_i - \omega_0)^{\frac{1}{2}} - (\omega_s - \omega_0)^{\frac{1}{2}} \right) \right]$$

For small $\vec{q}$, the intensity of the scattering is found to be quadratic in $|\vec{q}|$. Shown in figure 3.3 is the behavior of $\sigma_{LO}(\omega_i)$ predicted by

equation (3.2.15) using parameters appropriate to the E_0 critical point in GaAs. The lineshape is seen to be symmetrical about $\omega_0 + \omega_{LO}/2$ indicating that double resonance effects are not strong in this case either. This lineshape can be compared to the lineshape for the allowed TO phonon scattering. Note that the forbidden LO phonon cross section falls rapidly to zero on either side of the critical point while the TO phonon cross section decreases much more slowly.

As in the case of the allowed TO phonon scattering the results are shown in the limit of zero damping. The width of the resonance is then determined by the phonon energy.

In addition to the above discussed "intrinsic" intraband Frohlich mechanism, a number of authors have proposed a variety of extrinsic mechanisms that can activate the forbidden LO phonon scattering. For example, Pinzcuk and Bernstein[7] have shown that surface electric fields produced by depletion layers in semiconductors can result in forbidden LO phonon scattering. Several workers have suggested that defects may be involved in forbidden LO phonon scattering. The basis for this idea is that defects relax momentum conservation and allow phonons of larger $\vec{q}$ to participate. This can lead to an enhancement of the forbidden LO phonon scattering relative to the "intrinsic" process for two reasons. The first is that the $\vec{q}$-dependent Frohlich interaction increases in strength as $\vec{q}$ increases for $|\vec{q}|a_0 < 2$.[16] Thus a process that allows phonons with larger $\vec{q}$ to participate is favored. The second is that the relaxation of momentum conservation leads to a strong double resonance effect, which results in stronger scattering near the outgoing resonance.

Gogolin and Rashba[9] proposed a mechanism for the relaxation of

momentum conservation in LO phonon scattering that involves an elastic scattering between free excitons and defects. Thus the Raman process is of fourth order. The Raman process they proposed can be represented by a Feynman diagram like the one shown in figure 2.2d, except for the fact that Gogolin and Rashba assumed the intermediate states to be discrete exciton states. The model of Gogolin and Rashba is not appropriate for GaAs because the exciton binding energy is very small so it is necessary to consider not only the discrete bound states but also the continuum of the exciton as intermediate states.

Recently Menendez and Cardona[6] (MC) have developed a modification of the theory of Gogolin and Rashba. Instead of an isolated excitonic intermediate state they consider a continuum of uncorrelated electron-hole pairs as intermediate states. In this case the appropriate Feynman diagram is exactly the one shown in figure 2.2d, with the electron-phonon interaction assumed to be a Frohlich interaction. Due to a strong double resonance effect their model predicts that the enhancement in the forbidden LO phonon Raman cross section should peak at the outgoing resonance. This agrees with their experimental data at the $E_0 + \Delta_0$ gap of GaAs. The details of their calculation are discussed in the following section on defect induced Raman scattering.

3.3 Theory of Resonance Behavior of Defect Related Raman Scattering

3.3a Fourth Order Process Involving Plane Wave Phonons

In deriving their results MC draw on the result of an earlier

theory for allowed two phonon scattering due to Zeyher.[10] The Feynman diagram for two phonon scattering is shown in figure 3.5. Comparison with the fourth order process shown in figure 2.2d shows that formally these processes are quite similar; the diagram in figure 2.2d is obtained from the diagram in figure 3.5 by replacing an electron-phonon vertex with an electron-defect vertex.

Zeyher's theory for the two (optical) phonon scattering utilizes a Green function approach. The underlying assumptions are:

- Only 2 band processes are considered.
- Parabolic bands are assumed.
- The excited states are assumed to be free electron-hole pairs.
- Two types of electron-phonon couplings are considered: 1) $\vec{q}$-dependent intraband Frohlich coupling (for the LO phonon). 2) deformation potential coupling for both the TO and LO phonons.
- The phonons are assumed to be dispersionless.

Zeyher finds that the cross sections for the two TO phonon and the two LO phonon scattering are

$$\left.\frac{d\sigma}{d\Omega}\right|_{2TO} \propto \int_0^{x_{BZ}} dx\, x^2 \left|A(s_h x,-s_h x,x_1,x_2,x_3)\right|^2$$

$$\left.\frac{d\sigma}{d\Omega}\right|_{2LO} \propto \int_0^{x_{BZ}} \frac{dx}{x^2} \left|A(s_e x,-s_e x,x_1,x_2,x_3) + A(s_h x,-s_h x,x_1,x_2,x_3) - A(s_e x,s_h x,x_1,x_2,x_3) - A(s_h x,s_e x,x_1,x_2,x_3)\right|^2 \qquad (3.3.1)$$

where the symbols used in equation 3.3.1 are defined as follows:

$$x \equiv aq;\ x_j \equiv ak_j;\ a \equiv \sqrt{\frac{\hbar^2}{2\mu\hbar\omega_p}}\ ;$$

$\vec{q} \equiv$ phonon wave vector; $q \equiv$ amplitude of phonon wave vector;

$$s_{e,h} \equiv m_{e,h}/(m_e+m_h);\ M \equiv m_e + m_h;$$

$$k_j \equiv \left(\frac{2\mu}{\hbar^2}\left(\hbar\omega_i + i\Gamma - \hbar\omega_0 - (j-1)\hbar\omega_p - \delta_{j2}\hbar^2q^2/(2M)\right)\right)^{1/2};$$

$$A(0,\ \lambda_2\vec{q},\ k_1,\ k_2\ \ k_3) \equiv \frac{16\pi^2}{(k_1^2-k_2^2)\lambda_2|\vec{q}|}\left[\tan^{-1}\left(\frac{i\lambda_2 q}{k_1+k_3}\right) - \tan^{-1}\left(\frac{i\lambda_2 q}{k_2+k_3}\right)\right];$$

$$A(\lambda_1\vec{q},\ \lambda_2\vec{q},\ k_1,\ k_2,\ k_3) \equiv \frac{\lambda_1}{\lambda_1+\lambda_2}\,A(0,\ \lambda_1\vec{q},\ S^{1/2},\ k_2,\ k_1)$$

$$+\ \frac{\lambda_2}{\lambda_1+\lambda_2}\,A(0,\ \lambda_2\vec{q},\ S^{1/2},\ k_2,\ k_3);$$

$$S \equiv \frac{\lambda_1 k_3^2 + \lambda_2 k_1^2}{\lambda_1 + \lambda_2} - \lambda_1\lambda_2 q^2\ .$$

MC used Zeyher's result to obtain the Raman cross section of the forbidden LO phonon by simply replacing one of the electron-phonon interaction vertices with an elastic electron or hole scattering vertex. They assume a $\vec{q}$-dependent electron/hole-defect scattering potential V(q) of the form

$$V(q) \propto (q^2 + q_F^2)^{-1} \qquad (3.3.2)$$

where $q_F \equiv 2/\lambda$ and λ is the mean distance between defects. The qualitative features of their results are not very sensitive to the details of the potential chosen and are particularly insensitive to the exact choice of q_F. Additional assumptions they made are: neglect of multiple scatterings of electrons by defects and the validity of the Born approximation. With these assumptions the cross section for the LO phonon calculated from the diagram in figure 2.2d can be shown

to be

$$\sigma_{LO}(\omega_i) \propto \int_0^{q_{BZ}} \left[\frac{dq \left| A_T(\omega_i) \right|^2}{(q^2 + q_F^2)^2} \right] \qquad (3.3.3)$$

$\vec{q}_{BZ}$ is the wave vector at the zone boundary and

$$\begin{aligned} A_T(\omega_i) = {} & A(s_e x, -s_e x, x_1, x_2, x_3) + A(s_h x, -s_h x, x_1, x_2, x_3) \\ & - A(s_e x, s_h x, x_1, x_2, x_3) - A(s_h x, s_e x, x_1, x_2, x_3) \\ & + A(s_e x, -s_e x, x_1, x_2', x_3) + A(s_h x, -s_h x, x_1, x_2', x_3) \\ & - A(s_e x, s_h x, x_1, x_2', x_3) - A(s_h x, s_e x, x_1, x_2', x_3) \end{aligned}$$

where the definitions of the terms are as in 3.3.1 except that now

$$k_3 = \left[\frac{2\mu}{\hbar^2} \right]^{\frac{1}{2}} (\hbar\omega_i + i\eta - \hbar\omega_0 - \hbar\omega_p)^{\frac{1}{2}} ;$$

$$k_2' = \left[\frac{2\mu}{\hbar^2} \right]^{\frac{1}{2}} \left[\hbar\omega_i + i\eta - \hbar\omega_0 - \frac{\hbar^2 (x/a)^2}{2(m_e + m_h)} \right]^{\frac{1}{2}}$$

and where the rest of the notation is the same as in equation 3.3.1.

Plots of the RRS lineshape predicted by equation 3.3.3 for various values of $\vec{q}$ can be found in figure 3.6b. A discussion of these plots will be presented later in section 3.5b when they are compared with experimental results.

The theory of MC can readily be adapted to develop a theory for DAFORS in which the phonons are plane waves and momentum conservation is relaxed due to the electron/hole-defect elastic scattering. The only changes are that the electron-phonon interaction is now assumed to be $\vec{q}$-independent and the phonon branch involved is no longer assumed to be dispersionless.

Since the various phonons that constitute a given branch

represent distinct final states, it is appropriate to integrate over the final distribution of states <u>after</u> squaring the matrix elements. The expression for the RRS lineshape is then

$$\sigma_j(\omega_i, \omega_s) \propto \int_0^{q_{BZ}} dq\ q^2 |A_T(q, \omega_i)|^2\ \delta(\omega_i - \omega_s - \omega_j(q)) \qquad (3.3.4)$$

where $\omega_j(\vec{q})$ is the frequency of the j^{th} phonon branch.

3.3b Fourth Order Process Involving Non-Plane Wave Phonons

A fourth order Raman process can also involve various types of non-plane wave phonons such as local modes or resonant modes. Let us first consider the case in which a local mode is involved. Then each phonon has a broad distribution of $\vec{q}$ components which can be described by a function $C(\vec{q})$ (see equation 2.2.6 in the limit L -> 0). The various $\vec{q}$ components of this local mode do not represent distinct final states. Therefore it is appropriate to carry out the integration over $\vec{q}$ <u>before</u> squaring the matrix elements. The expression for the RRS lineshape is then

$$\sigma(\omega_i, \omega_s) \propto \left| \int_0^{q_{BZ}} dq\ q^2 C(q) A_T(\omega_i)\ \delta(\omega_i - \omega_s - \omega_p) \right|^2 \qquad (3.3.5)$$

It is instructive to examine the magnitude of the contributions made by the different $\vec{q}$ components in the integrand of equation 3.3.5. (This is plotted in figure 3.6a using parameters appropriate for GaAs.) It is seen that the magnitude of the contribution from a small range of $\vec{q}$ values centered about $|\vec{q}| = 0.1/a_0$, where a_0 is the lattice constant, is much greater than the contribution from any of the other

$\vec{q}$ components (note log scale). These special $\vec{q}$ values correspond to scattering wave vectors that allow the double resonance condition to be satisfied. Since a small region in $\vec{q}$ space contributes dominantly to the cross section interference effects should not be important and the theoretical results are relatively insensitive to whether one sums and then squares the different $\vec{q}$ components as in equation 3.3.5 or squares and then sums as in equation 3.3.4. In figure 3.6b the lineshapes of the different $\vec{q}$ components are compared by normalizing their peak amplitudes. Note that the contributions from the special $\vec{q}$ values are markedly asymmetric (peaked at the outgoing resonance) and die off rapidly away from the critical point. Away from these special $\vec{q}$ values the resonances are broader and peaked symmetrically midway between the ingoing and the outgoing resonances.

Non-plane wave phonons other than local modes may also participate in the type of fourth order Raman process illustrated in figure 2.2d. Spatially confined phonons or resonant phonons correspond to a case that is intermediate between the case of plane wave phonons, which lead to equation 3.3.4, and the case of a strictly local mode, which lead to equation 3.3.5. For example, consider the case of a spatially confined phonon derived from a zone edge bulk mode. Though each distinct mode is composed of a distribution of $\vec{q}$ components there still may be a large number of distinct modes in a narrow energy range. As discussed above, there is no significant difference between the lineshapes given by equations 3.3.4 and 3.3.5 so it is not important to know a priori the nature of the phonon in order to predict the enhancement of its Raman cross section.

3.3c Third Order Process Involving Non-Plane Wave Phonons (SC)

The spatially confined phonon (SC) model, which was discussed in section 2.2b, is based on the assumption that the defect related Raman scattering is due to a third order process involving a non-plane wave phonon. Equation 2.2.11 states that the scattering rate is proportional to the square of the scattering matrix element for a near zone center phonon of the same branch. It follows that, except for the differences in the electron-phonon interaction matrix elements, the expression for $\sigma(\omega_i)$ is similar to that of the bulk TO phonon (equation 3.2.6). This is due to the fact that as long as the electronic states responsible for the enhancement are assumed to be the same in the two cases, perturbation theory will produce the same frequency dependence in $\sigma(\omega_i)$.

As shown in the case of the forbidden LO phonon scattering, a $\vec{q}$-dependent electron-phonon interaction can alter the RRS lineshape. For the LO phonon the Frohlich interaction is caused by the macroscopic electric field associated with the LO phonon. Similarly, in a polar semiconductor like GaAs, long wavelength acoustic phonons can produce macroscopic electric fields via the piezoelectric effect. Coupling resulting from the Coulomb interaction of the electrons or holes with this macroscopic electric field associated with small $\vec{q}$ acoustic phonons is therefore analogous to the Frohlich interaction. From electron mobility measurements it was found that the strength of the piezoelectric electron-acoustic phonon coupling in GaAs is comparable to the deformation potential coupling.[5] In section 2.2b I demonstrated that spatially confined zone edge acoustic phonons possess small $\vec{q}$ Fourier components. Since these long wavelength

acoustic phonons have $\vec{q}$ dependent piezoelectric electron-phonon interactions, one may expect a sharper resonance for these spatially confined phonons just as for the forbidden LO phonon.

3.3d Third Order Process Involving Plane Wave Phonons

The Kawamura, Tsu and Esaki (KTE) model, which was discussed in section 2.2c, is based on the assumption that the defect related Raman scattering is due to a process that is third order and involves an unperturbed phonon and non-plane wave electronic intermediate states. As mentioned in section 2.2c, if the function $g_{\vec{k}_a}(\vec{k})$ does not depend on the index $\vec{k}_a$ (i.e., there are no electronic resonances) then

$$\sigma(\omega_i) \propto \left| \int \frac{d^3\vec{k}_a}{(\omega_a - \omega_i)(\omega_a - \omega_s)} \right|^2 \qquad (3.3.6)$$

Comparison of equation 3.3.6 with equation 3.2.6 shows that in this case the KTE mechanism predicts a resonance lineshape that is identical to the TO phonon. On the other hand it is clear that if electronic resonances exist the RRS lineshape can be different. For example, an electronic resonance due to a particular deep level may lead to a sharpening of the RRS lineshape. The reason is because in general the RRS lineshape will be sharper near an isolated intermediate state than near a critical point where it is necessary to perform an integral over a range of intermediate states when calculating the Raman cross section. In particular, $\sigma(\omega_i) \propto 1/(\omega_i - \omega_0)^2$ for an isolated intermediate state (equation 3.2.1a) while for a continuum of intermediate states near an energy gap such as E_0, $\sigma(\omega_i)$

$\alpha \propto 1/(\omega_i - \omega_0)^5$. Thus if the dominant electronic state for the defect related scattering is a narrow electronic resonance rather than an entire band of states, then the resulting RRS lineshape will be sharpened.

3.4 Experimental Aspects

The experimental set-up is the same as the one described in chapter 2.

The measured Raman intensity $I(\omega_i, \omega_s)$ is related to the actual cross section $\sigma(\omega_i, \omega_s)$, assuming that the sample thickness is much greater than the absorption length, by

$$\sigma(\omega_i, \omega_s) \propto \frac{I(\omega_i, \omega_s)(\alpha(\omega_i) + \alpha(\omega_s))}{(1 - R(\omega_i))(1 - R(\omega_s))} \qquad (3.4.1)$$

where $\alpha(\omega_i)$ and $\alpha(\omega_s)$ are the absorption coefficients of the incident and scattered photons respectively, and $R(\omega_i)$ and $R(\omega_s)$ are the reflectivities. Thus in order to deduce the Raman cross sections from these spectra it is necessary to know both the absorption and the reflectivity of the sample.

The reflectivity was measured using a lamp and spectrometer. It was found to vary by only 10% over the range of photon energies investigated. Therefore, correcting for variations in the reflectivity does not appreciably alter the RRS lineshape. On the other hand the absorption coefficient α can vary by more than two orders of magnitude in the vicinity of the E_0 gap so it is necessary to carefully measure

the absorption in this range. The above band gap absorption coefficient is quite large ($\alpha > 10^4$ cm^{-1}). Therefore, in order to make absorption measurements it was necessary to polish samples down to thicknesses ranging from 55 to 10 μm. The sample thicknesses were measured optically with a microscope to an accuracy of only 10-20% for the thinnest sample. However for the purposes of correcting the RRS lineshape only the shape of $\sigma(\omega_i)$ is important and this shape is not affected by inaccuracies in the measurement of the thickness. These thin specimens were prepared using conventional mechanical polishing techniques followed by chemical-mechanical polishing using a bromine/methanol solution. In the case of the electron irradiated sample, where the sample had not received a uniform exposure from the electron beam, care was taken to insure that the absorption was measured at the same location as that used for recording the Raman spectra.

Since the large variation in absorption coefficient in the vicinity of the band gap causes a large uncertainty in the Raman cross section it is often convenient to consider the ratio of the intensities of two Raman peaks $I(\omega_i, \omega_1)/I(\omega_i, \omega_2)$. The corresponding cross section ratio is then related by

$$\frac{\sigma(\omega_i, \omega_2)}{\sigma(\omega_i, \omega_1)} = \frac{I(\omega_i, \omega_1)}{I(\omega_i, \omega_2)} \left(\frac{\alpha(\omega_i) + \alpha(\omega_2)}{\alpha(\omega_i) + \alpha(\omega_1)}\right)\left(\frac{1 - R(\omega_1)}{1 - R(\omega_2)}\right) \quad (3.4.2)$$

Assuming that the absorption is a monotonically increasing function of the photon energy it follows that the absorption correction will at most alter the ratio by a factor of 2.

3.5 Results and Discussion

3.5a Resonance Behavior of the Allowed TO Phonon Scattering

Figure 3.7a shows RRS results for the allowed TO phonon scattering in the electron irradiated sample. The results were obtained in a backscattering geometry from a (110) surface with incident and scattered light both parallel to the (001) direction. The open circles in figure 3.7a represent the integrated intensity of the TO phonon peak as a function of incident photon energy. The data has been corrected for only the incident laser intensity and the response of the detection system, but not for the variation in the sample absorption.

As mentioned in section 3.4, the observed lineshape $I_{TO}(\omega_i)$ is dominated by the large changes in the scattering volume due to the rapidly varying penetration depth. The absorption spectra used to correct these data are shown in figures 3.8 (a) and (b). Also shown for comparison are absorption spectra recorded in an unirradiated sample and a neutron irradiated sample. Note that the electron irradiated sample still exhibits a clear exciton peak but that the absorption edge is shifted down in energy by 20 cm^{-1} relative to the unirradiated sample (figure 3.8a). This small shift may be due to local strains introduced by the irradiation. In the energy range at and above the absorption edge these spectra look very similar to those that have been observed previously.[12] At energies further below the band gap the irradiated samples show increased absorption (figure 3.8b). This can be attributed to the presence of defect induced band tail states. The neutron irradiated sample shows far greater defect

induced sub-band gap absorption than the electron irradiated sample.[11]

The solid circles in figure 3.7a represent the TO phonon cross section after corrections for the absorption and reflectivity of the sample and the ω^4 dependence of the cross section have been made. Figure 3.7b shows a fit of equation 3.2.9 to the corrected TO phonon cross section in the electron irradiated sample. There are three adjustable parameters used in obtaining this fit:

1) Peak height- Since I have not attempted to measure absolute values for the Raman cross section the peak height must be treated as an adjustable parameter.

2) Damping- The theoretical lineshape is quite insensitive to the damping parameter provided that the damping parameter is small relative to the phonon energy. It is found that the best fit to the data is achieved in the limit of zero damping. Even in this limit however the experimental peak is 40% narrower than the theoretical lineshape. This may be explained by the fact that the theory neglects exciton effects, which tend to sharpen resonances. Indeed, previous workers[4] have found that models that include exciton effects provide for a better fit to the experimental data. (There exist theories such as those of Trommer and Cardona[4], Shah, Leite and Damen[13] and Ferrari and Luzzi[14] that take exciton effects into account. However, all of the theories that I am aware of also assume that $\omega_p = 0$. Thus these theories are not accurate in the immediate vicinity of the enhancement peak.)

3) Gap energy- The fit gives a value for the band gap of 12120 ± 40 cm^{-1}, whereas a value of 12170 ± 20 cm^{-1} is deduced from the absorption measurements. Again this small discrepancy can be qualitatively accounted for by noting that models that include exciton

effects tend to shift the peak of the resonance downward in energy by an amount on the order of the exciton binding energy, which is 34 cm^{-1} in GaAs. Also, models that include exciton effects predict assymetric lineshapes in which the low energy side rises more sharply than the high energy side. Such assymetry is evident in the experimental result in figure 3.7b.

Thus from a comparison of the experimental data with theory I conclude that a standard model for TO phonon scattering in crystalline GaAs with small damping and without exciton effects gives a moderately good description of the observed resonance lineshape. It appears that a model that includes exciton effects will improve the quality of the fit. This implies that electron irradiation has not drastically altered the electronic properties of the sample. This is consistent with the absorption measurements, which show only a modest alteration of the absorption spectrum compared to the unirradiated sample. The value deduced for the band gap is 12160 ± 40 cm^{-1}.

Finally, I note that it is normally very difficult to measure the resonant enhancement lineshape near E_0 due to the large luminescence. Trommer and Cardona[4] have published data well above and below the E_0 gap but to my knowledge this is the first detailed study of resonant behavior of TO and LO phonon scattering very close to the E_0 gap in GaAs. This is a side benefit of studying irradiated samples in which the luminescence has been quenched.

3.5b Resonance Behavior of the Forbidden LO Phonon Scattering

Figures 3.9 and 3.10 show the enhancement in the LO phonon intensity relative to the TO phonon intensity for the electron and neutron irradiated samples respectively. In both cases the result is a fairly sharp peak. The steepness of this peak on the low energy side implies that the enhancement in the LO phonon cross section must be much stronger than the TO phonon. Indicated in figures 3.9 and 3.10 by arrows are the locations of the peaks of the enhancement lineshapes. For the forbidden LO phonon scattering this peak occurs at 12470 ± 30 cm^{-1} in both figures 3.9 and 3.10. It should be noted that this is one full LO phonon frequency above the gap, which was deduced in section 3.5a to have a value of 12160 ± 40 cm^{-1}. Thus the peak of the RRS lineshape for the forbidden LO phonon scattering occurs at the outgoing resonance.

In the preceding discussion I have concluded from the absorption and RRS of the TO phonon that the GaAs sample is only moderately perturbed by the electron irradiation. It is thus reasonable to apply the MC theory, which involves Bloch electrons scattered elastically from point defects, to interpret the LO phonon RRS results. (Obviously, when the defect density is high enough this model will break down as the band structure becomes severely perturbed.)

A fit of equation 3.3.5 to the experimental data is shown in figure 3.11. The parameters used in this fit are listed in the figure caption. Note that the value used for the gap is the same as was deduced from the TO phonon RRS data and from the absorption measurements. Thus the only adjustable parameters of any significance are the peak amplitude and the damping. The fitted value for the

damping, which is 90 cm^{-1}, seems reasonable. (It turns out to be almost identical to the one used by MC in fitting their results at the $E_0 + \Delta_0$ gap.) The quality of the fit is seen to be quite good. Specifically, the theory explains the occurrence of the peak position at the outgoing resonance and qualitatively reproduces the observed lineshape.

3.5c Resonance Behavior of the Defect Related Raman Scattering

Figures 3.9 and 3.10 also show plots of the cross sections for the defect induced peaks A and C relative to the TO phonon recorded at 100 K for the electron and the neutron irradiated samples respectively. The most striking feature of these data is that, with the exception of peak C in the neutron irradiated sample, all of these peaks exhibit an enhancement that is sharper than that of the TO phonon, although not as sharp as the LO phonon.

A second important result is that the maximum of the resonance enhancement for peak A occurs at the outgoing resonance in both figures 3.9 and 3.10. For peak C the difference between the ingoing resonance and the outgoing resonance is only 80 cm^{-1}. Therefore it is not possible to distinguish whether the maximum in the RRS lineshape occurs at the outgoing resonance or at a point midway between the ingoing and the outgoing resonances.

Figure 3.12a shows a comparison between the RRS results for peak A in the electron irradiated GaAs recorded at 100 K and results recorded at 10 K. The corresponding results for the forbidden LO

phonon are shown in figure 3.12a. In both cases lowering the temperature causes an upward shift of 70 cm^{-1} in the peak. This is roughly the amount that the band gap is expected to change from the known temperature coefficient. The lineshapes of the RRS results do not change much upon lowering the temperature.

In section 3.3 I discussed four different Raman processes that could potentially account for the Raman peaks A and C. I will now compare the expected resonance enhancement behavior for each of these processes with the experimental results to see which, if any, of these processes can account for the data.

Before such a comparison it is important to note that the band structure in the electron irradiated sample is not strongly perturbed by the radiation damage. This is important because once the possibility of large perturbations of the band structure are allowed there appear very many unknown parameters. This adds a tremendous amount of lattitude to the theoretical RRS lineshapes and the significance of any agreement between theory and experiment is greatly diminished. There are at least three pieces of evidence that suggest that such large band structure perturbations are absent. The first is that both the allowed TO phonon scattering and the forbidden LO phonon scattering were accounted for by models that assumed that the band structure is unperturbed. The second is that the enhancement peak A is observed to shift with temperature in the same way as the fundmental gap E_0. This means that the dominant intermediate state responsible for the enhancement cannot be a deep level. Thirdly, the absorption spectrum (at least in the electron irradiated sample) is only slightly different from the absorption spectrum in the unirradiated sample.

With the above assumption the KTE model predicts that the RRS

lineshapes for the defect induced modes should be identical to that of the TO phonon. It is clear from figures 3.9 and 3.10 that the KTE model cannot account for the experimental results perhaps with the exception of peak C in the neutron irradiated sample.

It was shown in section 3.3c that, if a deformation potential electron-phonon interaction is assumed then the SC mechanism (figure2.2b) also predicts that the enhancement lineshape for the defect induced modes is identical to that of the allowed TO phonon scattering. Thus, again with the possible exception of the peak C scattering in the neutron irradiated sample, this mechanism also cannot explain the RRS results.

It was pointed out in section 3.3c that a $\vec{q}$ dependent piezoelectric electron phonon interaction could be appreciable for non-plane wave phonons. In this case the SC mechanism becomes formally similar to the forbidden LO scattering in a perfect crystal discussed in section 3.2c. This theory can account for why the resonance of peaks A and C in the electron irradiated sample are sharper than the TO phonon resonance. However, as happened for the forbidden LO phonon scattering, this third order process cannot explain why the maximum in the enhancement for peak A occurs at the outgoing resonance. Thus, guided by our experience with the forbidden LO phonon scattering, we are led to consider a higher order process.

First, I consider a fourth order process involving plane wave phonons, which was discussed theoretically in section 3.3a. It is easy to see that this process cannot explain the experimental observation. If peaks A and C were due to plane wave phonons associated with the acoustic branch then the phonon dispersion curves in figure 1.4

suggest that these phonons would mostly have wave vectors near the zone edge because of the high density of states there. In this case double resonance would not be possible and the RRS lineshape should look like the curve labelled q_{BZ} in figure 3.6. Thus this mechanism predicts a resonance that is even less pronounced than the allowed TO phonon resonance and does not agree with experimental observation.

Next let us consider the fourth order scattering process involving non-plane wave phonons, which was discussed in section 3.3b. Shown in figures 3.13 (a) and (b) are the predictions of equation 3.3.5 using phonon frequencies appropriate to peaks A and C respectively. It is assumed in both cases that the phonons are well localized in the sense that the function $C(\vec{q})$, which describes the distribution of $\vec{q}$ values for a given mode, is a constant throughout the Brillouin zone. The values used for the gap ω_0 and the damping are the same as those used in fitting the forbidden LO phonon scattering in section 3.5b. Also shown in figures 3.13 (a) and (b) for comparison are the experimental data for peaks A and C. The main point to note is that the theory agrees reasonably well with experiment with no adjustable parameters. In particular, the theory accounts qualitatively for the fact that the enhancement in the defect related modes is sharper than that of the TO phonon and peaked at the outgoing resonance. Comparison of the theoretical curves and the experimental data points for the enhancement of the Raman cross section of the defect induced modes in figure 3.13 with the corresponding results in figure 3.11 for the fourth order forbidden LO phonon scattering, shows that both the theoretically predicted and the experimentally observed enhancements are less strong in the former case. This is a direct consequence of the assumption that the electron-phonon interaction

that occurs during the scattering of the defect induced modes is $\vec{q}$-independent. In contrast, the Frohlich interaction responsible for the forbidden LO phonon scattering is $\vec{q}$-dependent.

As in the case of the forbidden LO phonon scattering I find that a theory based on a higher order process better describes the enhancements of peaks A and C. Since the Frohlich interaction is not involved for these peaks it is not obvious why the fourth order scattering process should be more important than the third order scattering processes. The explanation is that most likely double resonance effects are still important for these peaks.

As mentioned above, a requirement for double resonance to be possible in the current model is that a non-plane wave phonon must be involved. Then strong resonant enhancement will occur for those phonon having large Fourier amplitude $C(\vec{q})$ at those special $\vec{q}$ values that satisfy double resonance. One interesting consequence of this model is that the RRS lineshape is quite sensitive to the degree of localization of the phonon. This can be demonstrated by assuming that the phonon has a Gaussian envelope as was done in section 2.2b and applying equation 3.3.5 to calculate the RRS lineshape. The results are shown in figure 3.14 for localization lengths of 5 and 100 Å. Even though 100 Å corresponds to a reasonably well localized phonon, the RRS lineshape is already quite broad (in fact it is broader than the allowed TO phonon resonance) and is no longer peaked at the outgoing resonance. This results from the fact that in the model of section 2.2b, $C(\vec{q})$ is very sensitive to the localization length L when $qL \geq 1$. Thus, whether double resonance effects are important or not depends critically on L.

The conclusion of the above discussion is that more localized modes give rise to sharper resonances. Examination of the experimental data for the resonance behavior of the defect induced modes (figures 3.9 and 3.10) suggests that peak A is well localized in both the neutron and the electron irradiated samples while peak C is well localized only in the electron irradiated sample. This is consistent with the proposal made in chapter 2 that peak C in the electron irradiated sample involves resonant modes while peak C in the neutron irradiated sample is due to either spatially confined modes or plane wave modes and is not due to isolated defects. The difference between the electron and neutron irradiated samples can be traced to the fact that neutron irradiation produces more damage resulting in a clustering of defects, which tends to spatially confine the phonon modes in the neutron irradiated sample.

Note that even though a resonant mode may extend over many lattice constants in the crystal, such modes are still expected to have an enhanced amplitude at the defect (see figure 1.6b). This enhancement will result in a broad range of Fourier components which enables a strong double resonance to occur and leads to strong sharp resonances. As an illustration of this idea I show in figure 3.15 a simple model for the wave function of a resonance mode and the corresponding theoretical predictions for its RRS lineshape. The wave function of this resonant mode is assumed to be a linear combination of two Gaussians (figure 3.15a):

$$\psi'(r) = \exp\left[\frac{-2r^2}{L_1^2}\right] + \exp\left[\frac{-2r^2}{L_2^2}\right] \qquad (3.5.1)$$

Substituting equation 3.5.1 into equation 2.2.6 gives

$$C(\vec{q}) = L_1 \exp\left[\frac{-q'^2 L_1^2}{4}\right] + L_2 \exp\left[\frac{-q'^2 L_2^2}{4}\right] \qquad (3.5.2)$$

where $\vec{q}' \equiv \vec{q}_{BZ} - \vec{q}$.

In figure 3.15a, L_1 corresponds to the length over which the enhancement of the amplitude of the resonant phonon at the defect decays. L_2 is assumed to be a much longer decay length that corresponds to the spatial extent of the resonant mode. Two cases are shown in figure 3.15a: 1) $L_1 = 5$ Å, $L_2 = 100$ Å and 2) $L_1 = L_2 = 100$ Å. The first case corresponds to a resonant phonon in which there is an enhanced amplitude of vibration at the defect which decays rapidly away from the defect. The second case describes a confined phonon for which there is no enhanced amplitude of vibration at the defect. The corresponding functions $C(\vec{q})$ are shown in figure 3.15b. Figure 3.15c shows the RRS lineshapes predicted by the theory for the fourth order Raman process (equation 3.3.5). The result indicates that even though these two phonons differ from one another only within the first few lattice constants surrounding the point defect, the RRS lineshapes are appreciably different. Thus the RRS lineshape is sensitive to the enhanced motion in the immediate vicinity of the defect.

3.6 Conclusions

Experimentally I have observed that the defect related scattering exhibits a strong resonant enhancement in the vicinity of the E_0 gap with a lineshape that peaks at the outgoing resonance. These results can be explained by a theoretical model that assumes that the dominant Raman process is fourth order and involves elastic scattering of the carriers by defects. Within the framework of this model the observed resonant enhancement behavior allows one to distinguish between modes that have an enhanced amplitude of vibration at the defect that decays over a short distance and those that do not. Those modes that are well localized in this sense are found to exhibit a stronger resonant enhancement. This result has very favorable consequences for the use of Raman scattering as a probe of defects. It implies that one can selectively enhance that scattering involving vibrational modes with an increased motion in the immediate vicinity of the defect. It is exactly this type of mode that may contain important microscopic information concerning the defect.

Another conclusion that can be reached based on this theoretical understanding is that, due to double resonance effects, a mode that shows a strong enhancement at the E_0 critical point should also show a strong enhancement at higher lying critical points. This suggests that even in samples with defect concentrations considerably lower than the ones used in this study, where the band gap luminescence is not quenched, it should still be possible to utilize Raman scattering to probe defects by tuning the laser to resonate with energy transitions such as the $E_0 + \Delta_0$ or E_1 transitions in zincblende semiconductors. Although some signal will be lost due to the shorter

penetration depth this loss will at least partially be offset by the increased efficiency of detectors and the increased power of lasers available in this frequency range.

References

1- E. Bedel, R. Carles, A. Zwick, J. B. Renucci and M. A. Renucci, Phys. Rev. B 30, 5923 (1984).

2- P. Y. Yu, M. H. Pilkuhn and F. Evangelisti, Sol. St. Comm. 25, 371 (1978).

3- D. J. Wolford, B. G. Streetman, S. Lai and M. V. Klein, Sol. St. Comm. 32, 51 (1979).

4- R. Trommer and M. Cardona, Phys. Rev. B 17, 1865 (1978).

5- M. Cardona in Light Scattering in Solids II, p. 19, Springer-Verlag, Berlin, (1982).

6- J. Menendez and M. Cardona, Phys. Rev. B 31, 3696 (1985).

7- A. Pinzcuk and E. Burstein, Phys. Rev. Lett. 21, 1073 (1968).

8- P. Colwell and M. V. Klein, Sol. St. Comm. 8, 2095 (1970).

9- A. A. Gogolin and E. I. Rashba, Sol. St. Comm. 19, 1177 (1976).

10- R. Zeyher, Phys. Rev. B 9, 4439 (1974).

11- The magnitude of the Raman signal was mucn larger in the electron irradiated sample than in the neutron irradiated sample. In addition, electron irradiation produces a more theoretically tractable result than neutron irradiation (i. e. homogeneously distributed isolated defects as opposed to inhomogeneously distributed clusters). For these reasons I shall concentrate on trying to understand quantitatively only the RRS results for the electron irradiated sample. The RRS results for the neutron irradiated sample will be discussed only qualitatively.

12- M. D. Sturge, Phys. Rev. 127, 768 (1962).

13- J. Shah, R. C. Leite and T. C. Damen, Opt. Comm. 1, 267 (1970).

14- C. A. Ferrari and R. Luzzi, Phys. Rev. B 19, 5284 (1979).

15- R. Martin, Phys. Rev. B 10, 2620 (1974); R. Martin, Phys. Rev. B

4, 3676 (1971).

16- P. Y. Yu in Excitons, ed. by K. Cho, Springer-Verlag, Berlin (1978).

Figure Captions

3.1- Demonstration of ingoing (first column) and outgoing resonances (second column) and the occurrence of double resonance. These drawings all depict processes with the Feynman diagram given in figure 2.2a. The numbers indicate the order of the electronic transitions. It is assumed that step (2) also includes the emission of a phonon of energy $\hbar\omega_p$ and wave vector $\vec{q}_p$. The length of the photon arrows denote the photon energy. The third column shows the expected behavior of $\sigma(\omega_i)$ for small damping (solid line) and larger damping (dashed line). a) Isolated intermediate state. b) Scattering in a model band structure. The phonon wave vector $\vec{q}_p$ is assumed to be unusually large. This allows double resonance to occur at the outgoing resonance. c) Scattering in a model band structure with $\vec{q}_p = 0$. No double resonance is possible.

3.2- Schematic drawings of two band (a) and three band (b) Raman processes. Although these drawings portray hole-phonon scattering, analogous drawings exist for electron-phonon scattering. The numbers indicate the order of the electronic transitions.

3.3- $\sigma(\omega_i)$ for TO phonon scattering according to equation 3.2.9 and for forbidden LO phonon scattering according to equation 3.2.15. in GaAs at the E_0 critical point. Both curves are in the limit of zero damping.

3.4- Schematic diagram of the two-band Raman processes involving the q dependent Frohlich interaction used in the heuristic calculation of the forbidden LO phonon Raman scattering. a) Scattering with electrons

emitting the LO phonon. b) Scattering with holes emitting the LO phonon.

3.5- Feynman diagram for a fourth order two- phonon scattering process considered by Zeyher (reference 10). The notation is the same as in figure 2.2.

3.6- Resonance behavior of the Raman cross section according to the MC theory for phonons of different $\vec{q}$. The $\vec{q}$-values given in the figure are in units of $1/a_0$, where a_0 is the lattice constant. $q_{MC} = 0.02$ corresponds to the wave vector determined by momentum conservation for the experimental conditions described in section 3.4. $\vec{q}_{BZ}$ is the zone edge wave vector. a) Here the curves are not normalized so that the magnitude of the contribution from different $\vec{q}$-components can be compared. Note the log scale. b) Here the curves are scaled to have the same peak amplitudes. This facilitates comparison of their lineshapes.

3.7- Resonance behavior of allowed TO phonon scattering at 100 K in electron irradiated GaAs. a) Shows experimental data that is uncorrected except for normalization by the incident laser power (open circles) and data that has been corrected for absorption and other effects listed in the text (closed circles). b) Fit of equation 3.2.9 to the corrected experimental data using $\omega_0 = 12160\ cm^{-1}$ (dashed line) and $\omega_0 = 12120\ cm^{-1}$ (solid line). No damping is included.

3.8- Absorption data for electron irradiated, neutron irradiated and

unirradiated GaAs (a) around the band gap; (b) below the band gap.

3.9- RRS behavior of peak A, peak C and the LO phonon scattering in electron irradiated GaAs at 100 K. These were recorded in a $\Gamma_1 + 4\Gamma_{12}$ scattering geometry. Solid lines are to guide the eyes only.

3.10- RRS behavior of peak A, peak C and LO phonon scattering in the neutron irradiated sample at 100 K. These were recorded in a $\Gamma_1 + 4\Gamma_{12}$ scattering geometry. Solid lines are to guide the eyes only.

3.11- Fit of the MC theory (equation 3.3.4) to the LO phonon RRS results. The parameters used are: $\omega_0 = 12160\ cm^{-1}$ and damping = 90 cm^{-1}.

3.12- Temperature dependence of RRS in the electron irradiated sample a) LO phonon relative to TO phonon intensity at 10 K and 100 K. Note the logarithmic scale for the intensity. b) Peak A relative to TO phonon at 10 K and 100 K. In both a) and b) the data are scaled to the same peak amplitude in order to facilitate a comparison of the lineshapes. The amplitude of both the peak A and the LO phonon resonances (relative to the TO phonon) was roughly 20% greater at low temperature.

3.13- Fit of equation 3.3.5 to the enhancement in (a) peak A (parameters used are $\omega_1 = 12160\ cm^{-1}$, damping = 90 cm^{-1}, $\omega_0 = 227\ cm^{-1}$, ω_p) and (b) peak C (parameters used are $\omega_0 = 12160\ cm^{-1}$, damping = 90 cm^{-1}, $\omega_p = 80\ cm^{-1}$).

3.14 Resonance behavior of a spatially confined phonon mode calculated from equations 3.3.5 and 2.2.6 for L = 5 Å and L = 100 Å.

3.15- Comparison between the enhancement in the Raman cross section of a resonance phonon and a spatially confined phonon. a) Model for the wave functions of the confined and resonance phonons. The confined phonon is assumed to have an envelope given by $\exp(-2r^2/L_2^2)$ while the resonant phonon has an envelope given by $\exp(-2r^2/L_1^2) + \exp(-2r^2/L_2^2)$. Here L_1 = 5 Å and L_2 = 100 Å. b) Corresponding distribution of Fourier components for these two types of phonons. Note the logarithmic vertical scale. c) RRS behavior for these two phonons as predicted by equation 3.3.5.

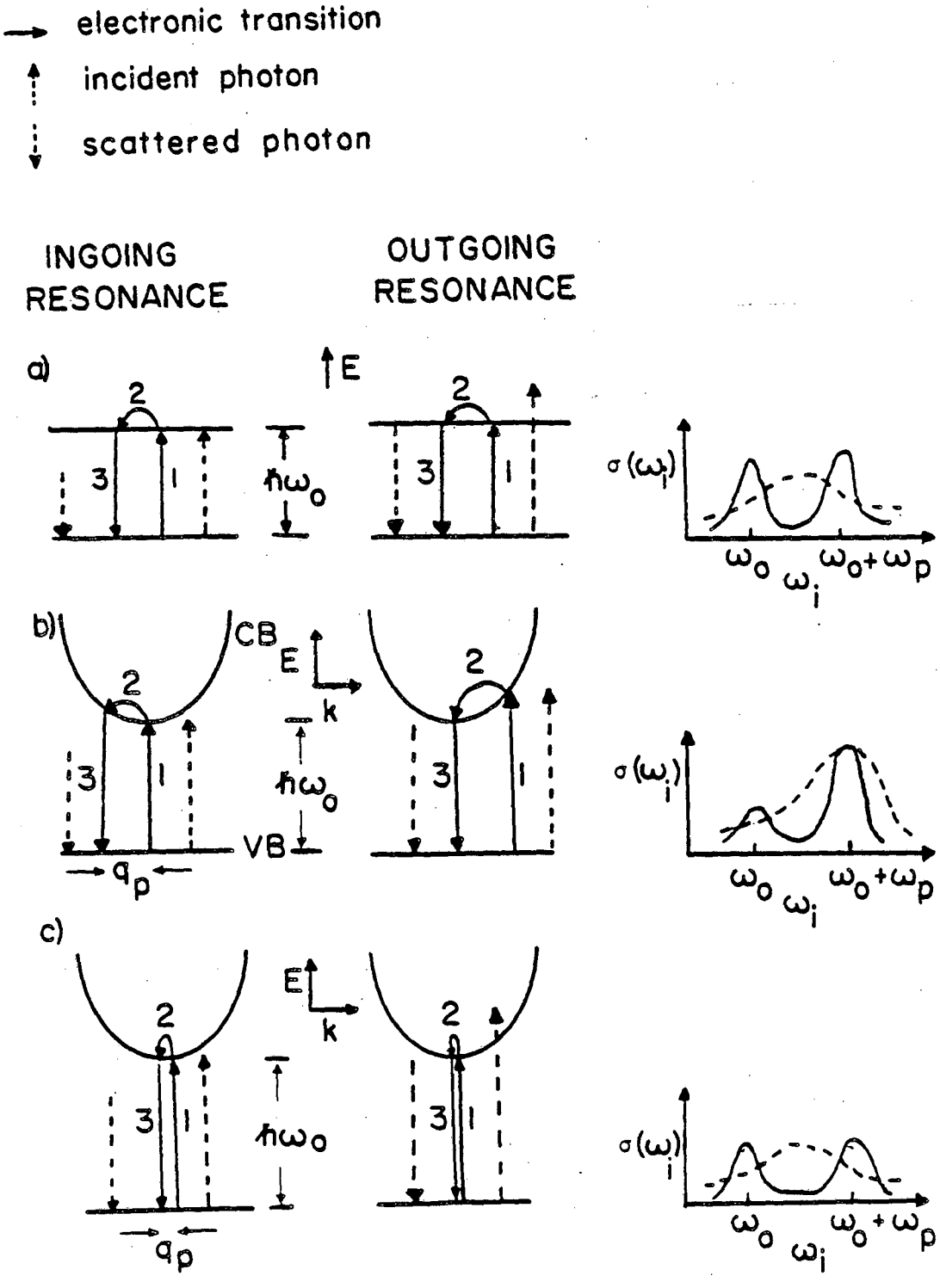
electronic transition
incident photon
scattered photon
INGOING RESONANCE
OUTGOING RESONANCE
a)
E
2
3
1
ħω₀
σ(ωᵢ)
ω₀ ωᵢ ω₀+ωₚ
b)
CB
E
k
VB
qₚ
c)

Figure 3.1

a)

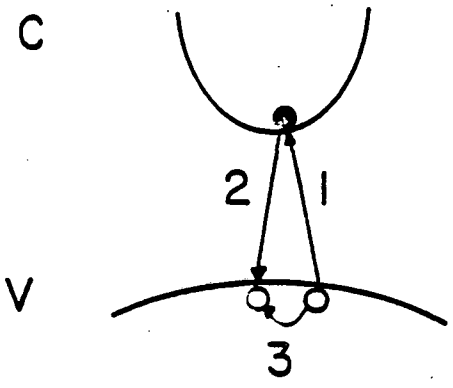

b)

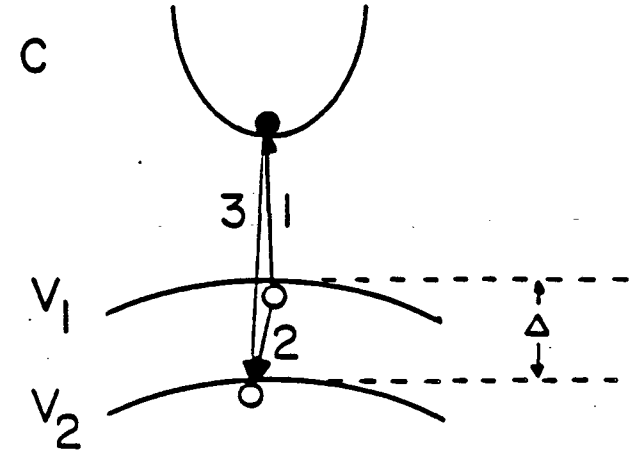

Figure 3.2

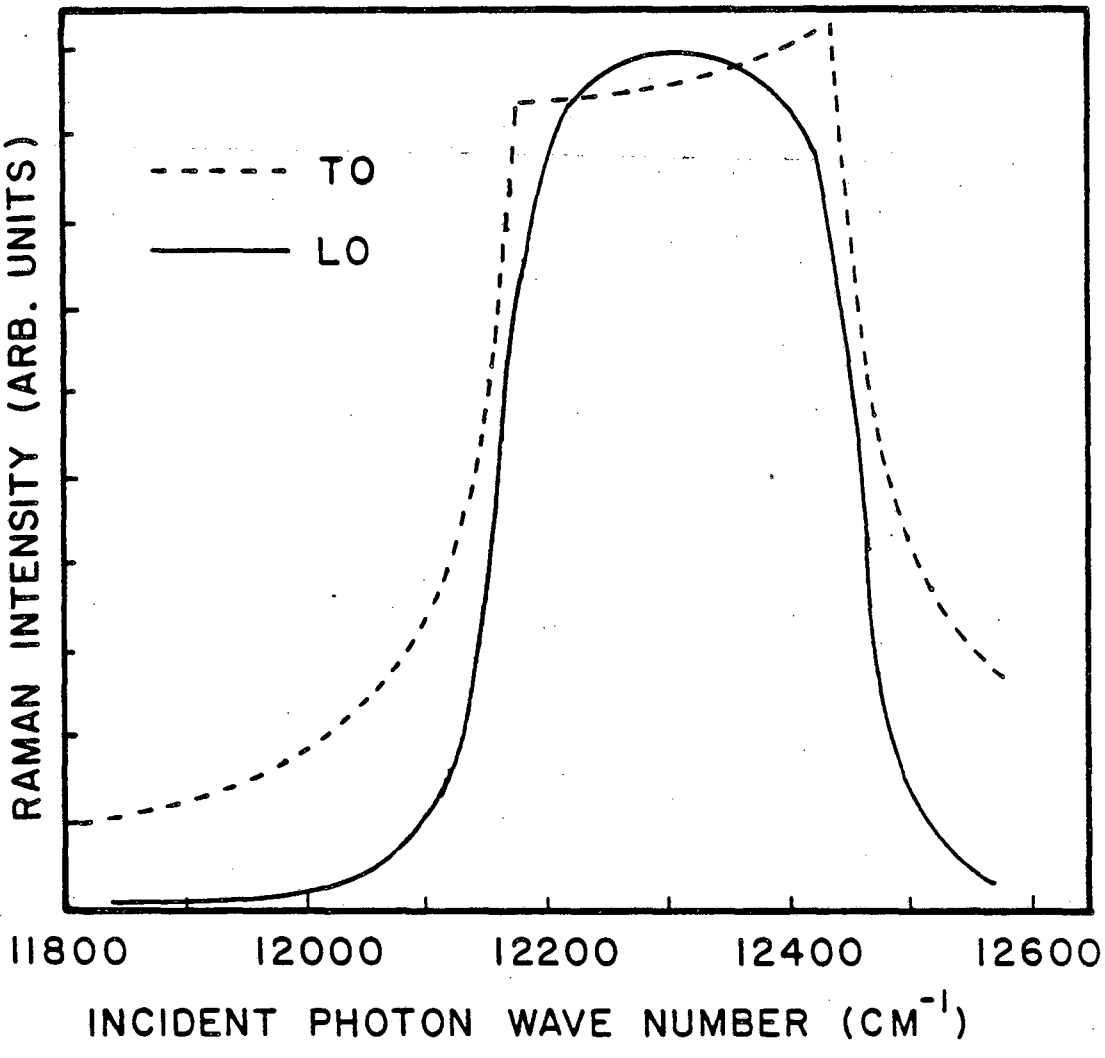
TO
LO
RAMAN INTENSITY (ARB. UNITS)
11800
12000
12200
12400
12600
INCIDENT PHOTON WAVE NUMBER (CM^{-1})

Figure 3.3

a)

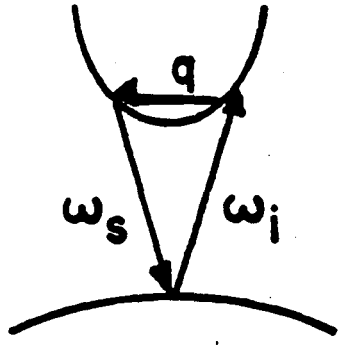

b)

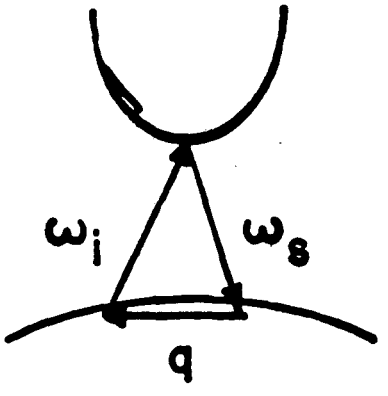

Figure 3.4

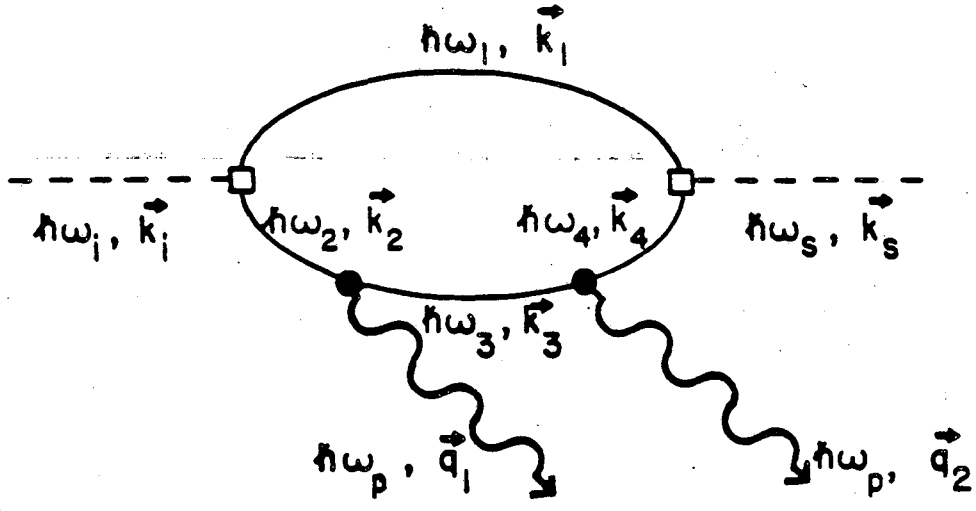
$\hbar\omega_1, \vec{k}_1$
$\hbar\omega_i, \vec{k}_i$
$\hbar\omega_2, \vec{k}_2$
$\hbar\omega_4, \vec{k}_4$
$\hbar\omega_s, \vec{k}_s$
$\hbar\omega_3, \vec{k}_3$
$\hbar\omega_p, \vec{q}_1$
$\hbar\omega_p, \vec{q}_2$

Figure 3.5

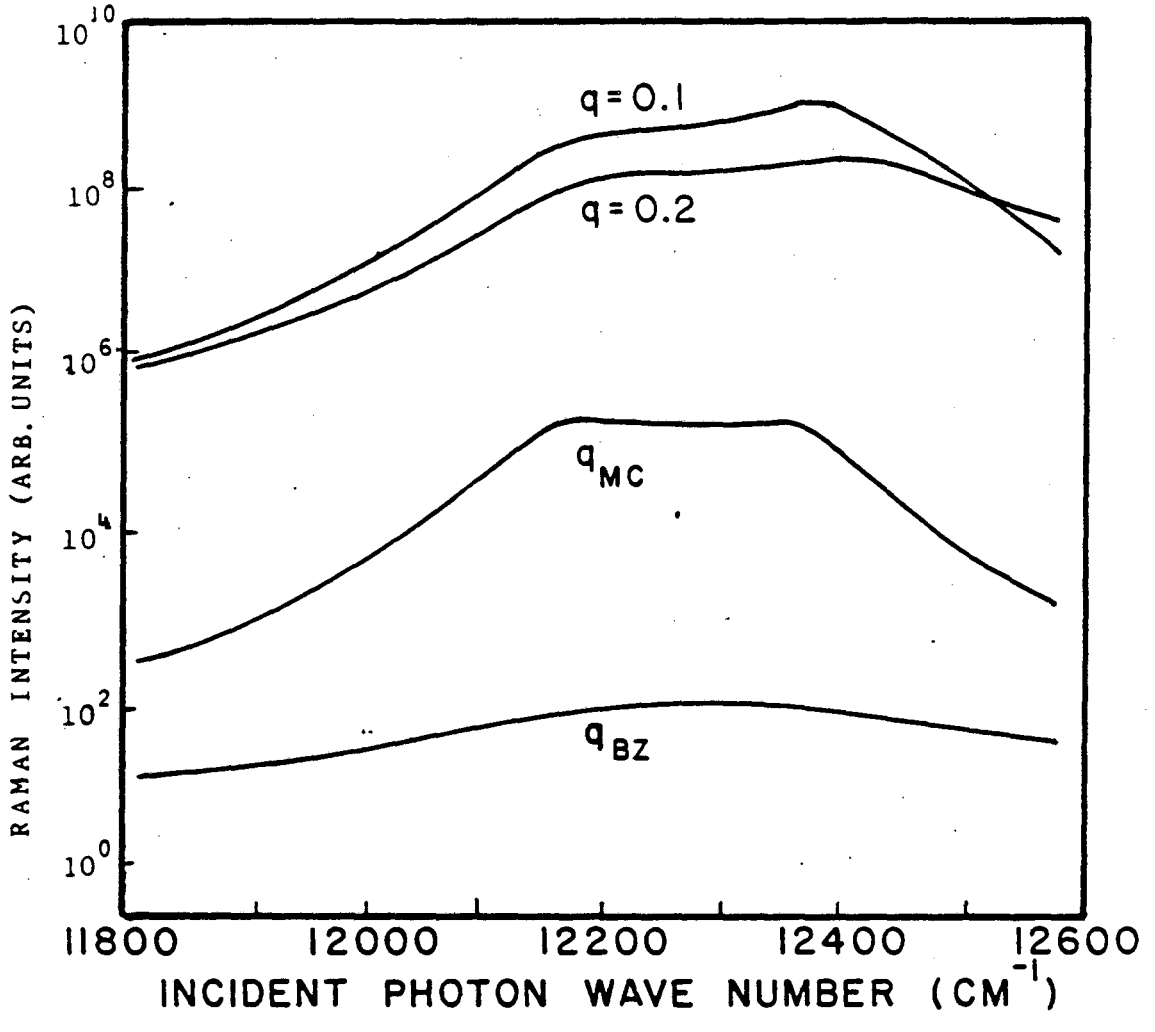
10^{10}
10^{8}
10^{6}
10^{4}
10^{2}
10^{0}
RAMAN INTENSITY (ARB. UNITS)
q = 0.1
q = 0.2
q_{MC}
q_{BZ}
11800
12000
12200
12400
12600
INCIDENT PHOTON WAVE NUMBER (CM^{-1})

Figure 3.6a

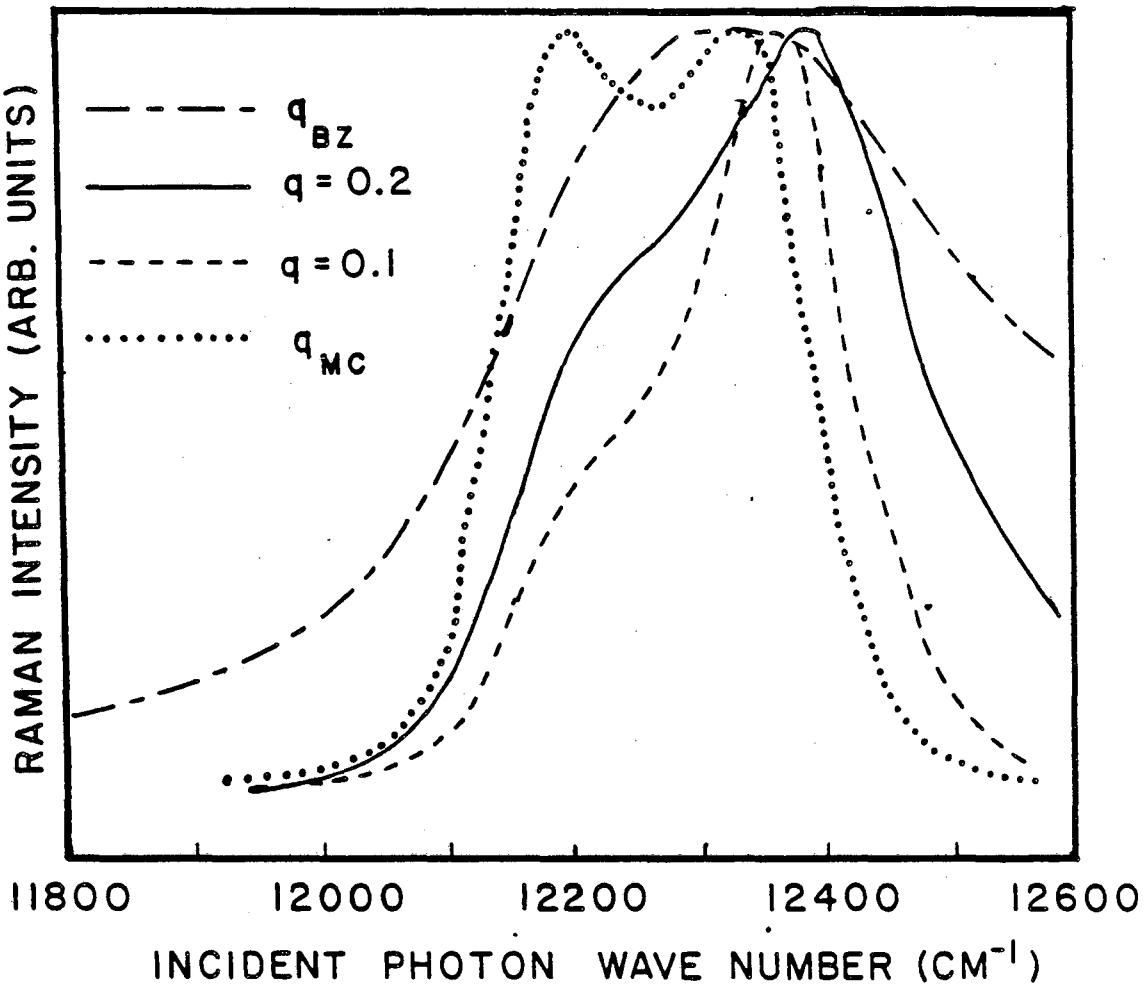
RAMAN INTENSITY (ARB. UNITS)
q_{BZ}
q = 0.2
q = 0.1
q_{MC}
11800
12000
12200
12400
12600
INCIDENT PHOTON WAVE NUMBER (CM^{-1})

Figure 3.6b

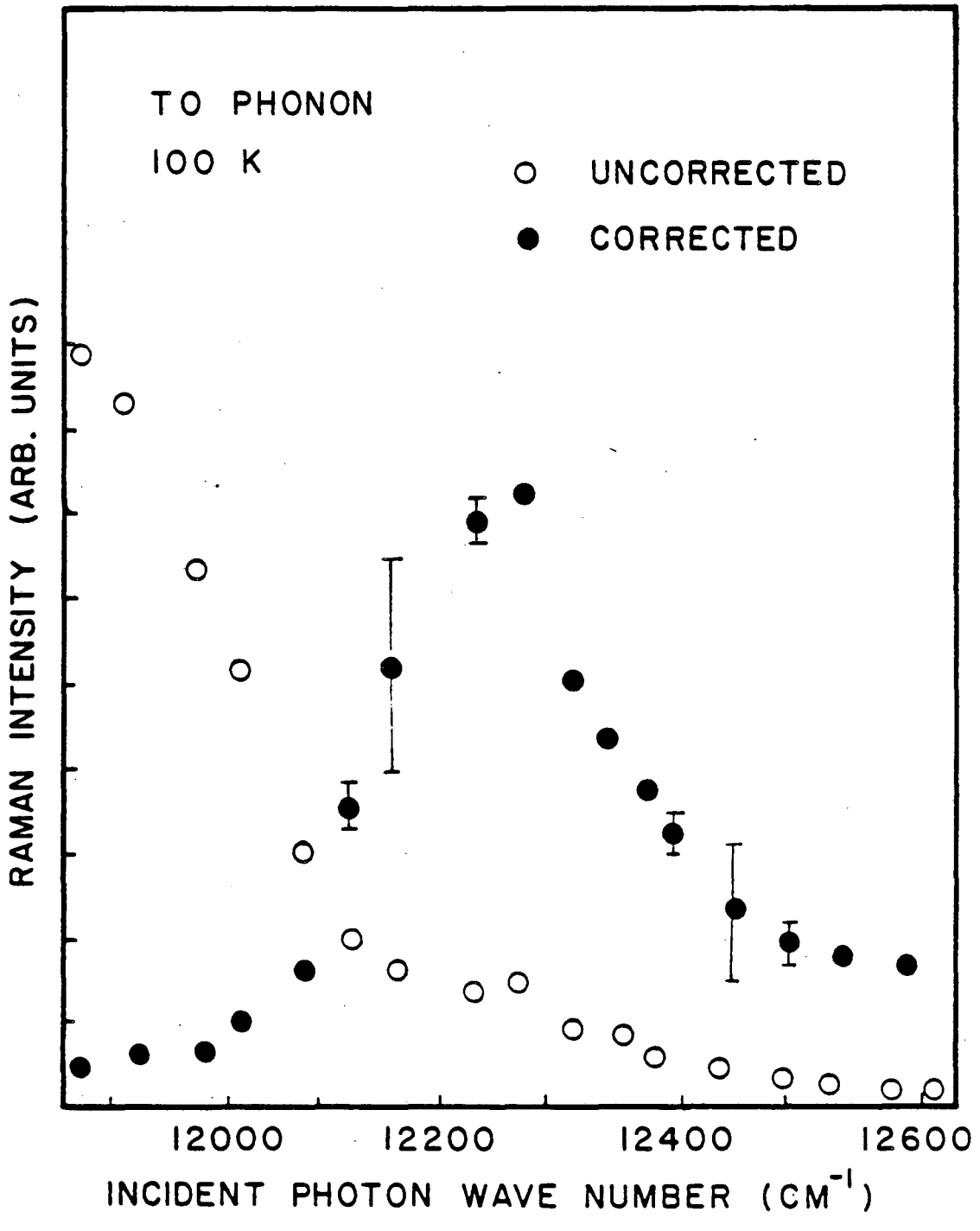
TO PHONON
100 K
UNCORRECTED
CORRECTED
RAMAN INTENSITY (ARB. UNITS)
12000
12200
12400
12600
INCIDENT PHOTON WAVE NUMBER (CM^{-1})

Figute 3.7a

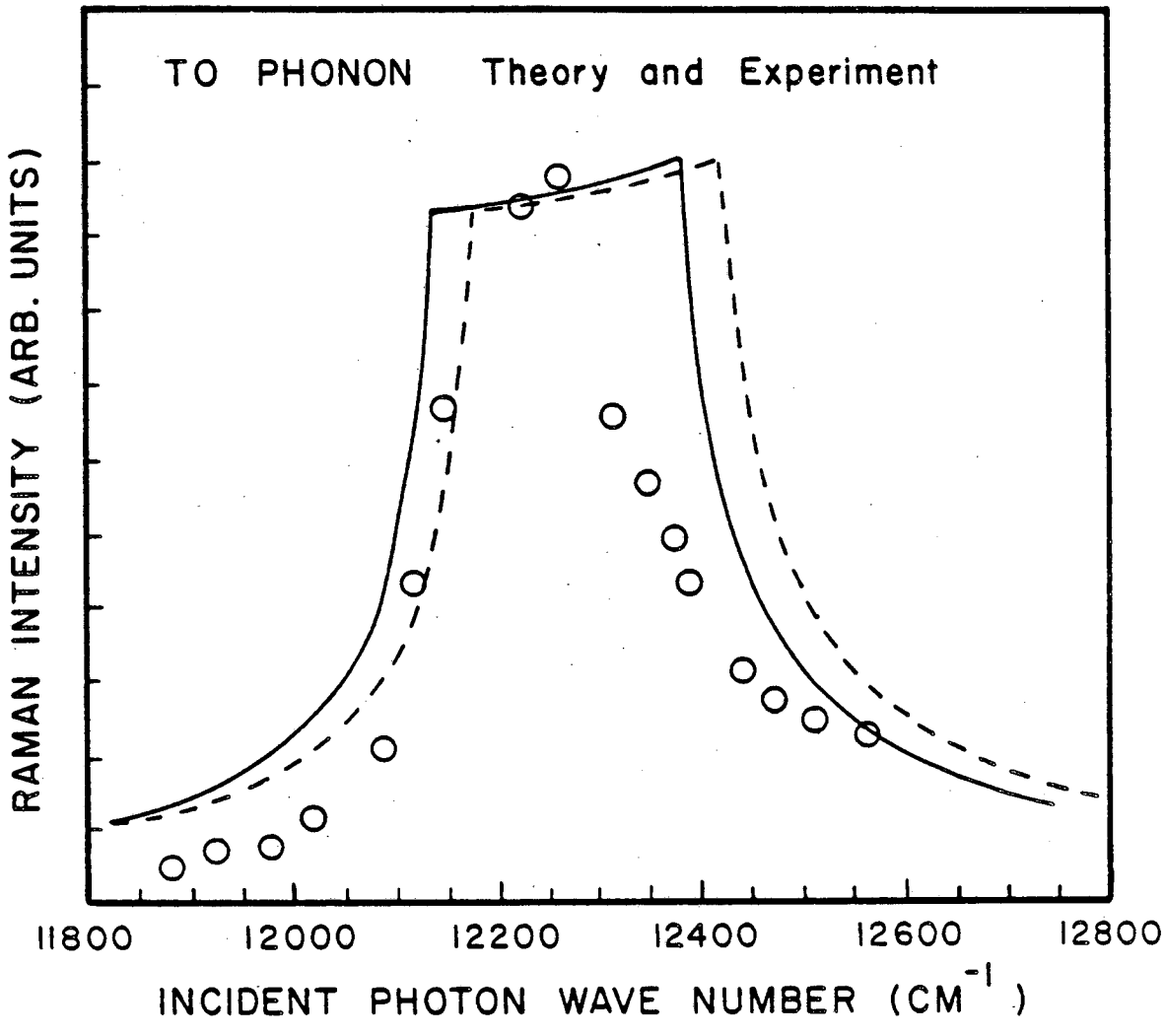
TO PHONON Theory and Experiment
RAMAN INTENSITY (ARB. UNITS)
11800
12000
12200
12400
12600
12800
INCIDENT PHOTON WAVE NUMBER (CM^{-1})

Figure 3.7b

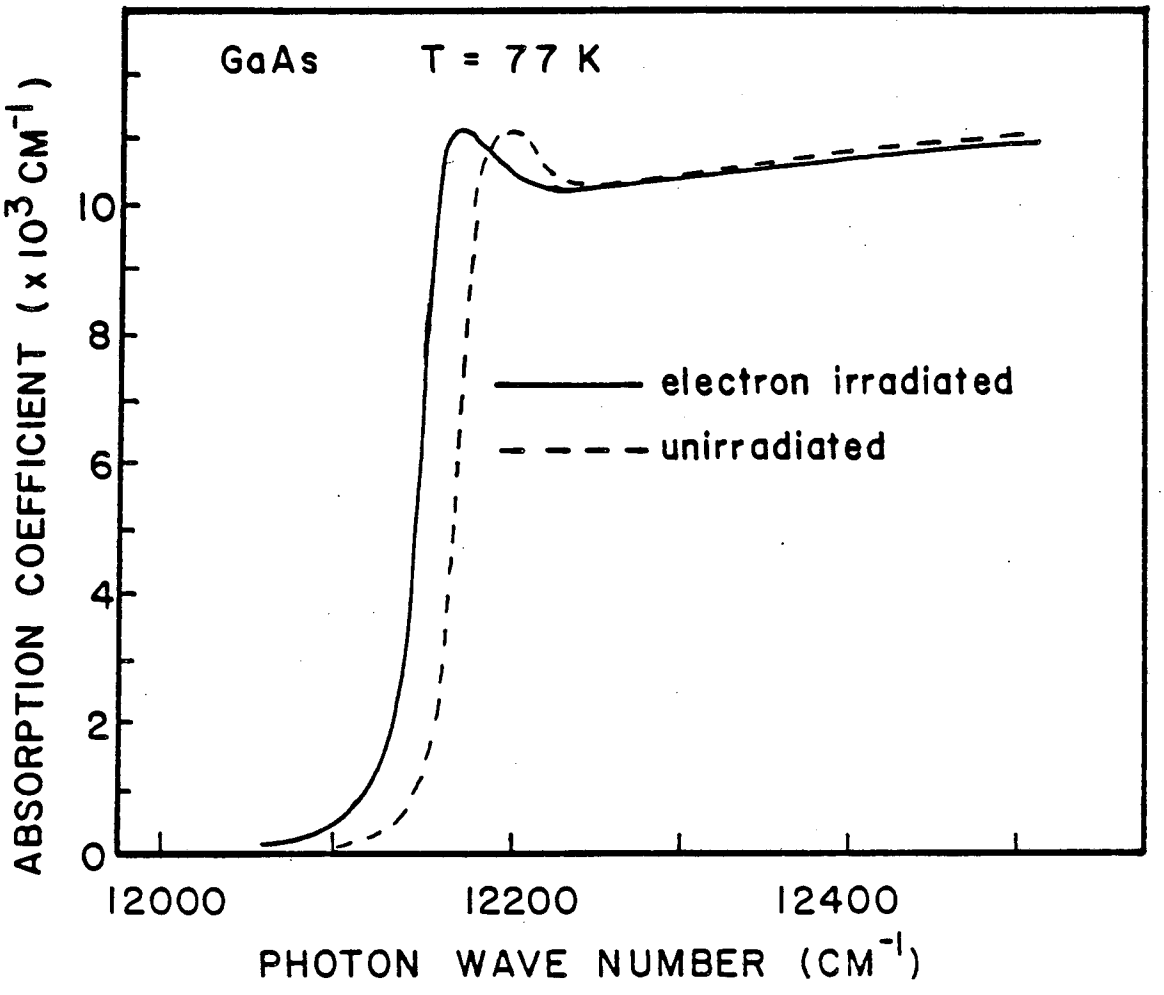
GaAs
T = 77 K
ABSORPTION COEFFICIENT (x 10^3 CM^-1)
0
2
4
6
8
10
12000
12200
12400
PHOTON WAVE NUMBER (CM^-1)
electron irradiated
unirradiated

Figure 3.8a

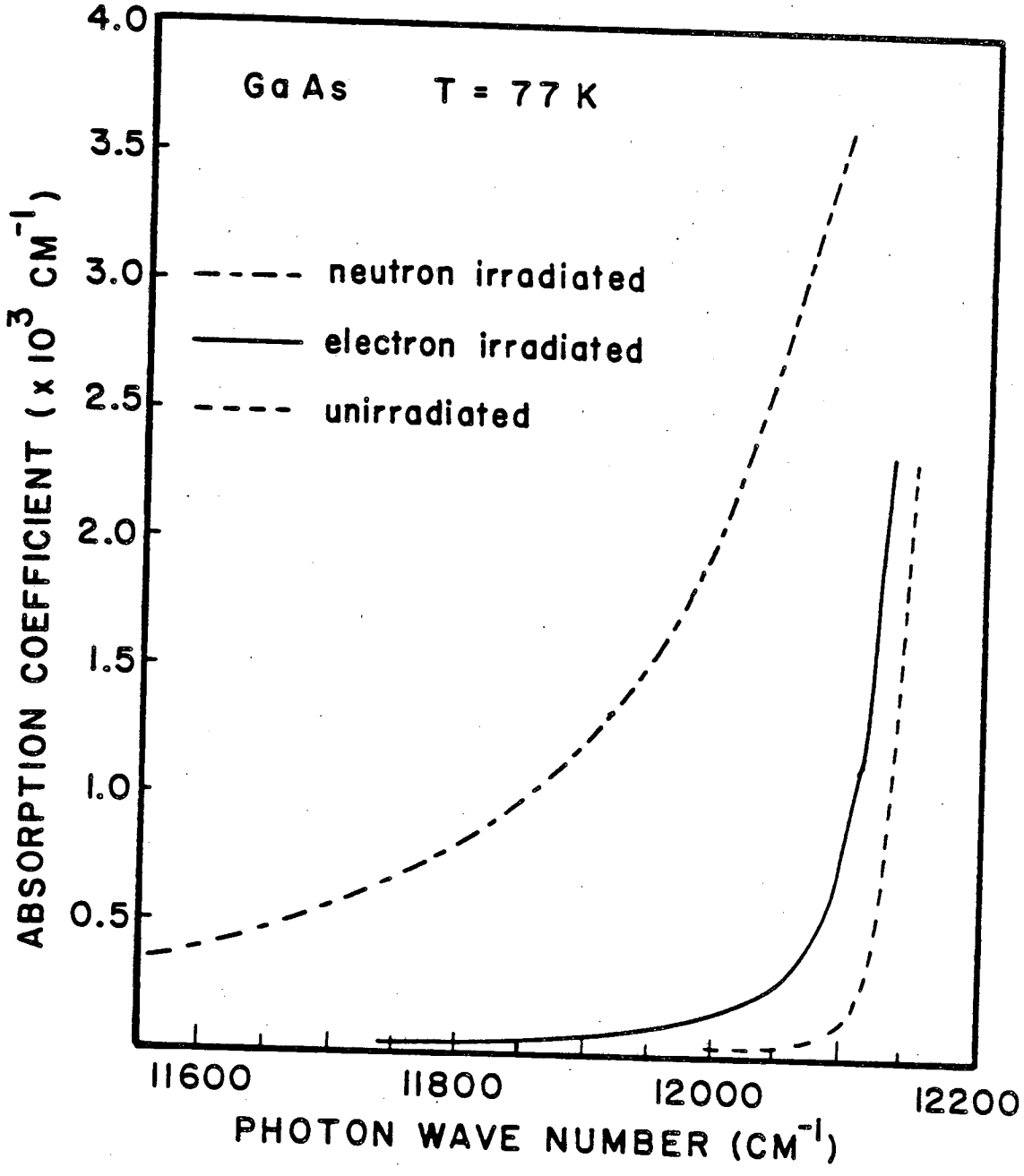
Ga As T = 77 K
neutron irradiated
electron irradiated
unirradiated
ABSORPTION COEFFICIENT (x 10^3 CM^-1)
4.0
3.5
3.0
2.5
2.0
1.5
1.0
0.5
11600
11800
12000
12200
PHOTON WAVE NUMBER (CM^-1)

Figure 3.8b

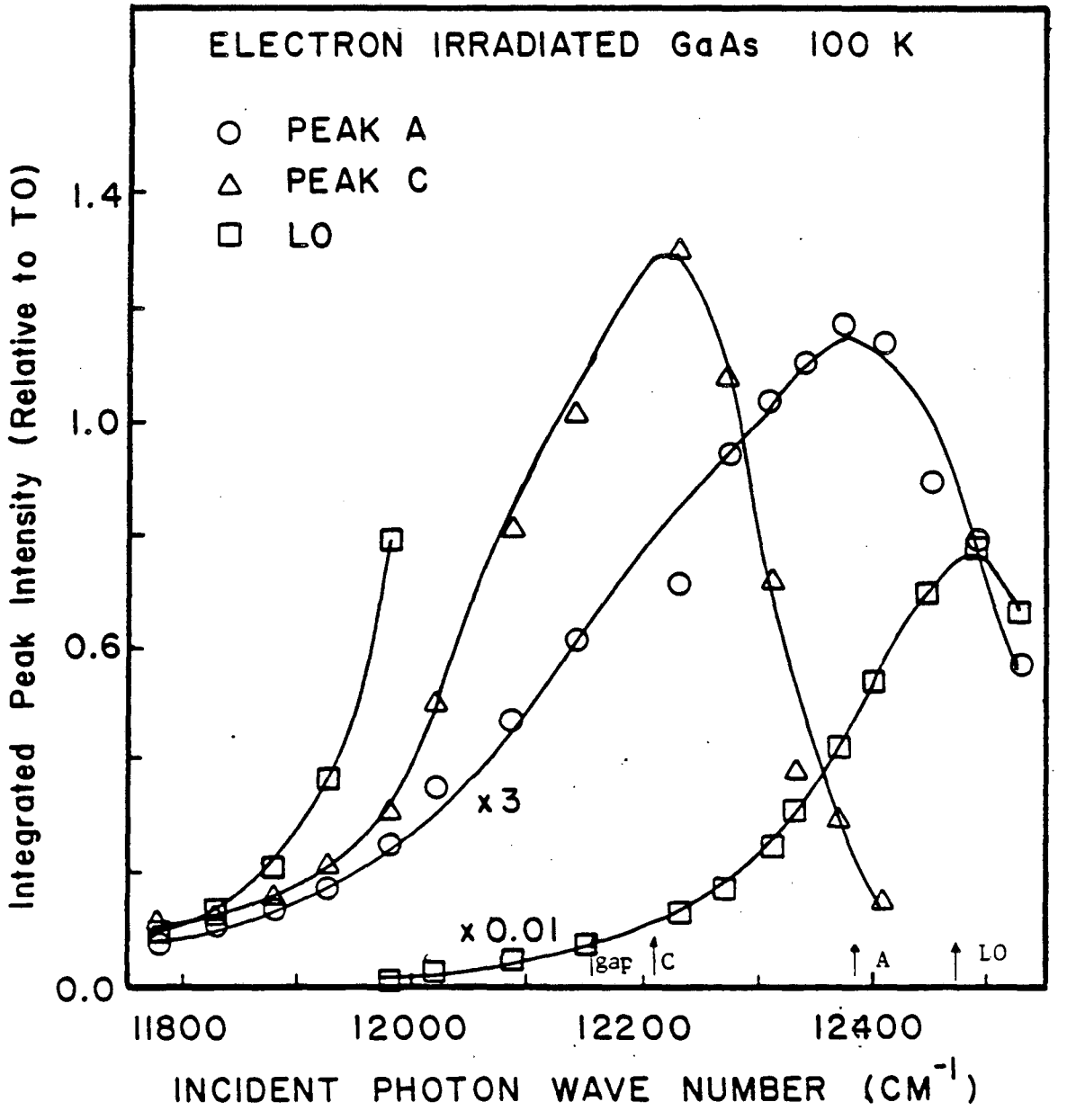
ELECTRON IRRADIATED GaAs 100 K
PEAK A
PEAK C
LO
Integrated Peak Intensity (Relative to TO)
1.4
1.0
0.6
0.0
x3
x 0.01
gap
C
A
LO
11800
12000
12200
12400
INCIDENT PHOTON WAVE NUMBER (CM⁻¹)

Figure 3.9

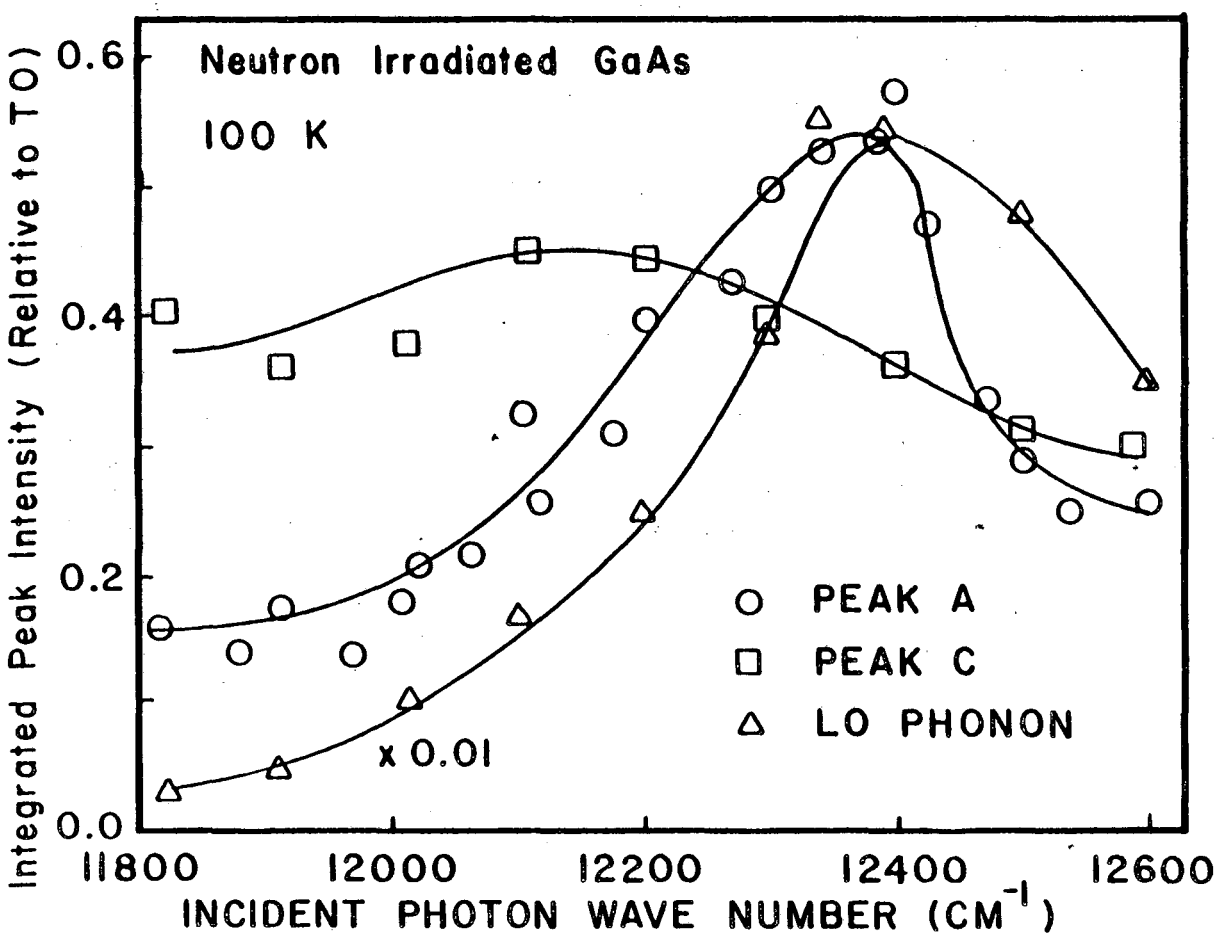
Neutron Irradiated GaAs
100 K
PEAK A
PEAK C
LO PHONON
x 0.01
Integrated Peak Intensity (Relative to TO)
0.0
0.2
0.4
0.6
11800
12000
12200
12400
12600
INCIDENT PHOTON WAVE NUMBER (CM^{-1})

Figure 3.10

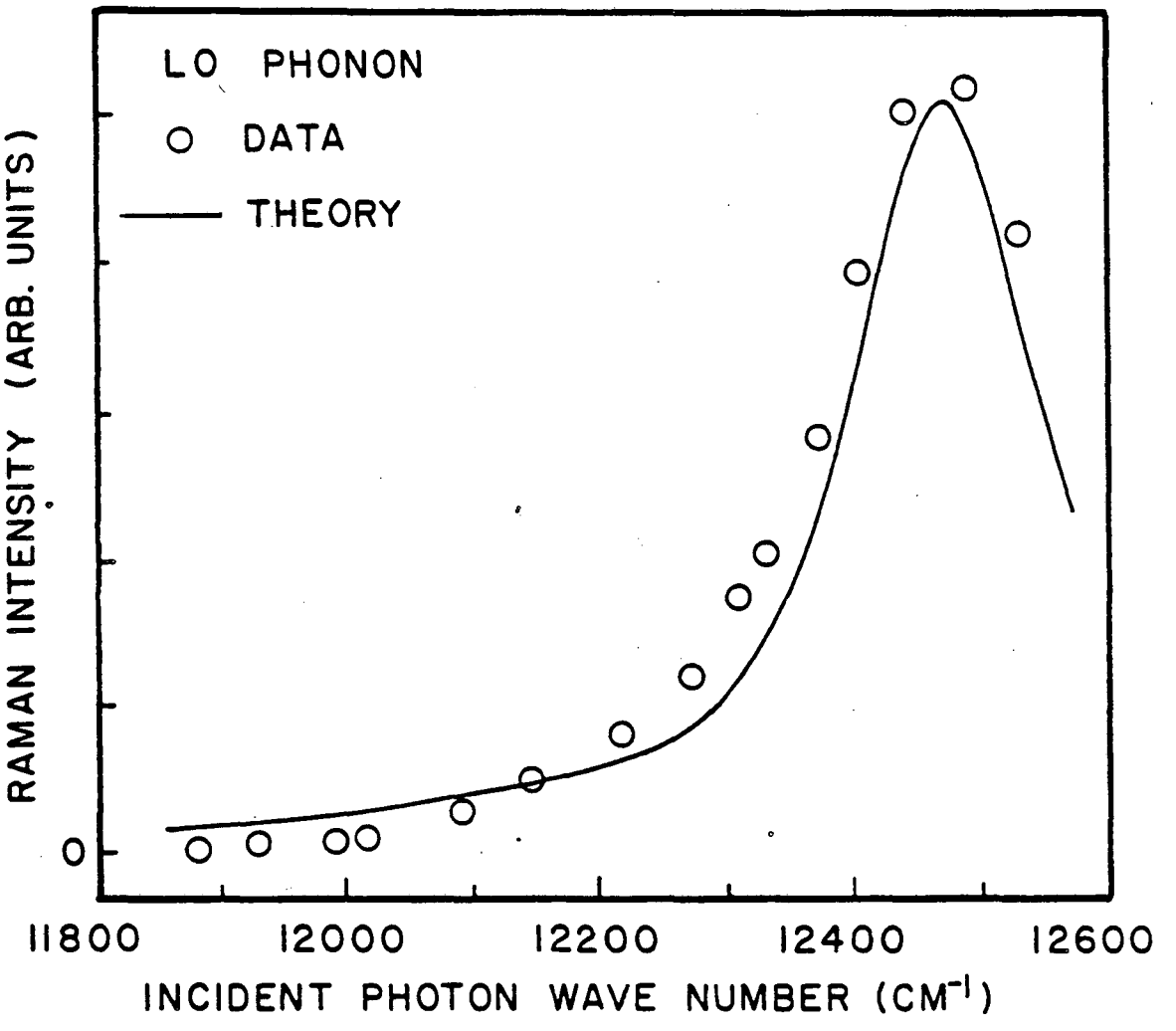
LO PHONON
DATA
THEORY
RAMAN INTENSITY (ARB. UNITS)
0
11800
12000
12200
12400
12600
INCIDENT PHOTON WAVE NUMBER (CM⁻¹)

Figure 3.11

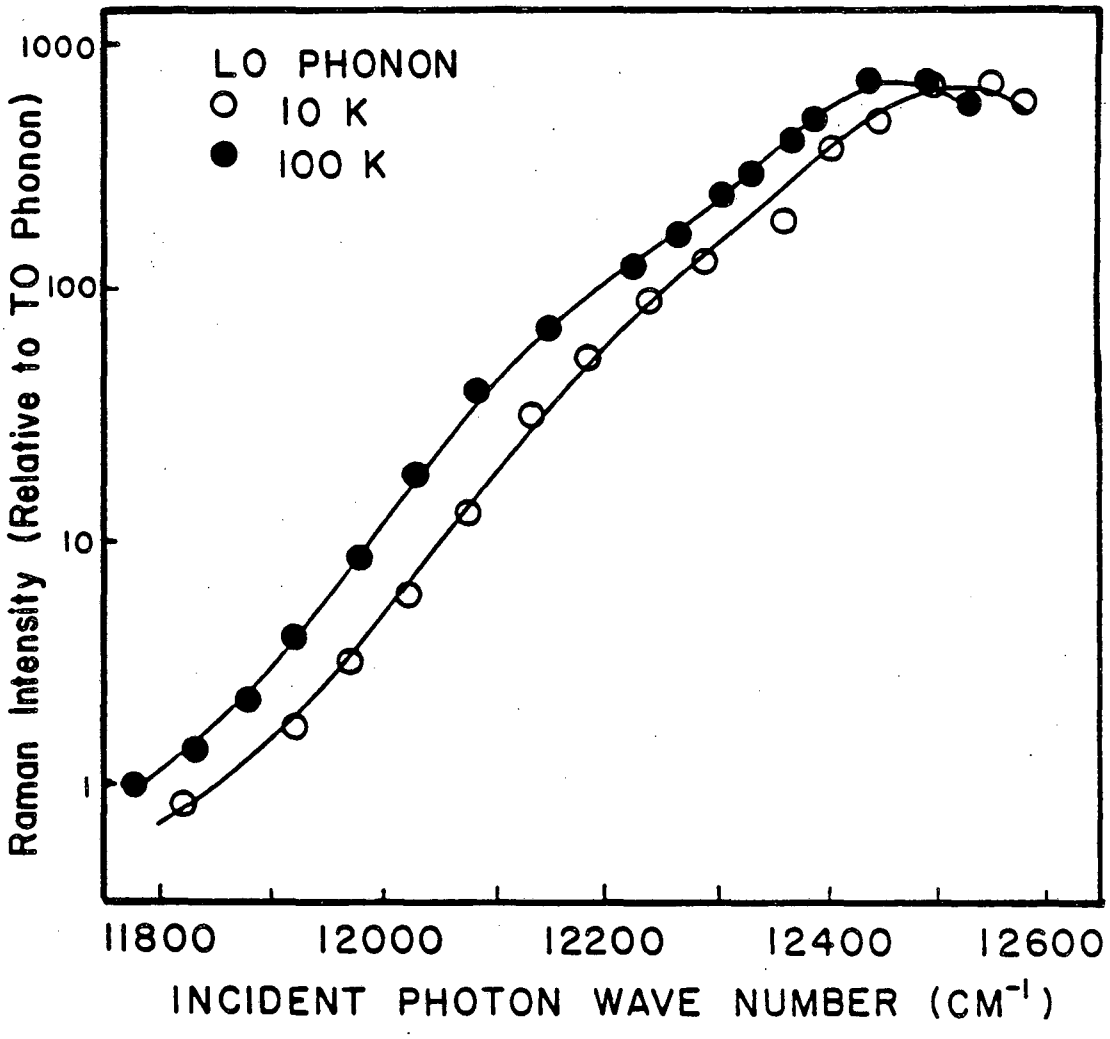
LO PHONON
10 K
100 K
1000
100
10
1
Raman Intensity (Relative to TO Phonon)
11800
12000
12200
12400
12600
INCIDENT PHOTON WAVE NUMBER (CM⁻¹)

Figure 3.12a

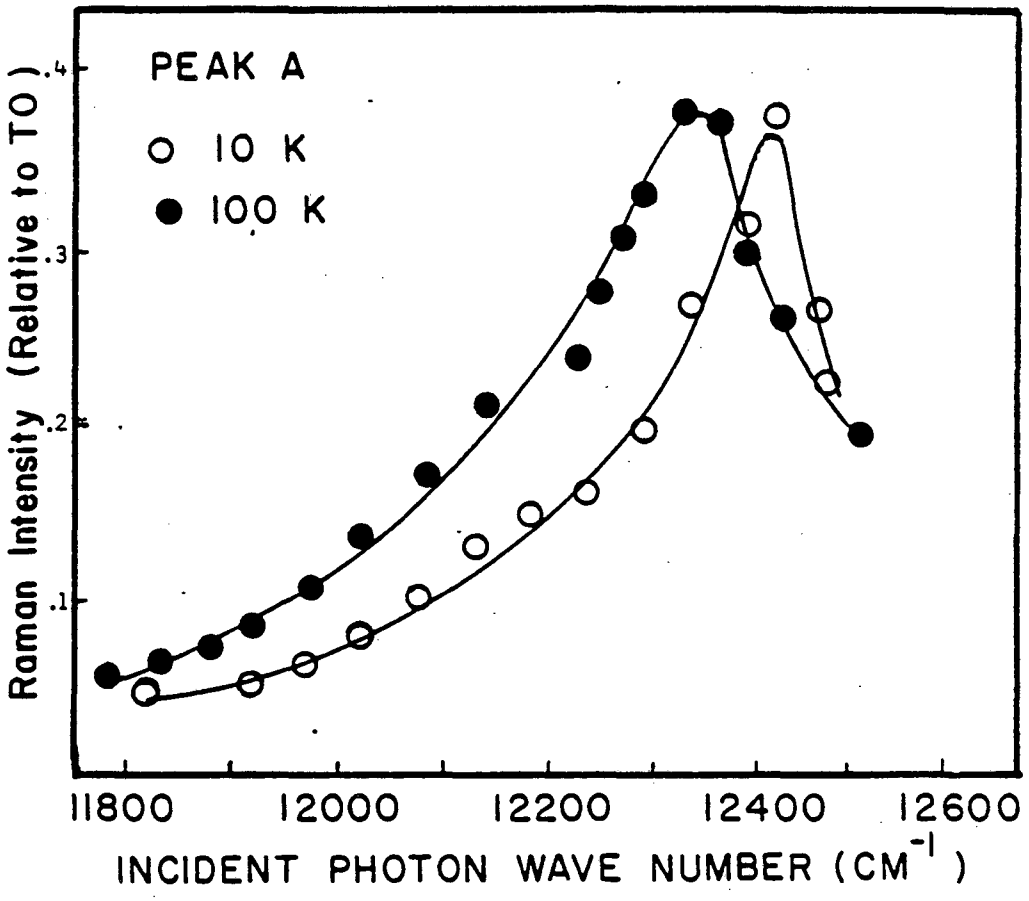
PEAK A
10 K
100 K
Raman Intensity (Relative to TO)
.4
.3
.2
.1
11800
12000
12200
12400
12600
INCIDENT PHOTON WAVE NUMBER (CM-1)

Figure 3.12b

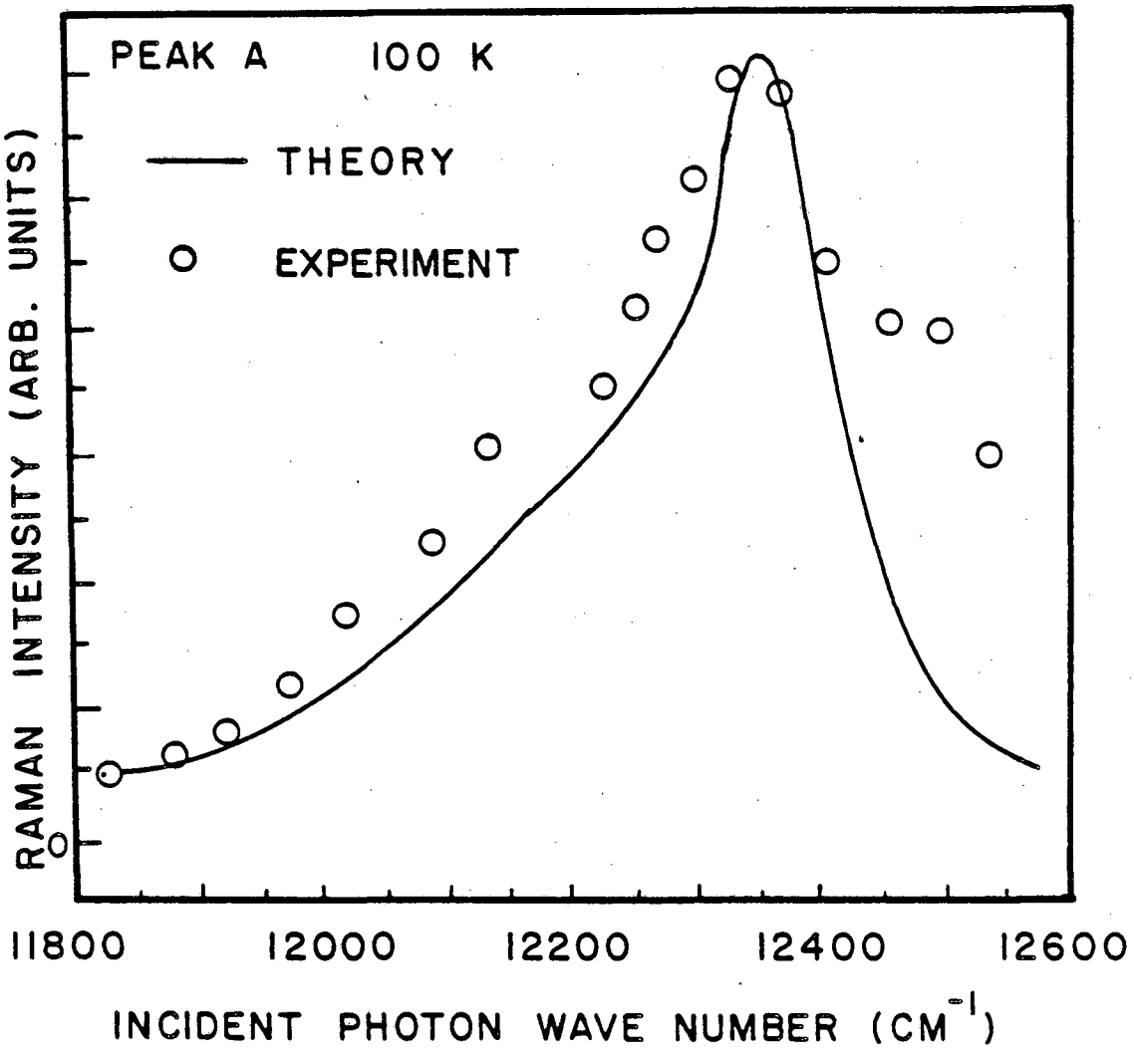
PEAK A 100 K
THEORY
EXPERIMENT
RAMAN INTENSITY (ARB. UNITS)
11800
12000
12200
12400
12600
INCIDENT PHOTON WAVE NUMBER (CM⁻¹)

Figure 3.13a

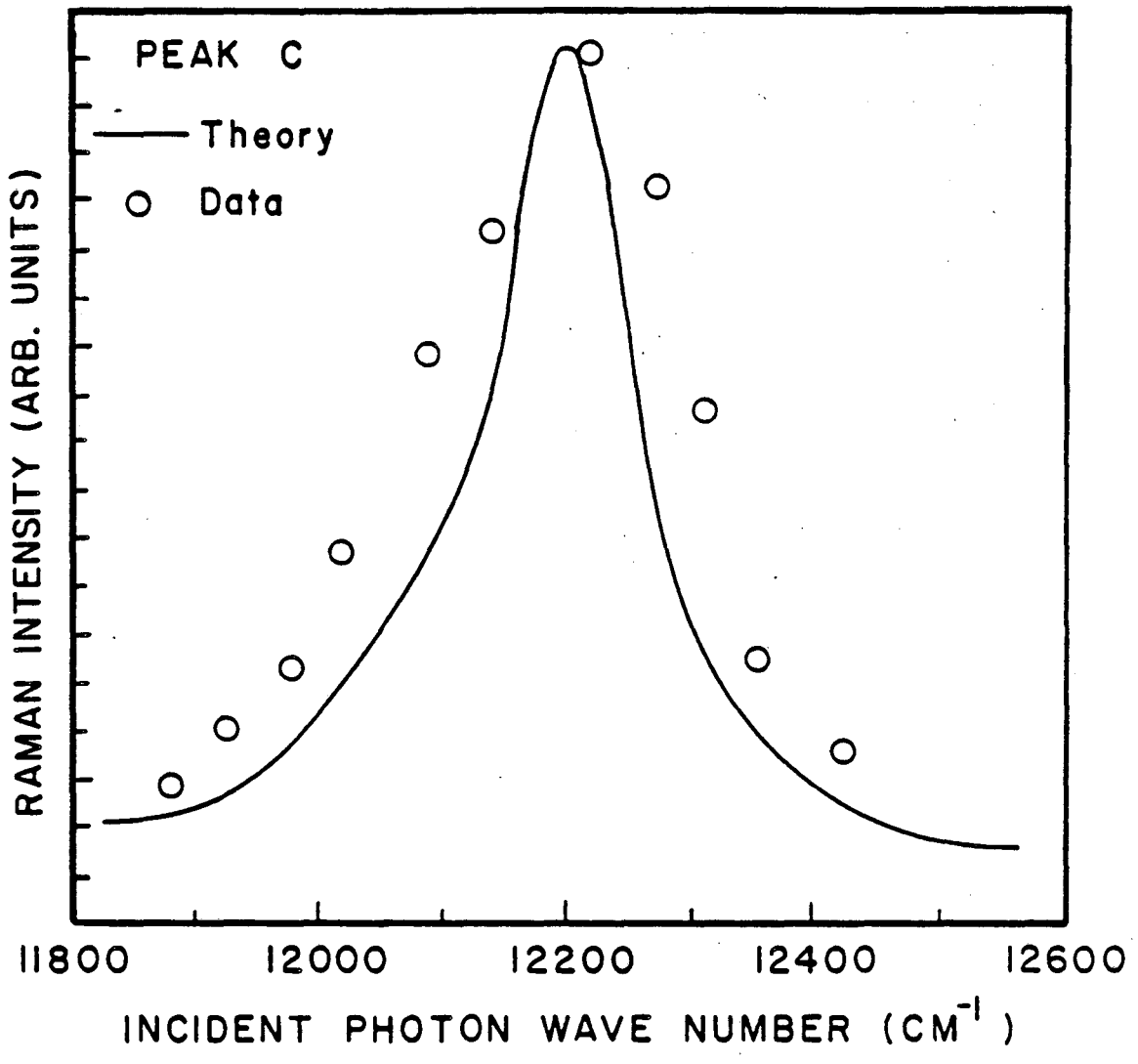
PEAK C
Theory
Data
RAMAN INTENSITY (ARB. UNITS)
11800
12000
12200
12400
12600
INCIDENT PHOTON WAVE NUMBER (CM^{-1})

Figure 3.13b

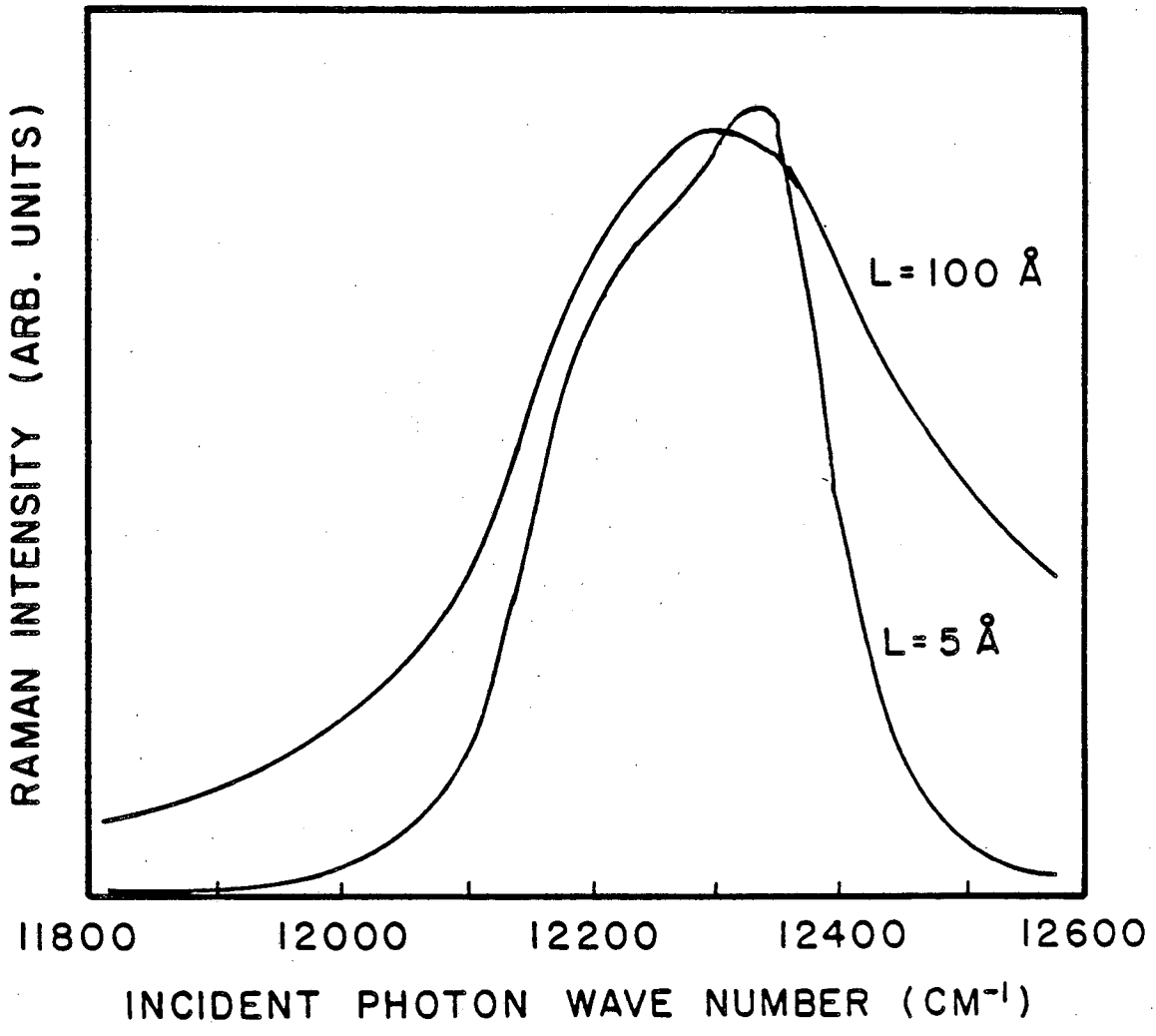
RAMAN INTENSITY (ARB. UNITS)
L = 100 Å
L = 5 Å
11800
12000
12200
12400
12600
INCIDENT PHOTON WAVE NUMBER (CM⁻¹)

Figure 3.14

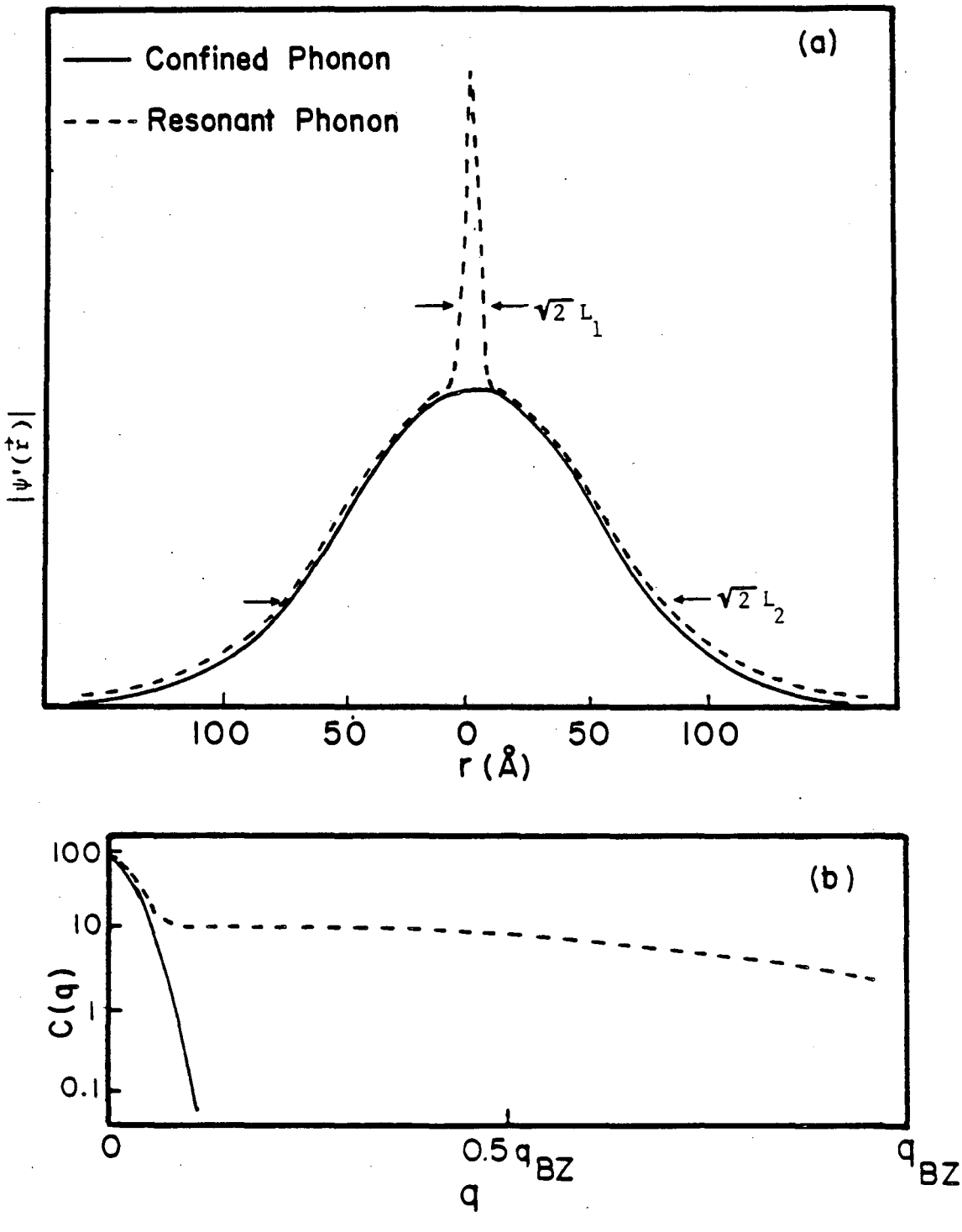

Figure 3.15a,b

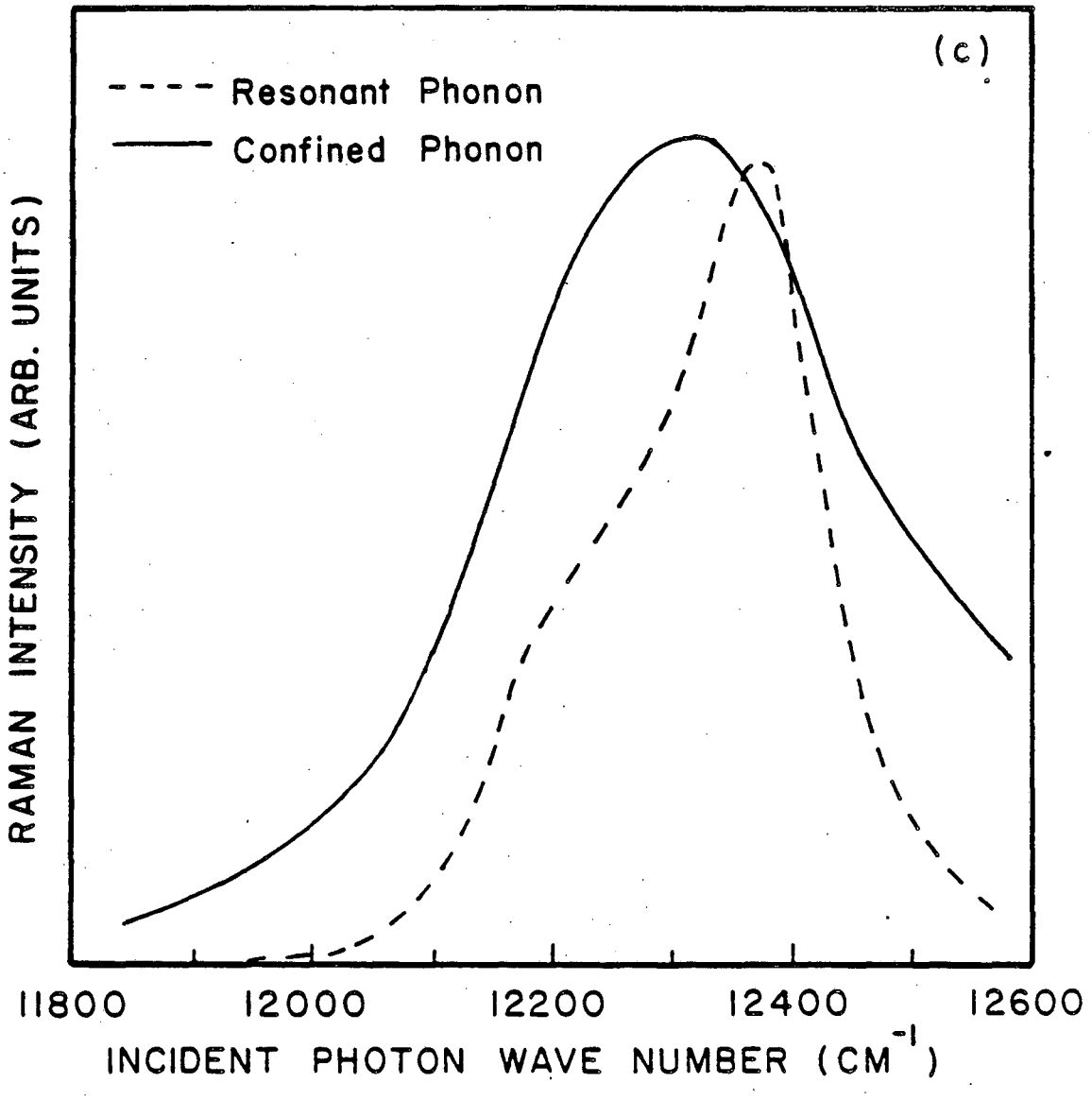
(c)
Resonant Phonon
Confined Phonon
RAMAN INTENSITY (ARB. UNITS)
11800
12000
12200
12400
12600
INCIDENT PHOTON WAVE NUMBER (CM^{-1})

Figure 3.15c

Chapter 4

Future Directions

This work suggests many possible areas for future research. Some of these have already been mentioned in chapters 1 through 3 such as:

- Tuning the excitation energy through localized electronic states that lie in the gap.

- Examining the behavior of the defect related scattering under the application of hydrostatic or uniaxial pressure.

- Examining defect induced modes in alloys such as GaAlAs or GaPAs.

- Examining the dependence of the Raman spectra on whether the incident beam of high energy electrons travels along a (111) or a (-1-1-1) direction.

Other possible avenues for research include:

- Using Raman scattering to study the kinetics of the annealing process.

- The discussion concerning spatially confined and resonant phonons suggests that it may be possible to distinguish between these two cases by monitoring how the Raman spectrum and the RRS lineshape changes as a function of electron dose.

- It will be interesting to examine other semiconductors. GaP appears an interesting place to start. It has the advantage of having a fundamental gap that lies in the visible portion of the spectrum. Also there is a distinct gap in the phonon density of states between the acoustical and the optical branches and true local modes are more likely.

LAWRENCE BERKELEY LABORATORY
TECHNICAL INFORMATION DEPARTMENT
UNIVERSITY OF CALIFORNIA
BERKELEY, CALIFORNIA 94720